Molecular Engineering of Peptide-Inorganic Interfaces: From Aqueous Conformations to Complex Surface Assemblies

Tyler Dean Jorgenson

A dissertation

Submitted in partial fulfillment of the

Requirements for the degree of

Doctor of Philosophy

University of Washington

2020

Reading Committee:

René Overney, Chair

Mehmet Sarikaya, Chair

Walter Pfaendtner

Program Authorized to Offer Degree:

Molecular Engineering and Sciences

University of Washington

Abstract

Molecular Engineering of Peptide-Inorganic Interfaces: From Aqueous Conformations to Complex Surface Assemblies

Tyler Dean Jorgenson

Chairs of the Supervisory Committee:

René M. Overney
Department of Chemical Engineering
Mehmet Sarikaya
Department of Materials Science and Engineering

Bio-inorganic interfaces, in which biomolecules intimately contact inorganic materials, have become the centerpiece for advanced technologies in medicine, catalysis, and electronics. Considering the convolutional complexity of interfaces involving environmental conditions and biomolecular and inorganic surface intricacies, it is of utmost importance to obtain a fundamental understanding of molecular conformations, interactions, and hybrid interfacial properties. Based on such basic understanding, it becomes feasible to engineer molecules with the tailored ability to spontaneously build-up, via self-assembly, a bio-inorganic interface with desired device relevant properties. It has been recognized in this Thesis that solid-binding peptides are suited perfectly for this molecular engineering task due to their vast sequence space, labile conformational nature, and reliance on soft intermolecular interactions that can be fine-tuned through environmental controls, and ability to form long-range ordered structures. Here, solid-binding peptides designed to bind and assemble on graphite surfaces are interrogated using scanning probe microscopy techniques and molecular dynamics simulations to explore and control their self-assembly pathway. Thermal selection of peptide conformations is shown to direct the long-range ordering of peptides at graphite surfaces. Through energetic analysis of

peptide-graphite interactions, using a technique dubbed Intrinsic Friction Analysis, the molecular implications of thermal conformational selection are elucidated and used to rationally design a peptide with tailored binding energy and assembly structure. The impacts of these thermally selected conformations on electron transport across the bio-inorganic interface are interrogated via scanning tunneling spectroscopy and metadynamics, revealing control over device relevant properties. Peptide-substrate recognition is explored using atomic resolution microscopy to understand peptide miscibility and nucleation in binary assemblies. Finally, the role of lateral confinement on self-assembly is explored, revealing unexpected peptide adsorption and assembly phenomena enabling tailored self-assembly at various length scales. From these fundamental insights, novel bio-inorganic devices can be rationally designed for targeted technological applications.

Table of Contents

Chapter 1:
Introduction:
Molecular Engineering of Peptide-Inorganic Interfaces: From Aqueous Conformations to Complex Surface Assemblies

Since the advent of nanoscience, nanomaterials have been at the forefront of biomedical research due to their tunable electronic properties and size.[2] Nanomaterials, such as nanoparticles, have been successfully implemented in biomedical diagnostics, drug delivery, and imaging.[3-5] The potential technological applications of nanomaterials were significantly broadened by the discovery of graphene, an atomically thin sheet of sp^2 hybridized carbon.[6,7] Much of the research exploration of nanomaterials has focused on fabricating, characterizing and developing technologies based on this family of two-dimensional (2D) single layer atomic materials.[8,9] In particular, significant effort has been placed in leveraging the exceptional electronic properties of graphene and other 2D nanomaterials for the development of highly sensitive and selective bioelectronic technologies.[10-12]

In the field of bioelectronics, in which biomolecules are integral components of the device, the molecular scale structure of the bio/nano interface is critical for controlling device functionality. For instance, proper biomolecular orientation is needed to display functional epitopes, while changes in biomolecule-substrate coupling will directly affect electronic transport phenomena across the interface. A multitude of functionalizations have been created to link biomolecules to nanomaterial surfaces and tailor the properties of the nanomaterial, e.g. imparting biofunctionality and anti-fouling properties.[13] The two primary functionalization methods are covalent chemical linkages and non-covalent

physical adsorption. Covalent surface functionalizations, such as self-assembled monolayers or polymeric coatings, may impart electronic defects into the nanomaterial resulting in decreased sensing capabilities. [10,14-19] Physical adsorption, on the other hand, preserves the nanomaterial but does not allow for easy tailoring of the nano- to micron scale structure of the interface.

Biomolecules that bind and self-assemble at inorganic surfaces are a promising means to control the molecular to micron scales structure of bioelectronic interfaces. While a variety of biomolecular systems have been engineered for such applications, this work focuses on solid-binding peptides. Solid binding peptides are small biomolecules that are combinatorially selected to bind tightly to target inorganic or polymeric surface.[20-22] In addition to material type, solid-binding peptides (SBPs) also have selectivity towards substrate crystal facets or molecular structure.[23,24] SBPs have been shown themselves to be extremely useful surface functionalization for bioelectronics since they are inherently biocompatible, easily bio-conjugated, and do not impede the electronic properties of the nanomaterial.[25-30]

In addition to acting as biomolecular linkers, SBPs have been used to tailor the nano- to micron scale structure and chemistry of 2D inorganic surfaces through self-assembly. Recent work revealed that SBPs can form both long-range ordered confluent films and unstructured (amorphous) monolayers on two-dimensional surfaces, such as graphite, MoS_2, and Au(111), depending on the peptide sequence and the assembly conditions.[25,31,32] Long-range ordering of the peptide assembly mirrors the crystallographic symmetry of the underlying lattice suggesting a supramolecular recognition between the peptide and inorganic crystals. In the language of material

science, the interface between the peptide and inorganic materials is coherent. Analogous to traditional inorganic devices, development of these coherent interfaces promises to seamlessly merge biological and man-made systems and aid the development of hierarchically assembled functional bioelectronics. Thus, the rational design and fabrication of self-assembling bio-inorganic interfaces with desired structure and properties is paramount.

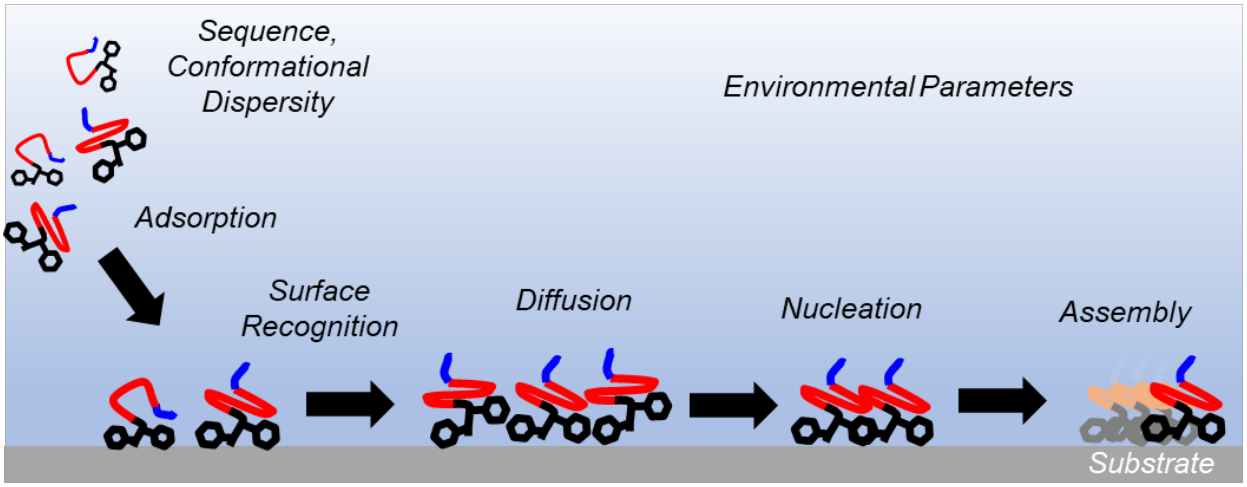

Figure 1.1. Schematic of peptide adsorption and self-assembly at atomically flat inorganic interfaces.

As schematized in Figure 1.1, the self-assembly of soft peptide-inorganic interfaces results from several interconnected steps, namely, the adsorption, surface recognition, diffusion, nucleation, and, finally, growth of the long-range ordered phase. All these assembly steps are intimately dependent on the peptide-peptide and peptide-substrate intermolecular interactions, and hence, on the peptide sequence, conformation, and environmental parameters of the system. For the rational design of SBPs and device relevant peptide-inorganic interfaces, engineers need to be guided by molecular fundamentals describing the complex relationships dictating peptide surface assembly as

outlined above and presented in Figure 1.2. Along these lines, this work focuses on developing such molecular insights and illustrates their utility in engineering the self-assembly of peptide-graphite interfaces via environmental parameters and sequence modifications. First, the experimental and theoretical methodologies that were used and have been developed are described in Chapter 2. The impacts of temperature, specifically thermal conformational selection, on self-assembly structure are discussed in Chapter 3. The energetic implications of this thermal conformational selection are discussed and leveraged to rationally design a self-assembling SBP in Chapter 4. The impacts of peptide conformation and substrate coupling on the electron transport across the hybrid interface are discussed and compared in Chapter 5. The role of divergent peptide-substrate molecular recognition in the nucleation of binary assembled peptide systems is the focus of Chapter 6. Finally, the effects of lateral confinement on peptide diffusion and self-assembly are explored in Chapter 7.

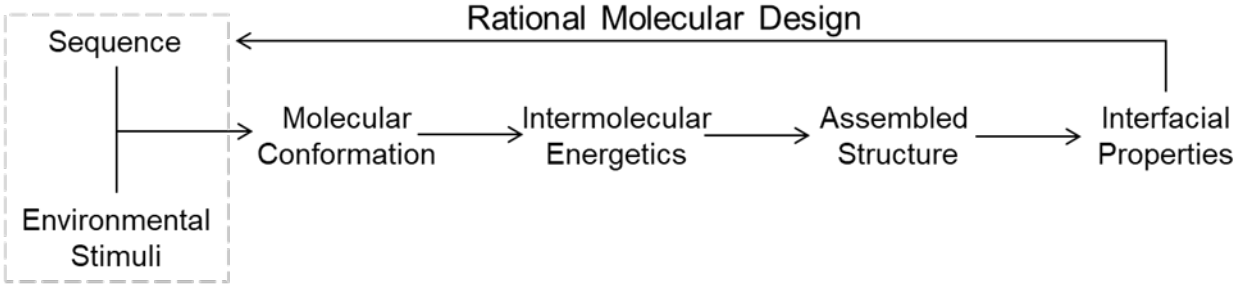

Figure 1.2. Overview of the presented research project in which fundamental molecular understanding about the sequence, conformation, and interfacial properties will be determined and implemented to tailor the hybrid peptide-inorganic interface.

Chapter 2:
Theoretical and Experimental Methodologies

Each step of the complex process leading to the self-assembly of peptides on inorganic surfaces, as schematized in Figure 1.1, is greatly impacted by the peptide sequence, conformation, and environmental assembly parameters. In this chapter, the theoretical considerations critical for understanding the experimental system are discussed followed by a detailed description of the experimental techniques used herein to analyze the system.

2.1 Theoretical Underpinnings of Peptide Surface Binding and Assembly

2.1.1 Peptide Conformational Dynamics

Peptides are naturally occurring short biopolymer analogues to proteins with biological activity and importance, such as signaling and biomineralization. Given the ease of synthesizing and engineering peptides, they have become key components of functional biomaterials. Peptides selected through directed evolution techniques for binding to inorganic surfaces, called solid-binding peptides (SBPs), typically range from 7-14 amino acids in length. These short peptides are typically considered intrinsically disordered as the limited intramolecular interactions present are not sufficient to stabilize a consistent conformation. As schematized in Figure 2.1, proteins are characterized by a deep free energy well in their conformational landscape related to the folded protein structure. In contrast, the conformational landscape of short solid binding peptides is more aptly described as a corrugated surface with small energetic barriers separating local free-energy minima. That is to say, short peptides in aqueous solution have a multitude of metastable conformational states that are easily transitioned between. The dispersity

of conformations in solution is therefore determined by a Boltzmann distribution of the metastable states.

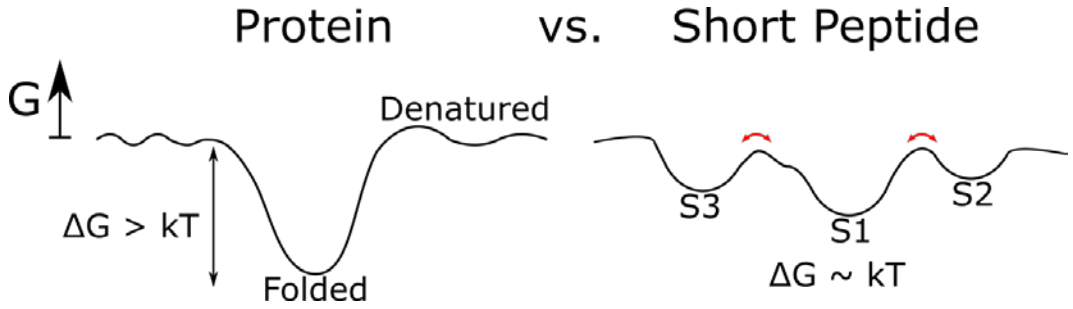

Figure 2.1 Comparison of conformational free energy, G, landscapes of globular proteins and short peptides. Differing conformational metastable states of the peptide are denoted by S1, S2, and S3.

The dispersity and stability of the peptide's solution conformations have been shown to depend on environmental parameters such as pH and temperature.[33,34] Moreover, as a result of SBP's environmental dependent conformational dispersity, SBP binding and interactions with inorganic surfaces are similarly dependent on the aqueous environmental conditions. For example, work on titanium binding peptides showed how the ionic conditions of the aqueous solution mediated the binding conformation and energetics.[35] Given the relationship between peptide conformational dispersity and environmental parameters, the environmentally variable interfacial region between the bulk solution and solid surface is of critical importance to peptide adsorption.

2.1.2 Complexity of the Bio-Inorganic Interface

Generally, experimental investigations into biomolecular interactions with solid surfaces view adsorption as a binary state change from the bulk solution state to the equilibrium surface state (see Section 2.1.3). While this approach allows for determination of overarching kinetics and energetics of protein adsorption, the transitory regime between the bulk solution and surface with bulk-deviating properties, a critical parameter

space dubbed going forward as the “boundary regime”, is neglected. It is the properties and interfacial phenomena within the boundary regime that play a pivotal role in determining the adsorption process and interactions at the surface for conformationally pliable biomolecules like SBPs. Not only does the boundary regime possess a locally varying chemical potential, μ, it also exhibits dimensional constraints due to its small size on the 1-10 nm scale.[36-38] Dimensional constraints substantially alter mixing properties, leading to altered adsorption resonances (times), as well as preferential (species specific) diffusion.[38]

Characteristics of the boundary regime result from the confluence of bulk environmental properties and the inherent surface properties of the substrate. The boundary regime greatly depends on the aqueous context with which the inorganic surface interacts. Figure 2.2A schematizes the boundary regime between a bulk solution and inorganic surface accompanied by the key properties dictating and describing this complex interface. The bulk solution can be described by the temperature, ionicity, pH, and biomolecular concentration. A given biomolecular species may be further described by specific chemistry (*i.e.*, sequence, charge, hydrophilicity, *etc.*) and conformational dispersity, Đ, as discussed in Section 2.1.1.

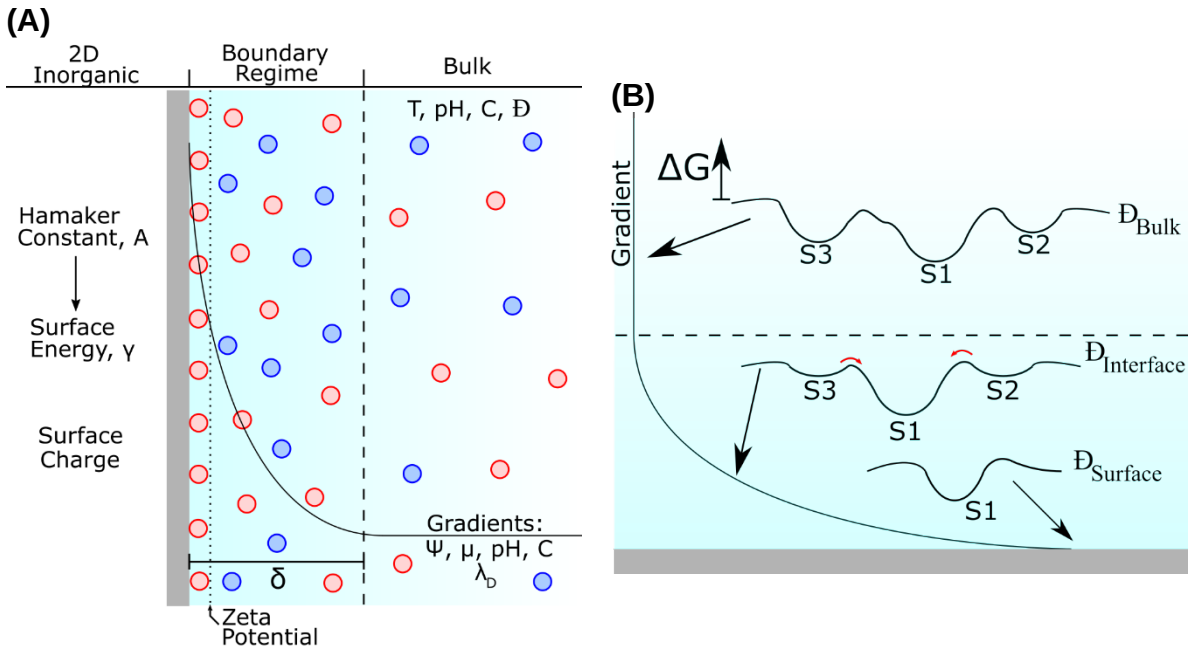

Figure 2.2 (A) Complexities of the boundary regime between bulk solution and an inorganic surface. Red and blue circles are negative and positive charges, respectively. (B) Schematic describing how environmental gradients in the boundary regime and intermolecular biases induced by the substrate can modify the free energy landscape of the peptide confromation during the adsorption process.

Resulting from the combination of the bulk solution and the substrate will be a boundary regime with a defined thickness, δ. Parameters considered to be isotropic within the bulk solution phase will be dependent on the distance from the surface within the boundary regime. Specifically, there will be a gradient in the pH and ion concentration within the boundary regime. This gradient will result in a varying electrostatic potential, Ψ, with a specific decay length known as the Debye length, λ_D, that depends on the ionicity and temperature, as shown in Equations 2.1 and 2.2.

$$\Psi = \Psi_0 \exp(-\lambda_D x) \quad Equation\ 2.1$$

$$\lambda_D = \left(\frac{2e^2 z^2}{\varepsilon \varepsilon_0 kT}\right)^{1/2} \quad Equation\ 2.2$$

Where Ψ_0 is the potential of the surface, x is the distance from the surface, e is the elementary charge, z is the charge number of the ion, $\varepsilon\varepsilon_0$ is the dielectric of the solvent, and kT is thermal energy. Moreover, due to adsorbed ions at the surface, a charge, known as the zeta-potential, will develop. While not equivalent to a surface charge, the zeta-potential is critical when understanding electrostatic interactions with the substrate. Changes to either the bulk solution or the inorganic surface will have an outsized effect on these boundary parameters thereby effecting how peptides in solution interact and adsorb to the surface. Due to these bulk-deviating properties, intermediate peptide conformational states may be stabilized within the boundary regime, mediating the transition from bulk solution to surface adsorbed, as schematized in Figure 2.2B. These transitory interfacial states are critical for understanding why and how SBPs interact with inorganic surfaces.

2.1.3 Molecular Adsorption Kinetics and Energetics

Molecular adsorption to surfaces is critical for many technologies from sensing to catalysis. For the fabrication of robust bioelectronics interfaces utilizing self-assembling solid binding peptides, it is critical to determine the peptide's binding kinetics and energetics to their target inorganic surface at a variety of environmental conditions. Several theoretical and empirical models have been developed to interrogate the molecular adsorption. The simplest among these models is the Langmuir Isotherm first derived by Irving Langmuir to describe the adsorption of gas molecules to a solid surface.[39] The Langmuir Isotherm assumes:

1. The molecule-surface interaction energetics are consistent for all molecules and surface sites. Specifically, the surface is homogenous with all surface sites having

the same adsorption activity, and the molecular adsorption mechanism is the same for all molecules

2. Only molecule-surface interactions exist such that the adsorbed molecules do not interact in-plane or form multilayers.

As shown in Figure 2.3, the Langmuir model considers the adsorption of a molecule *M* to a surface adsorption site S to generate a surface adsorbed species, *MS*, as described by the reaction:

$$M + S \rightleftarrows MS \quad Equation\ 2.3$$

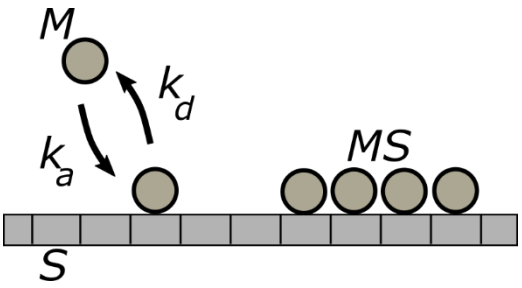

Figure 2.3. Langmuir adsorption schema of a molecule, *M*, binding to surface sites, *S*, to generate a surface adsorbed species, *MS*. Adsorbed molecules only interact with the substrate and not with each other.

As *MS* is generated the fractional occupancy of surface sites (surface coverage), *Γ*, will increase. Therefore, the rates of adsorption, r_a, and desorption, r_d, can be represented in terms of *Γ* and the molecule concentration, *[M]*.

$$r_a = k_a[M](1 - \Gamma) \quad Equation\ 2.4$$

$$r_d = k_d(\Gamma) \quad Equation\ 2.5$$

k_a and k_d are the rate constants for adsorption and desorption, respectively. At equilibrium. the rates of adsorption and desorption will be equivalent, thus, providing the functional form of the Langmuir Isotherm.

$$K = \frac{k_a}{k_d} = \frac{\Gamma^*}{[M](1-\Gamma^*)} \quad \text{Equation 2.6}$$

Or equivalently,

$$\Gamma^* = \frac{K[M]}{1+K[M]} \quad Equation\ 2.7$$

where *K* is the equilibrium adsorption rate constant and Γ^* is the equilibrium surface coverage, respectively. Experimentally, *K* is determined by measuring Γ^* as a function of [M] and fitting to Equation 2.5. The standard free energy of adsorption, ΔG_{ads}, can be determined from K by the following relationship.

$$\Delta G_{ads} = -RT \times \ln(K) \quad Equation\ 2.8$$

Due to the simplistic nature of the Langmuir model, it has been consistently used to measure the kinetics and energetics of more complex systems. However, it must be noted that the assumptions of the model do not typically hold for biomolecular systems, such as solid-binding peptides. For example, solid-binding peptides form complex assembly structures that rely on a multitude of intermolecular interactions. Moreover, the heterogeneous nature of experimental inorganic surfaces, e.g., step-edges or defect sites, allows for site specific adsorption enthalpies. Empirical models and extensions to the Langmuir model have been made to address such discrepancies. Table 2.1 compares different adsorption models.[40-42]

Table 2.1 Molecular Adsorption Models Beyond Langmuir

Adsorption Model	Equation	Notes
Freundlich	$\Gamma = K[M]^{1/n}$	Describes adsorption to a heterogeneous surface. K and n are fit parameters.
Frumkin	$\ln\left(\frac{\Gamma}{(1-\Gamma)[M]}\right) = \ln(K) + g\Gamma$	Assumes that the heat of adsorption decreases linearly with coverage. Considers molecule-molecule interactions. *g* is an additional fit parameter.
Toth	$\Gamma^C = \frac{\alpha[M]^C}{1/K + [M]^C}$	Empirical modification of Langmuir model for adsorption to a heterogeneous surface. *C*, *α*, and *K* are fit parameters.

Beyond the intermolecular interactions and the possible chemical heterogeneity of the system, the labile nature of the peptide's conformation with environmental parameters may result in differing peptide-substrate interactions, and therefore, K and ΔG_{ads} values that reveal non-Arrhenius temperature dependences. This level of molecular complexity is not adequately addressed by theoretical model equations, thus, experimental techniques for the direct determination of binding energetics is critical. As will be seen in Chapter 4, the effect of temperature on the peptide binding energetics and kinetics is elucidated via a novel scanning probe microscopy-based technique (technique outlined in Section 2.2.3).

2.1.4 Principles of Molecular Self-Assembly

To control the self-assembly process of peptides at solid surfaces, it is critical to unravel how the energetics of peptide-peptide interactions and self-assembly are related to peptide sequence, conformation, and environmental parameters. As a simple basis for understanding the self-assembly energetics of peptides one can look to the kinetics of molecular aggregation[43] as schematized in Figure 2.4.

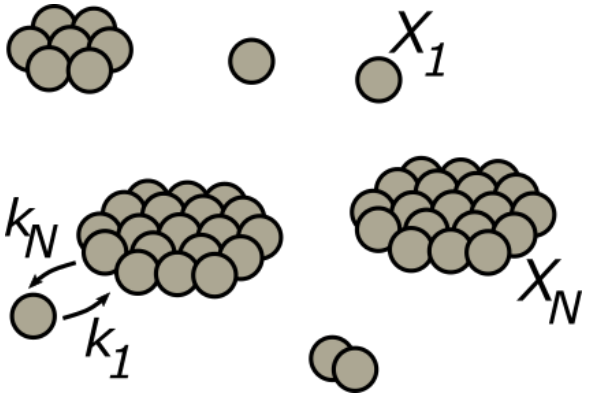

Figure 2.4. Schematic of two-dimensional aggregation of spherical monomers into circular aggregates.

The rate of association of *N* monomers, R_a, and the rate of dissociation for an aggregate of size *N*, R_d, can be described by Equations 2.9 and 2.10, respectively,

$$R_a = k_1 X_1^N \quad Equation\ 2.9$$

$$R_d = k_N (X_N / N) \quad Equation\ 2.10$$

where k_1 and k_N are the rate constants for association and dissociation, respectively, and X_1 and X_N are the chemical activity of the monomer and the aggregate, respectively. Moreover, the equilibrium constant for monomer aggregation, *K*, can be related to the standard chemical potential difference between the aggregate, μ_N^o, and monomer, μ_1^o, by Boltzmann statistics as presented in Equation 2.11.

$$K = \exp\left(\frac{-N(\mu_N^o - \mu_1^o)}{kT}\right) \quad Equation\ 2.11$$

Collectively Equations 2.9, 2.10 and 2.11 imply that the molecular system is in thermodynamic equilibrium, Equation 2.12.

$$\mu = \mu_1^o + kT\ ln(X_1) = \cdots = \mu_N^o + \frac{kT}{N}\ ln\left(\frac{X_N}{N}\right) = const.\ Equation\ 2.12$$

Equation 2.12 describes the first of two thermodynamic conditions that must be met for stable aggregates to form, which are:

1. The combined chemical potential of all identical molecules in an aggregate must be equivalent for different sized aggregates (Equation 2.12), and
2. There must be a favorable difference in the cohesive interaction energies within aggregates relative to the aqueous monomer, i.e., the standard chemical potential of the aggregate must be smaller than that of the monomer, $\mu_1^o > \mu_N^o$.

The monomer aggregation process can be fully thermodynamically described by the conservation of species, Equation 2.13, and by the chemical activity of the aggregate, X_N, represented in terms of the monomer, Equation 2.7 (as derived from Equation 2.12).

$$C = \sum_{N=1}^{\infty} X_N \quad Equation\ 2.13$$

$$X_N = N(X_1 \exp[(\mu_1^o - \mu_N^o)/kT])^N \quad Equation\ 2.14$$

In Equation 2.13 and 2.14, *C* is the total concentration of molecules, *k* is the Boltzmann constant, and *T* is the absolute temperature in Kelvin.

The standard chemical potential of an aggregate, μ_N^o, is the sum of the molecule-molecule interaction energies within the aggregate relative to an aqueous monomer. As the molecules at the aggregate's edge lack some possible molecular interactions, these interaction energies must be subtracted from the expected total interaction energies for an aggregate of size *N*. Thus, the chemical potential of the aggregate will depend on its

dimensionality, shape, as well as on the monomer's shape. Equation 2.15 is a generalized representation of μ_N^o in which α describes the strength of the intermolecular interactions, and p is a number that depends on the shape and dimensionality of the system.

$$\mu_N^o = \mu_\infty^o + \frac{\alpha kT}{N^p} \quad Equation\ 2.15$$

Combining Equation 2.14 and 2.15, provides an important relationship between α and X_N.

$$X_N \approx N[X_1 e^{\alpha}]^N \quad Equation\ 2.16$$

This relationship implies that when the activity of the monomer, X_1, reaches $e^{-\alpha}$ the monomer concentration can no longer increase, denoting a critical aggregation concentration, *CAC*, at which aggregates of size *N* must start forming.

$$(X_1)_{crit} = CAC \approx e^{-\alpha} \quad Equation\ 2.17$$

The relationship presented in Equation 2.10 holds for all *p* and, more critically, provides a way to translate an experimental observable *CAC* to the fundamental interaction energetics between the monomers. Analogous equations to Equation 2.17 can be constructed to relate concentrations of larger aggregates of size *M*, where $M < N$. While the above discussion provides a way to analyze the energetics of aggregating molecules, it does not distinguish between "amorphous" aggregates and "crystalline" aggregates that are observed during the peptide self-assembly process. In fact, the bond counting method used to derive the prior equations assumes the aggregate has a type of crystallinity or periodicity within the bulk.

In terms of the energetics of the system, the experimentally observed amorphous to crystalline transition requires that the standard chemical potential of the crystalline

phase is lower than that of an amorphous aggregate of the same size, $\mu^{o}_{N,crystal} < \mu^{o}_{N,amorphous}$. Amorphous aggregation can thus be viewed as an aggregate with irregular (or non-specific) intermolecular interactions between the monomers within the bulk amorphous aggregate. This irregularity is rationalized by the chemical heterogeneity of biomolecules and the multitude of possible configurations by which the biomolecules interact. To extract the free energy of self-assembly from the observed transition, a concentration analogous to the *CAC* with a similar relationship to the interaction strength of the monomers is used, namely, the critical self-assembly concentration, or as denoted in this work, C_{50}. C_{50} is the monomer concentration at which 50 % of the monomers are contained within the self-assembled crystalline phase.

$$C_{50} \approx e^{-\Delta G_{assembly}/kT} \quad Equation\ 2.18$$

As will be seen in Chapter 3, the energetics of self-assembly as discussed in this section are applied to extract the free energy of assembly for two graphite binding peptides of differing sequence.

2.1.5 Thermodynamics of Crystal Nucleation

As detailed in Section 2.1.4, equilibrium thermodynamics of molecular aggregation can be used a basis for understanding peptide self-assembly. However, the presence of the metastable intermediate amorphous phase during the self-assembly process indicates there exists an energetic barrier to the formation of the crystalline aggregate. In this section the fundamentals of crystal nucleation are described to address this shortcoming.

From a thermodynamic perspective, the nucleation rate of a crystal, dn/dt, is proportional to the Boltzmann probability that monomers overcome an energetic nucleation barrier, Δg_{nuclei}, and form a cluster of critical radii, as shown in Equation 2.19: [44,45]

$$\frac{dn}{dt} = A \exp\left(\frac{\Delta g_{nuclei}}{kT}\right) \quad Equation\ 2.19$$

where A is a pre-exponential factor related to the diffusion and sticking probability of the monomer, k is the Boltzmann constant, and T is the absolute temperature in Kelvin. The nucleation barrier, Δg_{nuclei}, is dependent on the dimensionality of the nucleating crystal, the shape of the crystal, and whether the nucleation process is homogenous or heterogeneous. The total free energy of the cyrstal, $\Delta g_{crystal}$, arises from the balancing of the free energy of the bulk molecules in the crystal, Δg_{bulk}, and the free energy of the crystal interface, Δg_{edge}, as schematized in Figure 2.5 for a two-dimensional nucleation process.

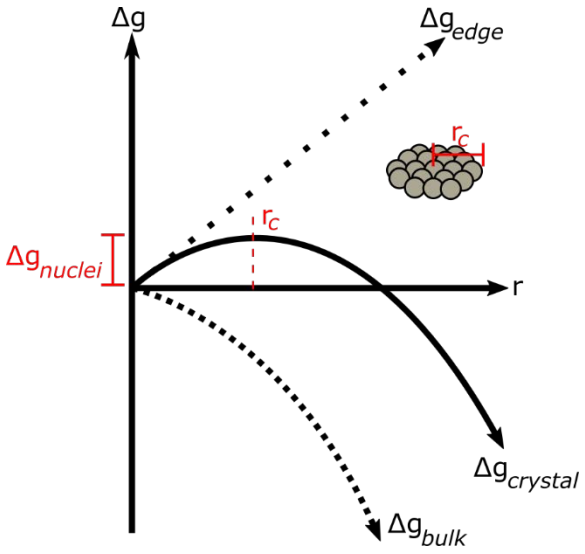

Figure 2.5. Depiction of the free energy of a growing two-dimensional circular crystal nucleus as a function of radius. The system has a critical radius, r_c, and barrier to nucleation of Δg_{nuclei}. The inset depicts a crystal nucleus of critical radius.

Given that solid binding peptide self-assembly is confined to two-dimensions and at a solid interface, we can approximate the nucleation rate using a classical 2D nucleation model. For 2D nucleation of circular monomers, the free energy of the bulk crystal, Δg_{bulk}, and the free energy of the crystal interface, Δg_{edge}, are as follows:

$$\Delta g_{crystal} = \Delta g_{edge} + \Delta g_{bulk} = 2\pi r\lambda - \frac{\pi r^2}{A_m}\Delta\mu \qquad Equation\ 2.20$$

Where r is the radius of the nuclei, λ is the line-tension of the crystal-substrate interface, A_m is the area per monomer, and $\Delta\mu$ is the chemical potential difference between the monomer and the crystal phase. The critical radius occurs, r_c, when the gradient of $\Delta g_{crystal}$ is 0.

$$0 = \frac{dg_{crystal}}{dr} = 2\pi\lambda - \frac{2\pi r_c}{A_m}\Delta\mu$$

$$r_c = \frac{\lambda A_m}{\Delta\mu} \qquad Equation\ 2.21$$

The free energy barrier associated with forming a nucleus of critical radius, Δg_{nuclei}, is thus

$$\Delta g_{nuclei} = 2\pi\frac{\lambda A_m}{\Delta\mu}\lambda - \frac{\pi\left(\frac{\lambda A_m}{\Delta\mu}\right)^2}{A_m}\Delta\mu = \frac{\pi A_m\lambda^2}{\Delta\mu} \qquad Equation\ 2.22$$

The chemical potential, $\Delta\mu$, is most generically defined as $\Delta\mu = kTln(\alpha)$, where k is the Boltzmann constant, T is the temperature in Kelvin, and α is the activity of the system (note this is a different parameter than is discussed in Section 2.1.4). For practical purposes it is beneficial to represent α in terms of an experimental observable in relation to a reference condition scaled by an activity coefficient, γ, that captures non-ideality. Herein, we use the peptide concentration, C, in reference to an equilibrium concentration,

C_e, that denotes the concentration at which a critical nucleus will neither grow nor dissolve. Moreover, we assume $\gamma = 1$ for single phase nucleation, i.e.,

$$\Delta\mu = kTln\left(\gamma\frac{C}{C_e}\right) \cong kTln\left(\frac{C}{C_e}\right) \underset{\frac{c}{c_e}\ll 1}{\longrightarrow} kT\left(\frac{C}{C_e} - 1\right) \quad Equation\ 2.23$$

for low concentrations. Combining Equations 2.19, 2.22 and 2.23, the nucleation rate is given by Equation 2.24.

$$\frac{dn}{dt} = A\exp\left(\frac{\pi A_m\lambda^2}{(kT)^2\left(\frac{c}{c_e} - 1\right)}\right) = A\exp\left(\frac{B}{\frac{c}{c_e} - 1}\right) \quad Equation\ 2.24$$

The fit parameters *A*, *B*, and *Ce* from this model can be used to compare the nucleation properties of peptide self-assembly at solid surfaces as a function of peptide sequence and experimental conditions. As will be seen in Chapter 6, this model fits well with the self-assembly of the graphite binding peptides used in this work. However, this model ignores the conformational complexity of peptide monomers as well as asymmetric growth direction of the studied peptide surface assemblies. For these reasons, other nucleation model may fit experimental data well, for instance, a 1D nucleation model has been successful in interrogating peptide nucleation at surfaces.

2.2 Experimental Methodology

2.2.1 Self-Assembly Sample Preparation

Substrate quality and preparation are critical for reproducible self-assembly of peptides. For the studies presented in this work graphite substrates are used. Graphite is composed of layers of stacked atomically flat two-dimensional sheets of sp^2 bonded

carbon in an A-B-A configuration. Figure 2.6 schematizes the structure of graphite as well as the typical sample preparation processes used in this work.

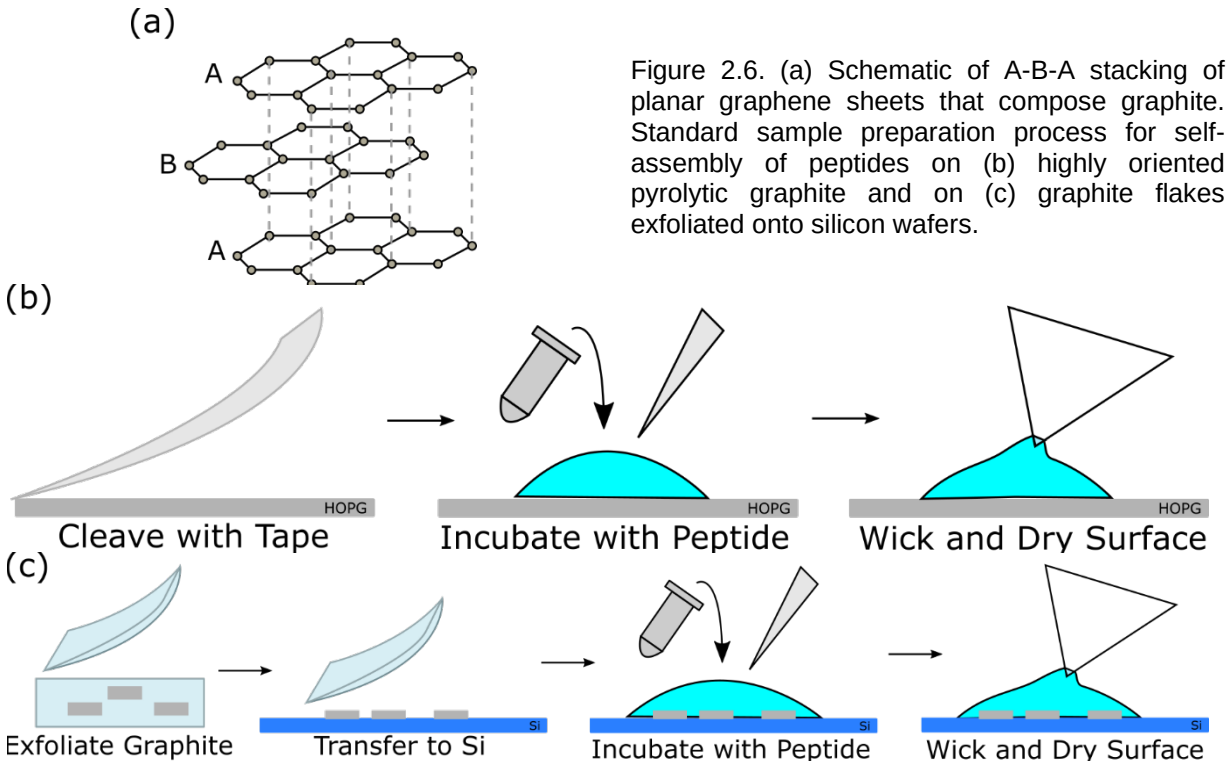

Figure 2.6. (a) Schematic of A-B-A stacking of planar graphene sheets that compose graphite. Standard sample preparation process for self-assembly of peptides on (b) highly oriented pyrolytic graphite and on (c) graphite flakes exfoliated onto silicon wafers.

A renewed interest in graphite has emerged since the discovery of graphene, a single layer of graphite, has repeatedly shown unique electronic properties.[7,46] While self-assemblies on graphene surfaces are the target for many applications, controlling the size, cleanliness and purity of graphene remains a challenge. In this work, high grade highly oriented pyrolytic graphite (HOPG Grade 1, SPI, Inc.) is used to ensure reproducible sample surfaces with minimal to no stack faults and a low density of step-edges. While HOPG is a very well-defined substrate for peptide self-assembly experiments, it is not the only type of graphite used in peptide self-assembly experiments presented herein. Graphite flake is the preferred material when preparing graphene samples through exfoliation. While exfoliation of graphite flakes provides a facile way of

producing graphene for testbed devices, this graphite can have a higher density of stack faults or other defects. Additionally, the resulting substrate sizes range from 10 to 100s of microns in lateral dimension, i.e., several orders of magnitude smaller than the “gold standard” of cleaved HOPG surface. As will be shown in Chapter 7, this variability in lateral size can have measurable impact on peptide surface coverage and self-assembly.

While the bulk concentration of peptide solutions is typically addressed as the variable parameter in many self-assembly experiments, the true variable is the relative ratio of peptide monomers to available graphite sites. Therefore, to ensure consistency between samples the graphite area and the volume of peptide solution must be held constant while other parameters (such as bulk concentration) are varied. For most self-assembly experiments presented in this work graphite surfaces with approximate area of 0.25 cm^2 were prepared by mechanically cleavage using scotch tape. After cleavage, 40 µL of peptide in DI water of varying concentrations were incubated on the graphite surfaces for 3 hours. For many of the kinetic and energetic analyses presented in Section 2.1, the system is assumed to be at equilibrium. The incubation time of 3 hours is used to reach this required equilibrium, as previous studies showed that the structure of the peptide assembly does not significantly change after this time point. To prevent peptide solution evaporation during incubation, the samples is kept in a sealed chamber with saturation vapor pressure. In the subsequent chapters, specifics on sample preparation are provided for experiments that diverge from this standard discussed here.

2.2.2 Scanning Force Microscopy Imaging and Peptide Structure Analysis

To interrogate the self-assembly phenomena of solid-binding peptides at inorganic interfaces the structure needs to be visualized with micrometer scale precision. Scanning

probe microscopy (SPM) since its advent with the scanning tunneling microscope has been key to characterization of nanoscale and molecular scale systems. All SPM techniques are based on the raster scanning of a sample surface via lateral x-y positioning of a nanoscale probe controlled by a piezoelectric material or solenoid motor. Interactions between the sample and probe are used to control the probe's z-displacement via a feedback controller allowing for the imaging of the sample surface. The type of interaction used for the feedback control depends on the specific SPM technique. Scanning force microscopy (SFM), also called atomic force microscopy (AFM) in the literature, relies on a combination of long- and short-range interactions, such as electrostatics and van der Waals interactions, between the sample and a probe microfabricated onto the end of a cantilever. As schematized in Figure 2.7, the z-displacement is monitored using a laser reflected off the back of the cantilever and tracked by a photodiode. This general set-up makes SFM an extremely versatile technique for the imaging of a diverse set of material classes under a variety of environmental conditions.

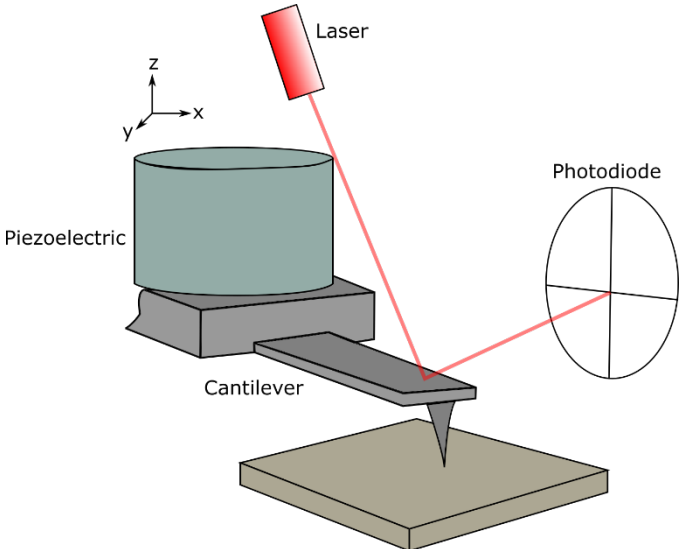

Figure 2.7. Schematic of a scanning force microscope in which a x-y-z piezo raster a nanoscale probe across a sample surface. The tip-sample distance is tracked by reflecting a laser off the cantilever and monitored by a photodiode. Deviations in photodiode signal are used for PID controlling of tip-sample interactions (not shown).

The most commonly implemented SFM variation for the imaging of soft systems, such as the peptide-inorganic interfaces focused on in this work, is dubbed intermittent-contact mode ("Tapping Mode™" or "dynamic mode" depending on company branding). In intermittent-contact mode SFM, the cantilever is driven at a frequency close to its resonance. As the probe comes closer to the sample surface, the intermolecular interactions perturb the cantilever resonance frequency and thus the amplitude and phase of the oscillation. Typically, the probe-sample distance is monitored by keeping the oscillation amplitude constant via a standard PID controller. Intermittent contact mode SFM has a lateral resolution of 2-5 nanometers (as limited by the probes radius) and vertical resolution of 0.1 nanometers allowing for the high-resolution imaging of peptide self-assembly structures. For SFM imaging conducted herein, dried peptide samples were visualized under ambient conditions using a DI Nanoscope IIIa SPM (Digital Instruments) in Tapping Mode™ using soft tapping mode probes (HQ:NSC14/No Al, MikroMasch). Through the analysis of such SFM images a multitude of key structural details can be extracted. Of specific interest to this work are details that can be analyzed in light of theoretical models discussed in Section 2.1 such as : (i) the peptide surface coverage and assembly height (Adsorption – Section 2.1.3) , (ii) the percentage of long-range ordering (Molecular Assembly – Section 2.1.4), (iii) the number of long-range ordered structures (Nucleation – Section 2.1.5), and (iv) the dimensions of those long-range ordered structures.

SFM images presented herein were analyzed using the Gwyddion SPM data analysis software.[47] All images were flattened with a 2D plan fit and the individual scan lines were aligned using built in Gwyddion functionality. Height measurements can most

simply be determined by taking several line profiles of the self-assembly structure and calculating the distance between the top and valley of extracted features. When this technique is employed it is best practice to extract single scan lines and not to analyze line-profiles that include several scan lines as image flattening or processing may distort relative height values. Other structural features are determined by isolating the peptide structures from the underlying substrate via a “masking” process. The peptide mask can then be further edited or analyzed to extract the desired information. Example masking and analysis is presented in Figure 2.8.

Figure 2.8 (a) The images are flattened and cropped to remove graphite step edges or other defects that complicate further processing. (b) A mask is applied to flattened image based on height so that the peptide is clearly distinguished from the underlying graphite surface. Some additional manual editing of the mask was performed to remove erroneously masked graphite when the computer was unable to automatically exclude it. The mask is then filtered by a variety of grain parameters. In part (c) the mask is filtered by grain size. This was often the most effective at separating the ordered and amorphous regions.

For instance, the total surface coverage was determined by first flattening the image and then masking based on height to separate the peptide from the graphite surface. The percent of ordering was deduced from the fraction of the total surface coverage that is part of a long range assembled structure. The ordered regions were subsequently determined by thresholding the initial mask based on either the area or aspect ratio of individual peptide domains. Manual editing of the mask is typically needed

for samples of densely packed peptide to distinguish between ordered and amorphous regions. Statistics on the mask, such as number of ordered domains, average domain size, perimeter, etc. can be further determined for nucleation and growth analyses. At least three one micrometer-square AFM images were analyzed for each sample and averages and standard deviations were determined from all individual image measurements.

2.2.3 Molecular Energetic Determination: Intrinsic Friction Analysis

While high-resolution imaging and structural analyses can provide insights into the assembly and nucleation processes, the molecular complexity of peptide-inorganic interfaces make interrogation of their intermolecular interaction energetics difficult. As will be seen in Chapter 3, peptide adsorption kinetics are non-Arrhenius and, thus, binding energetics are not accurately described. To elucidate the desired energetic information a novel SPM technique dubbed Intrinsic Friction Analysis (IFA) is implemented in Chapter 4. Intrinsic Friction Analysis was originally formulated by Sills and Overney and implemented to interrogate polymeric films.[48-50] IFA is a local energetic analysis based on the well-established lateral force microscopy (LFM),[51] and therefore, provides a molecular and energetic description of relaxation processes that are associated with structural transitions. In IFA, the SFM probe acts as a mechanical scatter by transferring kinetic energy to molecular modes possessed by the material under study, for instance, activating side chain rotations in glassy polystyrene or bonding-debonding interactions for 2D inorganic materials. As demonstrated in Chapter 4, IFA interrogations of self-assembled peptides on 2D surfaces provides the binding energy between the peptide and the substrate, Figure 2.9a.

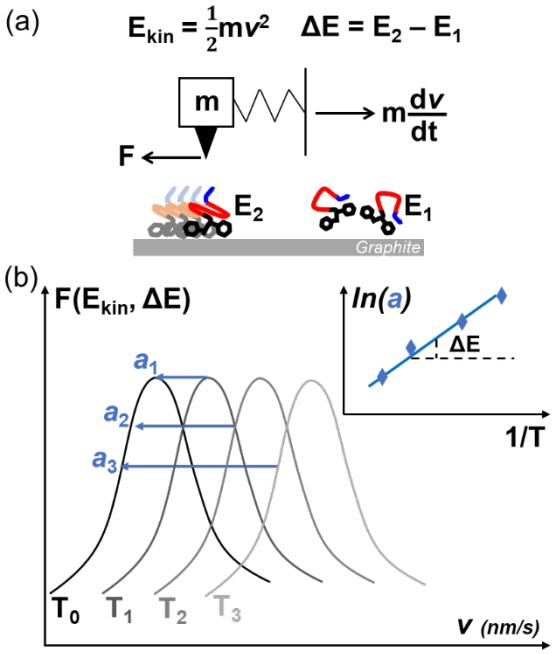

Figure 2.9. (a) Schematic of lateral forces, F, acting on a SPM tip moving at a scanning velocity, *v*, upon coupling with the structural transition between two peptide energetic states at the surface. (b) Illustration of lateral force spectra obtained at different temperatures and the associated thermal shift factors. The inset is the Arrhenius relationship of the shift factors.

Lateral (friction) forces are determined as the hysteresis in the torsional cantilever deflection between forward and reverse scans. To deduce the apparent activation energy of the molecular mode, friction force isotherms are obtained by varying scanning velocities at various constant temperatures. These friction-velocity isotherms are then treated based on the theory of time-temperature equivalence.[52,53] All isotherm curves are superimposed to an arbitrary reference isotherm by shifting them with horizontal distances ln(a_T), where a_T is the thermal shift factor. Shifted isotherms generate a master curve that describes the relaxation landscape of the material making IFA analogous to other relaxation methods such as dielectric spectroscopy and dynamic mechanical analysis. Fast molecular processes that the rate of disturbance, i.e., the scan velocity, cannot reach, are represented by a log-linear line. For slower material relaxation times that can be accessed by the scan velocity, the master curve will contain a characteristic relaxation peak. Enthalpic contributions to the molecular energetics, E_a, are obtained from the thermal shift factor, ln(a_T), as function of inverse temperature using an Arrhenius relationship presented in Equation 2.25, where *R* is the universal gas constant. Vertical

friction shifts, ΔF_F, may also be necessary to generate the master curve and are related to the entropy of the molecular mode as shown in Equation 2.26 in which φ' is the contact area normalized stress activation volume, ΔS is the entropy, and T is the temperature in Kelvin. The decoupling of entropic and enthalpic contributions to molecular energetics is unique to IFA and is not obtainable from other time-temperature superpositions.

$$E_a = -R\left[\frac{\partial \ln(a_T)}{\partial(1/T)}\right]_P \quad Equation\ 2.25$$

$$\Delta F_F \approx -\frac{T\Delta S}{\varphi'} \quad Equation\ 2.26$$

The experimental set-up for IFA is as follows. Friction measurements of the dried peptide samples were obtained using a contact mode stand-alone Explorer SPM (Topometrix, Veeco, CA) with contact mode silicon probes in a low humidity nitrogen atmosphere to avoid capillary formation.[37] The sample stage temperature was controlled using a programmable temperature controller (K-20, MMR Technologies heating stage).[54] Lateral forces were determined as the half-amplitude of the square-wave lateral photodiode signal monitored using an oscilloscope. Lateral forces were scaled using a blind calibration method in which the friction coefficient of a cleaned silicon wafer is obtained and scaled to the known silicon-silicon friction coefficient to determine a geometric calibration factor.[55] The silicon wafer was cleaned by sonicating in acetone and then in methanol for 10 and 40 minutes, respectively. The cleaned silicon wafer is rinsed with deionized water, followed by a 20-minute UV treatment before being dried in a vacuum oven at 120°C under a nitrogen atmosphere for 2 hours to create a natural oxide layer.

Prior to friction measurements the cantilever thickness, *t*, was calculated using the out-of-contact normal cantilever resonance frequency, f_c [Hz], via Equation 2.27. From the calculated thickness, *t* [m], known cantilever length, *L* [m], width, *W* [m], and elastic modulus, *E*, the cantilever spring constant, k_N, was determined using Equation 2.28.

$$t = 0.000723 L^2 f_c = [m] \quad Equation\ 2.27$$

$$k_N = \frac{E t^3 W}{4L^3} \quad Equation\ 2.28$$

During IFA experiments the total normal force, F_N, is kept constant to maintain isobaric conditions. The total normal force, F_N, is calculated using Equation 2.29, by taking into consideration the apparent contact stiffness, *S*, of the cantilever and the adhesion force, F_{adh}, between the probe and sample as extracted from force-distance curves, the out-of-contact top-bottom photodiode signal, F_{TB}, and the applied force, F_{App}.

$$F_N = \frac{k_N}{S}\left(F_{App} + F_{Adh} - F_{TB}\right) \quad Equation\ 2.29$$

Friction-velocity isotherms were generated by scanning 1 mm × 1 mm areas with a low resolution of 25 lines per scan to prevent memory effects from prior scans. Friction measurements were averaged over multiple scans at the same scan velocity and temperature. To generate the isotherms, measurements were taken at least five temperatures and six scan velocities.

2.2.4 Scanning Tunneling Microscopy and Spectroscopy

The prior sections on scanning probe microscopy detailed how insights into the self-assembly process and intermolecular energetics can be experimentally elucidated. This section details how device relevant electronic properties of the self-assembled

interface can be interrogated through the application of scanning tunneling microscopy and spectroscopy. The scanning tunneling microscope (STM) was the first member of the SPM family developed in 1981 by Binnig and Rohrer and catapulted the field of Nanotechnology to the forefront of scientific research.

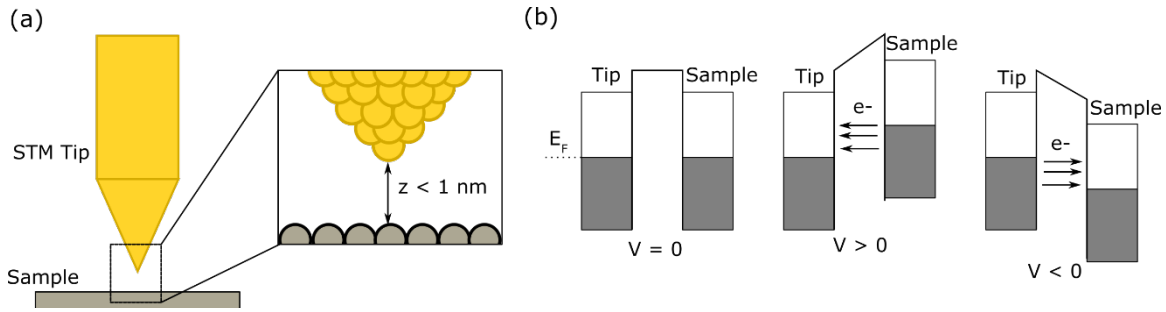

Figure 2.10. (a) Schematic of metal-insulator-metal (MIM) junction created by a conductive STM tip with an atomic asperity with a conductive sample. (b) Electron tunneling within the MIM junction is controlled by the voltage difference between the tip and sample. Applying a bias raises electron energy levels of either the tip or sample above the Fermi energy level allowing for electrons to pass across the junction.

While SFMs rely on long- and short-range interactions between the probe and surface to track surface features, the STM uses the tunneling current between an atomically sharp conductive tip and conductive sample as schematized in Figure 2.10. To get electrons to tunnel between the tip and sample, a voltage is applied to excite electrons above the Fermi level of the tip (or sample depending on the direction of the bias). As the tunneling current depends exponentially on the distance between the tip and sample, small variations in tunneling current that occur while scanning the tip across the sample surface at a constant tip-sample bias are translated into an STM image. STM image features represent the local magnitude of the tunneling current and, thus, are a combination of topographical surface features and surface electronic properties. The exponential dependence of the tunneling current with the tip-sample distance combined with an atomic probe radius, STM allows for higher resolution imaging over SFM.

Beyond the gap distance, *z*, between the probe and sample, the tunneling current, *I*, is greatly affected by the density of states at the Fermi level, $D_s(E_F)$, the bias *V*, and the potential barrier or work function, φ, as shown in Equation 2.30.

$$I \propto VD_s(E_F)\exp\left(-1.025\sqrt{\varphi}\times z\right) \quad Equation\ 2.30$$

In addition to high resolution imaging, scanning tunneling microscopes can be used to interrogate the local current voltage (I-V) characteristics of the sample and insulating junction between the tip and sample. Scanning tunneling spectroscopy (STS) can be determined by monitoring the tunneling current as a function of voltage at a constant z value. The first derivative of this I-V spectra provides experimental access to probe the local work function and local density of state of the material. For peptide-inorganic interfaces, this may provide information about doping of the inorganic material by the peptide which will affect device characteristics.

2.2.5 Molecular Dynamics Simulations

While experimental interrogations previously outlined can provide a multitude of insights into how peptide sequence and environmental conditions affect the self-assembly structure and process, atomistic details of the peptide-inorganic interface are still inaccessible. Computational approaches, and in particular, molecular dynamics simulations allow for the atomic level description of molecular conformations, interactions and energetics that can be corroborated by and flesh-out experimental data.

For molecular simulations, molecules are represented by a collection of point particles with simple mechanical model representations for interactions. Non-bonded interactions are represented using a combination of Lenard-Jones potentials and

electrostatic potentials. The specific formulation and parameters used to represent the potentials depend on the force field used. Nonetheless, the total interaction potential, *U*, for a molecular system is given by the summation of the bond, angle, dihedral, van der Waals and electrostatic energies as seen in Equation 2.31. Table 2.2 provides general representations for the bonded and non-bonded interactions present in molecular mechanics models.

$$U = E_b + E_\theta + E_\varphi + E_{vdw} + E_{elec} \quad Equation\ 2.31$$

Table 2.2. Molecular Mechanics Equations

Interaction Type	**Mechanics Model**
Bonded	$E_b = \sum_i K_{b,i}(b_i - b_{0,i})^2$
Angle	$E_\theta = \sum_i K_{\theta,i}(\theta_i - \theta_{0,i})^2$
Dihedral	$E_\varphi = \sum_i K_{\varphi,i}\left[1 - \cos\left(n_i \times (\varphi_i - \varphi_{0,i})\right)\right]$
van der Waals	$E_{vdw} = \sum_{i,j}\left[\varepsilon_{i.j}\left(\frac{r_{0,ij}}{r_{ij}}\right)^{12} - 2\varepsilon_{i.j}\left(\frac{r_{0,ij}}{r_{ij}}\right)^{6}\right]$
Electrostatics	$E_{elec} = \sum_{i,j}\left(\frac{q_i q_j}{r_{ij}}\right)$

K is the spring constant of the interaction. *b* and b_0 are the bond length and equilibrium bond length, respectively. θ and θ_0 are the bond angle and equilibrium bond angle, respectively. φ and φ_0 are the dihedral angle and equilibrium dihedral angle, respectively. r_{ij} is the distance between the two atoms, *q* is the charge of the atom, and ε_{ij} is the dielectric constant. These parameters are tailored for every force field to achieve accurate results.

By applying a time-dependent integration of the total interaction potential allows for the determination of forces acting on every atom contained within a molecule. Using standard Newtonian mechanics, the velocities of every individual atom can be calculated for small timesteps. This process allows for the simulation of a molecule's dynamics and conformational properties. In this work, molecular dynamics simulations are used to study

the conformational space of peptides in aqueous solution and at inorganic surfaces. Several force fields have been developed from a combination of first-principle calculations and fits to experimental data. In the work presented here the four different force fields have been used; namely, the *in lucem Molecular Mechanics* (ilmm) package with a flexible three-center (F3C) water model, the OPLSe force filed with the TIP3P water model, and the CHARMM27 force field with Interface Force Field modifications.[56-61] Specific simulation approaches are addressed in the following chapters.

As discussed in Section 2.1.1, the conformational space of the short peptides of interest in this work is extraordinarily complex and is, therefore, not adequately searched by standard molecular dynamics approaches. Several enhanced sampling techniques have been developed to search the conformational and configurational space of molecular systems more thoroughly, e.g., Monte Carlo, umbrella sampling, replica exchange.[62,63] In this work we implement metadynamics to explore the peptide's conformational space throughout the entire adsorption process.[64-66] In metadynamics, history dependent gaussian biases are applied to variables, $\vec{s}$, (called collective variables, or CVs) with slow dynamics to force the molecular system to search the unsampled regions of the thermodynamic landscape. The gaussian biases, *V*, have the mathematical form:

$$V(\vec{s}) = \tau \sum_{j=0} \omega \exp\left(-\frac{1}{2}\left|\frac{\vec{s} - \vec{s}_j}{\vec{\sigma}}\right|^2\right) \quad Equation\ 2.32$$

where τ is the time step, ω is the deposition rate of the gaussian function, $\vec{\sigma}$ is the width of the gaussian, and $\vec{s}_j$ is the value of the collective variable at an instantaneous timepoint in the simulation. The free-energy landscape of the system can be directly reconstructed

by summing the gaussian biases and allows us to understand the conformational propensities of the peptide and the energetics of the peptide-substrate binding energetics.

Chapter 3:
Thermal Selection of Peptide Conformations for Self-Assembly

3.1 Introduction

Molecular self-assembly involves spontaneous structuring or self-organization of molecules in solution and at interfaces and is a key strategy in building biological architectures and molecular machines that execute life's functions.[67-70] Inspired by nature, a wide variety of methods have been developed to aid nanoscale organization of molecules and nanomaterials in solution and at free surfaces enabling bottom-up fabrication in both nano- and bio-technologies.[71-73] Molecular assembly relies on relatively weak forces, such as van der Waals (VdW), hydrogen bonding, and electrostatic interactions.[74,75]

In biomolecular systems, monomer structural differences profoundly affect self-assembly due to the orientational dependence of intermolecular interactions, and, the increased conformational degrees of freedom of the molecule. This conformational dependence of the self-assembly process typically necessitates interactions between monomers with well-defined biomolecular structures and chemistries, *e.g.* "lock-and-key" associations, as found for ligand-receptor or antibody-antigen interactions.[76,77] Biomolecules either possess well-defined structures, or adopt them upon interacting with their binding partners, described by the "induced fit model".[76] Due to the complexity and specificity of biomolecular interactions, biomolecules have garnered interest as a means of engineering complex hierarchical assemblies of technological importance.[78-84] Traditional kinetic models apply to the assembly of thermally stable biomolecules, such as micelle formation, fibrillation, *etc.*, enabling their use in engineering applications.[80,85,86]

Conformational dependences of biomolecular interactions can be utilized to dynamically control assembly by inducing an “active” conformational state, *e.g.* cytoskeleton filament assembly.[70,87,88] Well-defined structures are not *a priori* required for assembly, as long as there exists a conformational state that leads to assembly. Intrinsically disordered proteins, a class of biomolecules ranging from completely unstructured to dynamically structured conformations, highlight the phenomenon of self-assembly with metastable conformational states with increased intermolecular interactions.[89-92]

Peptides genetically selected to bind to metal, ceramic and mineral surfaces are commonly viewed as part of this class of intrinsically disordered biomolecules.[21,93,94] Despite the assumed structural disorder of solid binding peptides (SBPs), some exhibit long range ordered assembly on solids for which they were selected.[31,32] The material-specificity and self-assembling capability of SBPs are core in their use as molecular linkers, assemblers, and inorganic synthesizers for bio-enabled technologies.[25-27,95,96] The assembly process of SBPs has been shown to depend on the adsorption kinetics and strength, surface diffusion, and intermolecular interactions between peptides.[31] For example, two chemically similar graphite binding peptides that differ in the composition of the C-terminal aromatic residues (GrBP5-WT and GrBP5-M2), detailed in Figure 3.1, assemble into two different structures on graphite.[31] As was previously published, GrBP5-WT (WT) form long-range ordered nanostrips up to microns in length with six-fold symmetry, mirroring the underlying graphite lattice. GrBP5-M2 (M2), on the other hand,

form confluent amorphous films. The difference in assembly was attributed to increased aromaticity of M2 leading to tighter binding and slower surface diffusion.[31]

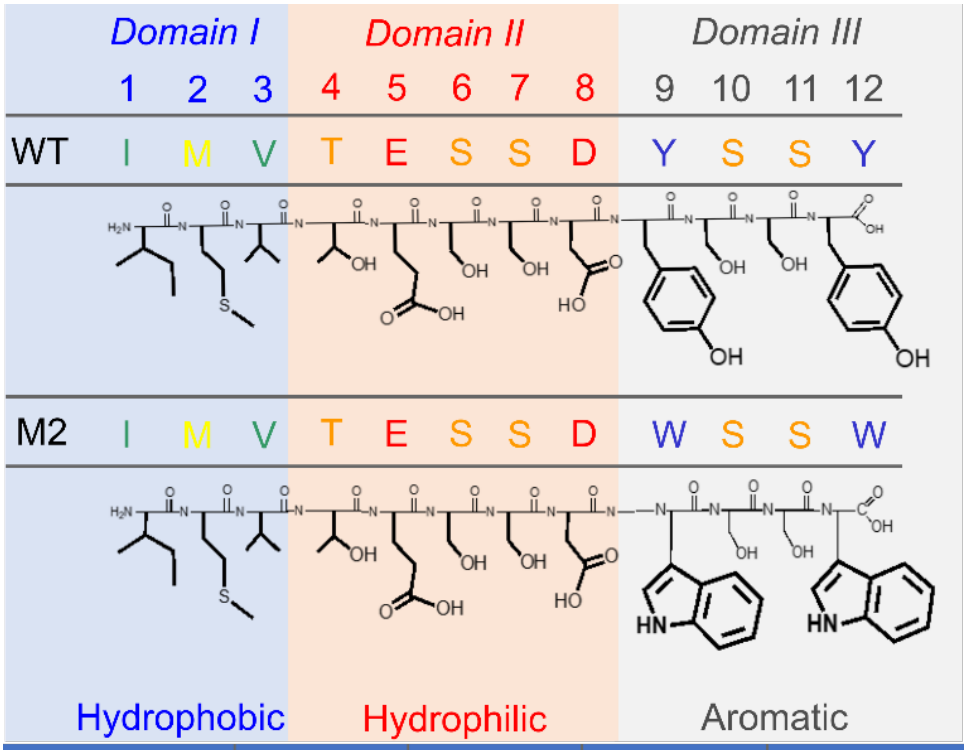

Peptide	MW	Charge	pI	GRAVY
GrBP5-WT	1383.4	-2	3.55	-.242
GrBP5-M2	1427.5	-2	3.55	-.175

Figure 3.1. Sequence and physical properties of GrBP5-WT and GrBP5-M2. The displayed charge is the net charge of the peptide at pH 7, in which the N and C terminus as well as the central E and D are charged. The molecular weight (MW) is in Daltons. The isoelectric point, pI, was determined using the IPC – Isoelectric Point Calculator.[1] The Grand Average Hydropathy (GRAVY) scores were determined as the sum of the individual amino acid hydropathies divided by the length of the peptide. The color coding for the amino acids is as follows: green – hydrophobic, yellow – sulfur containing, red – charged, orange – hydrophilic, blue – aromatic.

Since the observed SBP assemblies exhibit low-dimensionality and high coordination, it is reasonable to assume the assembly process/structures rely on orientationally and structurally sensitive interactions, as discussed above. Thus, it is necessary to complement the underlying adsorption and assembly parameters of SBPs with information about the conformational state (or states) of the peptides in solution. For instance, sequence differences between WT and M2 could result in different

conformational or structural states in solution, and exhibit disparate responses to environmental conditions, such as temperature. In this light, the "rigid" monomer structure description of molecules must be replaced by a “soft” conformable depiction of the peptide structure in solution. This dynamic interpretation of structure suggests that solution conformational states could be biased to favor a particular self-assembly via changes in the solution environmental condition, *e.g.*, incubation temperature. To predict and direct the assembly of SBPs, an understanding of how sequence and environmental conditions affect the peptide structure and the assembly must be developed. To this end, we investigate here (i) the energetic and structural effects of temperature on self-assembly with thermal and kinetic property experiments, in addition to (ii) molecular mechanics simulations of the solution dispersity of peptide conformations.

3.2 Experimental Methodology

3.2.1 Peptide Synthesis

The GrBP5-WT and GrBP5-M2 were synthesized in-house using an automated solid-phase peptide synthesizer (C2336X, CSBio Inc., Menlo Park, CA) employing standard batch process Fmoc (Fluorenylmethyloxycarbonyl) chemistry procedures as reported previously.37 Fmoc deprotection was achieved using 20% piperidine in dimethyl formamide (DMF) and the reaction efficiency was monitored by UV absorbance at 301 nm. The peptides were cleaved from the resin and side chains were deprotected via mixing in a cleavage “cocktail” for 2 hours under a N2 atmosphere. The cleavage cocktail contained trifluoroacetic acid (TFA) / thianisole / diH2O / phenol / ethanedithiol (EDT) (87.5:5:5:2.5) or TFA / tri-isopropylsilane / diH2O / EDT (94:1:2.5:2.5) for GrBP5-WT and GrBP5-M2 respectively. The peptide was separated from the resin, subsequently

precipitated with cold ether, and reconstituted using various ratios of deionized water and acetonitrile. Purification by HPLC (Waters Deltaprep 600, Semi-preparation Mode) was performed using a linear gradient of 1% per minute at a flow rate of 10 mL/min. Retention times were anywhere between 30 and 50 minutes. The synthesized peptide's molecular weight was confirmed by MALDI-TOF mass spectrometry (Autoflex II, Bruker Daltonics, Billerica, MA). Spectra are provided in the supplementary materials.

3.2.2 Isothermal Peptide Assembly

Highly-oriented pyrolytic graphite (HOPG, Grade 1, SPI Inc.) was mechanically cleaved with scotch tape and attached via double sided tape to steel pucks. For peptide assembly, 40 µL of either 500 nM, 1 µM, 2.5 µM, or 5 µM peptide in deionized water was incubated for 3 hours on a freshly cleaved HOPG surface in a chamber with saturated water vapor at temperatures from 5°C to 47°C. After the incubation time elapsed the peptide solution was wicked from the surface using a laboratory tissue paper and subsequently dried under a gentle nitrogen flow for at least 30 seconds.

3.2.3 Non-Isothermal Peptide Assembly

Two sets of dynamic heat-treatment experiments were performed to differentiate between thermal effects on solvated peptide structure versus peptide surface dynamics. In the first set of experiments, 200 µL of 2.5 µM peptide was heated to an elevated temperature (37°C for WT and 47°C for M2). After 15, 30, and 60 minutes of exposure to heat, 40 µL of the heated peptide solution was quenched to room-temperature and incubated on a freshly cleaved HOPG surface (see substrate preparation above) in a chamber with saturated water vapor for 3 hours. To test the effect of temperature on the peptide surface dynamics, 40 µL of peptide solution was incubated at room temperature

on HOPG surfaces for 1 hour, at which point the sample was exposed to an elevated temperature for an additional 3 to 6 hours. The samples were dried using the same procedure as isothermal experiments.

3.2.4 AFM Imaging and Image Analysis

Dried self-assembled peptide samples were kept in a dry environment until imaged by atomic force microscopy (AFM Nanoscope IIIa, Digital Instruments) in tapping mode under ambient conditions using soft tapping mode AFM probes (HQ:NSC14/No Al, MikroMasch). AFM images were analyzed using Gwyddion 2.52 analysis software (gwyddion.net). Images were flattened and corrected for line errors. Total surface coverage was determined by masking the AFM images based on a threshold height that distinguished the peptides from the HOPG surface. The percent of ordering was deduced from the fraction of the total surface coverage that is part of a long range assembled structure. These regions were determined by thresholding the initial mask based on either the area or aspect ratio of individual grains. For samples of densely packed peptide, manual editing of the mask was used to distinguish between ordered and amorphous regions. Example masking and analysis is available in the supplementary material. At least three one micrometer-squared areas were analyzed for each sample. Averages and standard deviations were determined from all individual image measurements.

3.2.5 Molecular Dynamics Set-up and Analysis

Simulations were performed using the in lucem Molecular Mechanics (ilmm) package with the microcanonical NVE (constant number of particles, volume, and energy) thermodynamic ensemble, and the flexible three-center (F3C) water model.43-45 All simulations were performed at 298 K, pH 7, with no additional salt. Protein Data Bank

(PDB) files were built using UCSF Chimera (www.cgl.ucsf.edu).46 Hydrogen atoms were modeled onto the protein structure and minimized for 500 steps of steepest gradient minimization. Afterwards the entire system is minimized for an additional 1000 steps. Water molecules were subsequently added, minimized for 100 steps, simulated for 500 steps, and minimized for an additional 500 steps. The peptide was then minimized in the presence of the water for 500 steps. An unbiased extended starting structure (Φ, Ψ = 180°) was simulated for 5-ns to generate a slightly collapsed structure to be used for the subsequent 200-ns simulation. An 8 Å buffer region of water was used to prevent edge effects.

(Φ, Ψ) pairs were binned into a 2D histogram with 72 × 72 bins comprising 5° × 5° increments. The bins were scaled by the total number of (Φ, Ψ) pairs generating a population distribution for the backbone angles. These backbone angle distributions were used to calculate entropy values using $S= - R\sum A(i,j) \ln[A(i,j)]$, in which A is a population distribution and A(i,j) is the population density in one 5° × 5° bin. Free energy values for conformational states were determined using $G = -RT \times \ln[p_i/(1-p_i)]$, in which p_i is the probability of the conformational state based on the relative frequency of the state versus all observed states. The frequency and number of conformational states was obtained by ensemble clustering implemented in UCSF Chimera.

3.3 Results and Discussion

3.3.1 Kinetic and Structural Analysis

To test the thermal effects and to probe the energetic landscape of WT and M2, we analyzed experimentally the equilibrium structures resulting from a variety of isothermal incubations. Atomic force microscopy (AFM) images displayed in Figure 3.2a reveal for WT comparable equilibrium surface coverages at 23°C and 5 °C. At these incubation temperatures, the degree of ordering is above 60% for all samples with solution concentrations greater than 1 μM. Estimation of the equilibrium kinetics from

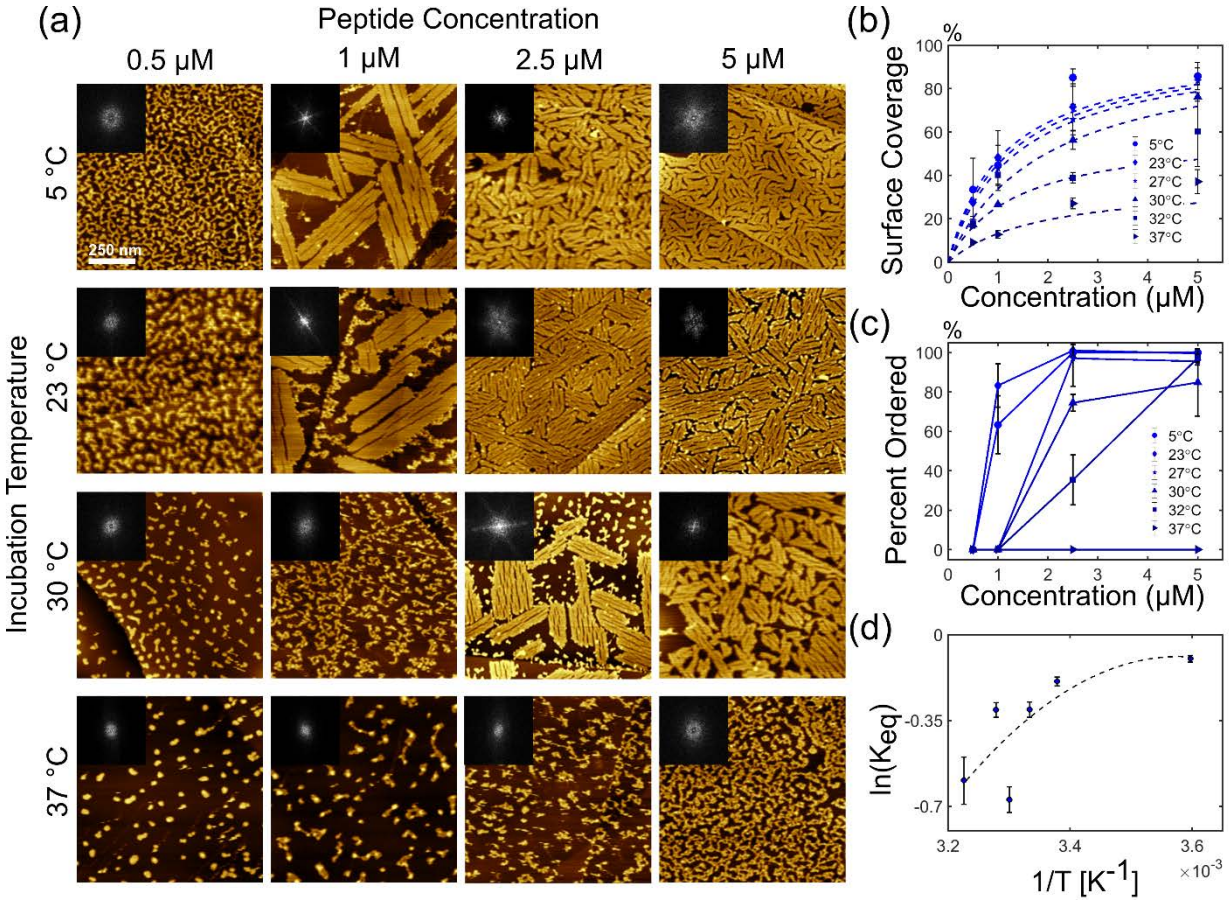

Figure 3.2. WT Isothermal Assembly (a) Representative images of GrBP5-WT assembled structure for a variety of incubation temperatures and peptide concentrations. All images are 1 μm^2 and insets are Fast Fourier Transforms (FFTs) of the image. (b) Langmuir isotherms of equilibrium surface coverage. Dashed lines are fits from the Langmuir adsorption isotherm. (c) Percent ordering observed for each incubation condition tested. (d) Arrhenius plot of estimated equilibrium adsorption kinetic rates versus temperature showing non-linear relationship. Guiding line is a quadratic fit to show non-linearity only.

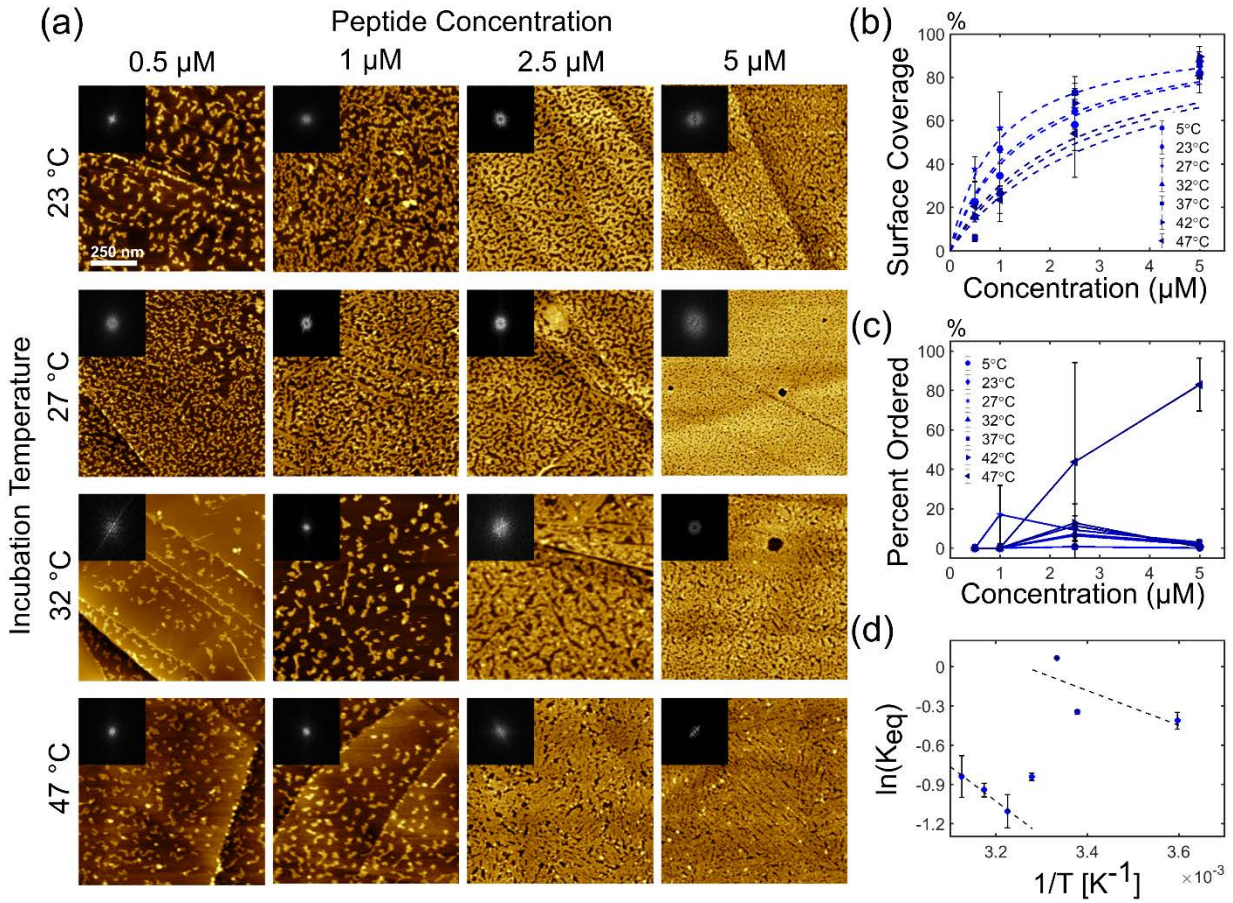

Figure 3.3. Isothermal M2 Assembly. (a) Representative images of GrBP5-M2 assembled structure for a variety of incubation temperature and peptide concentrations. All images are 1 µm^{2}and insets are Fast Fourier Transforms (FFTs) of the image. (b) Langmuir isotherms of equilibrium surface coverage. Dashed lines are fits from the Langmuir adsorption isotherm. (c) Percent ordering observed for each incubation condition tested. (d) Arrhenius plot of estimated equilibrium adsorption kinetic rates versus temperature showing non-linear relationship. Two linear fits are displayed to show discontinuity.

Langmuir fits, Figure 3.2b, show that adsorption kinetics and equilibrium surface coverages of WT decrease when the incubation temperature is increased beyond 23 °C. Similarly, the degree of ordering decreases with increased incubation temperature, Figure 3.2c. Samples incubated at 37 °C had a maximum surface coverage of ~40 % and exhibited no ordering, even at high solution concentration of 5 µM.

In contrast to WT, the maximum surface coverage for M2 remains high (80 to 90%) for concentrations of 2.5 and 5 µM up to 47°C incubation temperatures, as revealed by AFM images and Langmuir isotherms in Figure 3.3a and 3.3b, respectively. The

equilibrium surface coverage at lower concentrations is more variable and affected by the incubation temperature. The degree of ordering in M2 samples, Fig. 3.3c, increases with elevated incubation temperature reaching above 80 % for 5 μM samples incubated at 47°C. Although increasing temperature aids M2 assembly, the results are inconsistent and do not follow an obvious trend with temperature. For example, more ordering was observed at 27 °C than at higher temperatures for 1 μM samples. Only the 2.5 μM samples followed the expected trend of increasing ordering with increasing temperature. The lack of observed ordering for 5 μM samples may be attributed to the high packing density in these samples. High packing density provides two challenges: (i) Restricted surface diffusion, and, thus annealing towards ordered assembly structures, as well as, (ii) Experimental difficulties in distinguishing the ordered from amorphous regions.

The equilibrium adsorption kinetics for both WT and M2 are non-Arrhenius, *i.e*., not loglinear with inverse temperature, as shown in Figure 3.2d and 3.3d. Non-Arrhenius adsorption, with temperature dependent activation energies, suggests the structural dispersity of the peptide in solution changes, given the adsorption of biomolecules has been shown to depend on the solvated conformation.[97,98] We observed aggregation (bright globular structures in Figure 3.2a and 3.3a) at high temperature and low concentration for both WT and M2 samples, reducing the accuracy of the Langmuir fits for adsorption kinetics.

For WT, the non-Arrhenius behavior is a continuous curved line that can be interpreted as denaturation, or, increased dispersity of the solvated structures. Increasing the incubation temperature results in reduced adsorption and subsequent loss in degree of ordering. In contrast to WT, non-Arrhenius behavior observed for M2 is discontinuous,

with two regimes separated by a transition at a critical temperature around 30 °C (Figure 3.3d). Above this critical temperature, ordering in M2 samples increases, especially for 2.5 μM samples (Figure 3.3c). We attribute this transition to a change in the structural dispersity towards a conformation with a higher propensity of ordering at the surface.

3.3.2 Deconvoluting Solution and Surface Dynamics

The non-Arrhenius adsorption kinetics for WT and M2, Figure 3.2d and 3.3d, suggest a temperature dependent chemical potential difference, Δμ(T), between the solvated peptide's self-energy and the self-energy of the adsorbed states. To investigate our hypothesis that changes in Δμ are a result of thermally induced conformational changes of the solvated peptides, we conducted non-isothermal assembly experiments (Figure 3.4a). Briefly, 2.5 μM peptide solutions were exposed to an elevated temperature

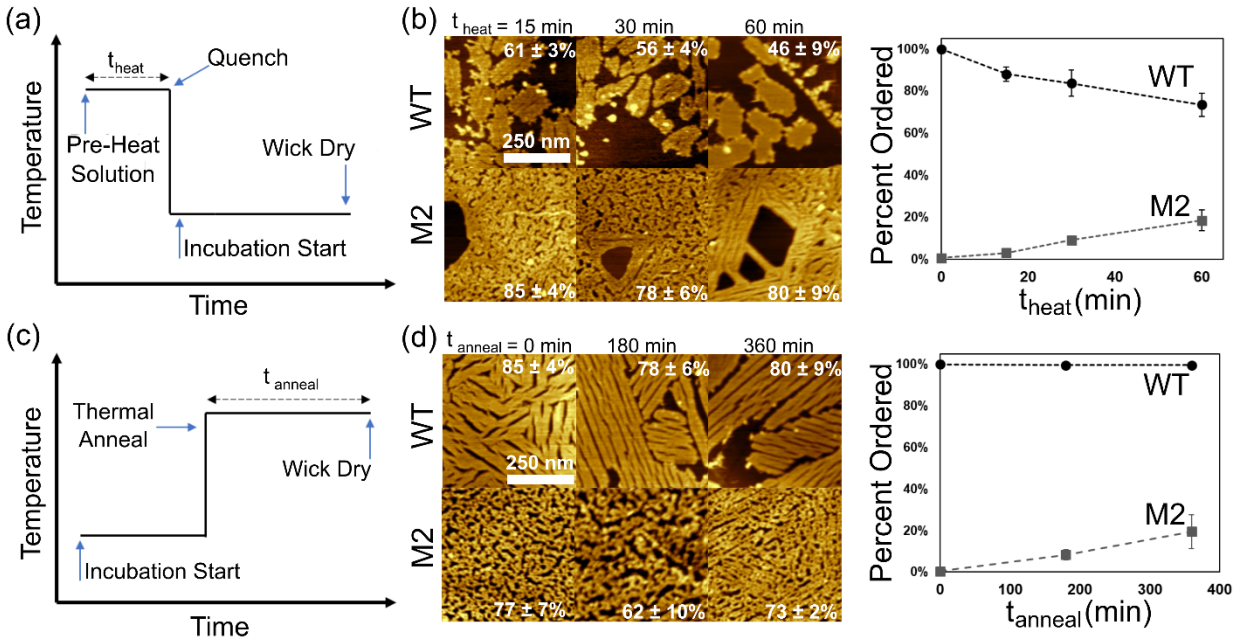

Figure 3.4. Non-isothermal Assembly. (a) Schematic of the non-isothermal procedure used to obtain the data presented in (b). (b) Representative images of the self-assembled structures of WT and M2 as a function of exposure time to elevated pre-incubation temperatures. Quantification of the degree of ordering present in the self-assembled structures is displayed to the left. (c) Schematic of the non-isothermal procedure used to obtain data presented in (d). (d) Representative images of the self-assembled structures obtained from pre-incubating the peptide and thermal annealing for different durations (right) and the quantification of the degree of ordering (left). A temperature of 37°C was used for WT samples while M2 was exposed to 47°C. Inset percentages on AFM images are the total surface coverage of the samples.

prior to introducing them at room temperature to HOPG surfaces for 3 hours. A 2.5 μM solution concentration was chosen for its clear change in assembly properties for both WT and M2 in isothermal experiments.

As shown in Figure 3.4b, increasing the exposure time of the peptide solution to elevated temperatures, improved the degree of ordering for M2, while slightly impeding the ordering of WT. The surface coverage of WT samples decreased from 87% to 45% upon exposure to 1 hour of elevated temperature, corroborating the change in adsorption kinetics observed in isothermal experiments to be in part due to thermal effects on the solvated peptide conformation. The lack of ordering in isothermal experiments of WT can be interpreted to originate from an increase in the desorption rate at elevated temperatures, affecting the aggregation and assembly. The surface coverage of pre-heated M2 remained high for all exposure times, as expected from isothermal experiments. These results corroborate the hypothesis that thermal energy affects the peptide in solution, and consequently leads to a different self-assembled structure.

Although preheating M2 in solution biased the peptide towards assembly, the extent of ordering is lower than observed for isothermal assembly. Peptide self-assembly on solid-surfaces is a multistep process involving the solution state, adsorption, diffusion and peptide-peptide interactions; all of which can be thermally modulated. To further interrogate the effects of temperature on the surface dynamics of the peptide, a second set of non-isothermal experiments were performed, Figure 3.4(c-d), in which room-temperature peptide solutions were incubated on a fresh HOPG surface for 1 hour before “annealing” the incubated sample at an elevated temperature for three hours. The assembly structure of WT from a room-temperature peptide solution showed to be

unaffected, *i.e.,* thermally stable after annealing for 6 hours at 37 °C, Figure 3.4d(top). The M2 assembly, on the other hand, showed an increase in ordering at a rate of approximately 10% every 3 hours, Figure 3.4d(bottom), implying the assembly process to be thermally activated on the surface, albeit a slower kinetic rate.

Combining the isothermal and non-isothermal experimental results, it can be concluded that peptide self-assembly is dependent on the solvated conformation. In the case of WT, peptides can be primed conformationally for assembly at room-temperature and colder incubations. Increasing the thermal energy of the peptide solution denatures the solute conformation leading to lower adsorption coverage and rate, thus, impeding ordering, as demonstrated in Figure 3.2a, 3.2d and Figure 3.4b. For M2, the transition to a conformation with higher propensity of ordering is similarly controlled via the temperature and can occur either in solution or at the surface. However, as demonstrated by the isothermal experiments, the combination of thermal exposure through-out the assembly process greatly enhances the adsorption kinetics, as well as, the degree of ordering.

3.3.3 Simulated Structural Propensities and Energetics

The experimental results highlight the role of solvated GrBP5 conformations in the peptide assembly kinetics and structure. To further elucidate the structural and energetic differences between WT and M2 in solution, we modelled their conformational propensities using *in lucem Molecular Mechanics* (*ilmm*).[60] To identify stable conformational states, an automated clustering algorithm within *UCSF Chimera* was implemented.[99] The theoretical analysis revealed 56 distinct conformational states for WT, and 80 states for M2. Representative structures from the top three most frequent

conformational states are shown in Figure 3.5a, along with a composite structure of the three states superimposed. For WT, states 1, 2, and 3 composed 35%, 15% and 8% of the 200 ns simulation, respectively. For M2, states 1, 2, and 3 composed 27%, 13%, and 9% of the simulation time, respectively. All other observed conformational states for WT and M2 compose the remaining 42% and 51% of their respective simulations. Individually, these infrequent states each lasted for less than 7% of the simulation. Additional discussion on ensemble clustering and structural transitions can be found in the supplementary.

As evidenced by the representative structures in Figure 3.5a, amino acids Val-Thr-Glu-Ser form an α-helical structure in both peptides. Based on the residence time, the α-helix is more stable in WT than M2. Composite structures of states 1, 2, and 3 for WT, Figure 3.5a, shows the overall conformation is (i) quite similar regarding the high structural overlap for the α-helix, and, (ii) different in the relative location of the tyrosine rings. For M2, states 1 through 3 show little structural overlap since (i) state 1 lacks the α-helix present in the other states, and (ii) the α-helices in state 2 and 3 do not align as observed with WT. Thus, WT is more uniformly structured in solution than M2. Inspection of amino-acid contacts revealed that Trp12 in M2 made frequent contacts with the N-terminal amino acids potentially destabilizing the observed secondary structure. These side-chain contacts were much less frequent with Tyr12 in WT providing a rationale for why the substitution of Trp affects the molecular structure of the peptide. This suggests that truncating the peptide to remove Trp12 may stabilize the structure.

Additional structural comparisons between WT and M2 are provided in greater detail in the supplementary. Backbone angle population distributions of WT and M2 were

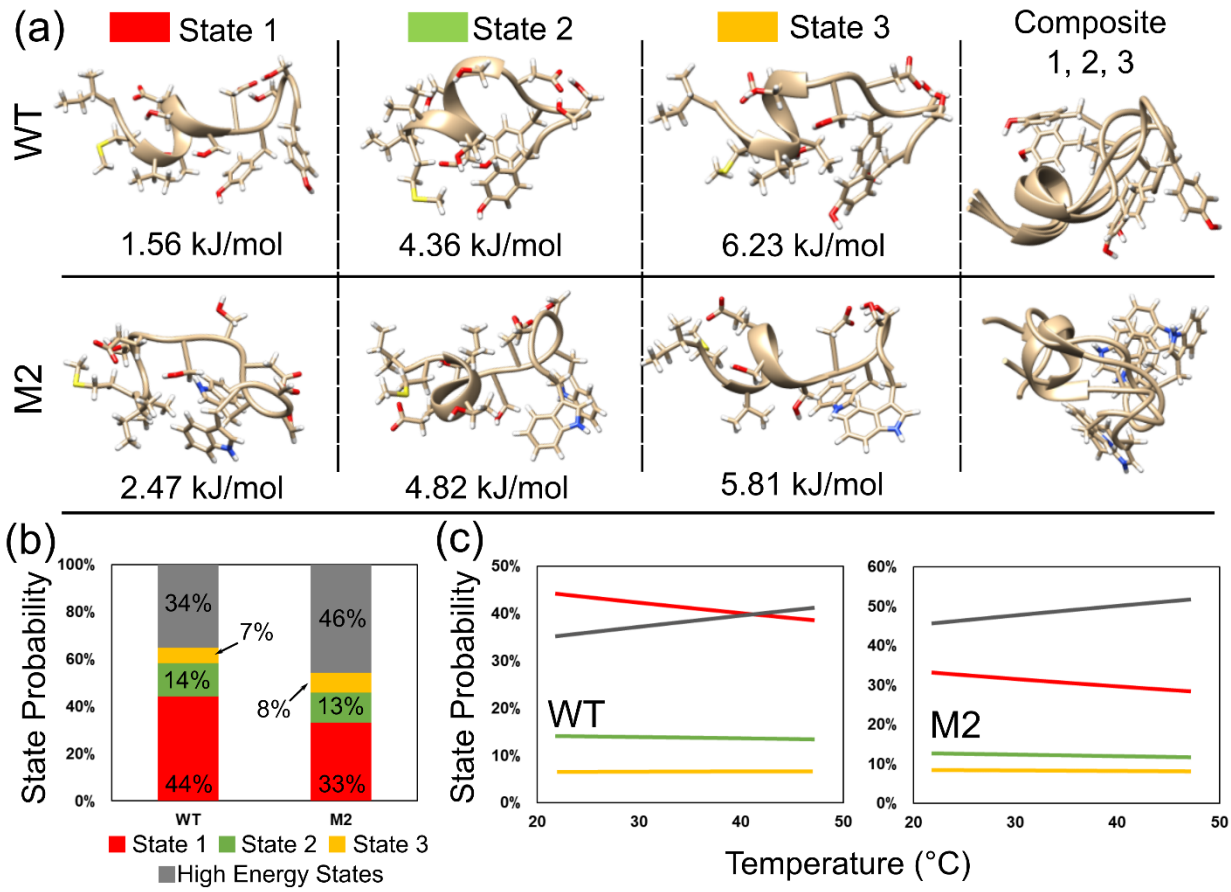

Figure 3.5. Conformational Propensities and Energetics of Solvated GrBP5s. (a) Representative structures of the three most stable states as determined by proportion of simulation time and ensemble clustering. The inset energetic values are based on the probability of the peptide being in the given conformational state out of all the observed states during the 200 ns simulation using $G = -RT \times \ln[p_i/(1- p_i)]$ in which p_i is the probability of the state. The comparison of the three states was obtained by aligning the peptide by amino acid sequence and orienting to obtain the lowest Cα RMSD value. (b) The room-temperature structural dispersity of the solution state was estimated using a Boltzmann distribution, and the free energy estimates based on conformational state probabilities. The high energy states are the collection of infrequent states observed for the respective peptide (n= 53 for WT and n=77 for M2). (c) The temperature dependence of the solution dispersity for WT and M2 was then estimated using the same Boltzmann distribution.

similar, however M2 sampled more conformational space suggesting greater conformational entropy. From said angle distributions, backbone entropies for WT and M2 were estimated as 563 and 597 J/mol K, respectively. Using the relationship between frequency/probability and energetics, we estimated the free energy values for all the observed conformational states. For states 1, 2 and 3, *i.e.*, the lowest energy states, we estimated free energies of 1.56, 4.36, and 6.23 kJ/mol, respectively, for WT, and energies of 2.47, 4.82, and 5.81 kJ/mol for M2 (Figure 3.5a). All other observed conformational

states for WT and M2 were determined to be high energy states given their low frequency. It is important to note that for WT, the free energy differences between state 1 and the other states exceeds the molar thermal energy, *RT,* at room temperature, while the energy differences between all M2 conformational states is less than the molar thermal energy. This goes along with the suggestion that M2 is more structurally disperse in solution than WT at room temperature.

To estimate the structural dispersity differences between solvated WT and M2, we determined the probability of every observed conformational state using Boltzmann statistics (Figure 3.5b). At room temperature, the lowest energy WT state, state 1, is the most probable conformation (44%), outnumbering the collection of all the high energy infrequent states. For M2, the collection of high energy infrequent states is the most dominant (46%). If we assume that the adsorption rates of the various conformational states are on the same order of magnitude, then we can assume that the surface adsorbed M2 is similarly disperse to the solution state. This finding supplements our experimental results by elucidating the non-uniformity of solute conformation as cause for M2 forming an amorphous rather than ordered room-temperature assembly. Assembly of a more conformationally uniform peptide in solution, like WT, is not impeded by an additional kinetic conformational transition.

Estimation of the solution dispersity as a function of temperature shows that at approximately 40 °C the collection of high energy WT states, *i.e.*, all states besides states 1, 2 and 3, overcome state 1 to be the most probable in solution (Figure 3.5c). This finding further suggests denaturation as the mechanism leading to the experimentally observed decrease in adsorption and degree of ordering. For M2, the collection of high energy

states remains the most probable with increasing thermal energy. The experimentally observed increase in ordering for M2 then can be interpreted as a result of populating an infrequent state with greater propensity to assemble. State 3 of M2 is one such conformational state given it is within 0.6 Å RMSD of WT's state 1. However, the population increase of M2's state 3 is minimal compared to the increase in the high energy states (Figure 3.5c). Since our analysis relies on conformational states observed at 298K, the sampling of high energy states of interest is limited, *i.e.*, the conformational state of interest could not have been observed in our simulations.

The presented computational results supplement our experimental analysis of WT and M2 on HOPG and broaden our understanding of polypeptide assembly and thermal effects prior and post assembly. Taking the experimental and computational results collectively an assembly mechanism for graphite-binding peptides can be developed. As schematized in Figure 3.6, ordered assembly results when the solution state has a large population of a conformation with propensity for assembly, allowing it to adsorb, diffuse, and interact with other peptides to form a long range ordered structure. In the case of M2, thermal energy aids in the transition to this assembly prone conformation both in solution and at the surface. Amorphous assembly results when a more conformationally

disperse peptide adsorbs, retains the dispersity and simply aggregates upon interacting with other peptides.

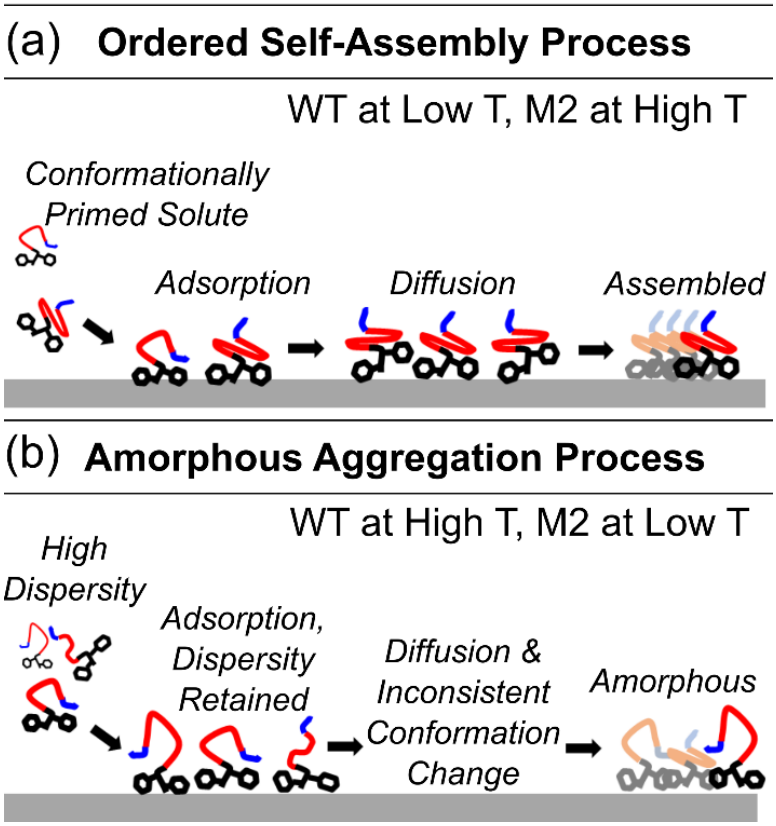

Figure 3.6. Proposed mechanism for thermally directed and conformationally mediated self-assembly of graphite-binding peptides. For simplicity, the scheme only shows the WT structure. The blue, red and black coloring represents the hydrophobic, hydrophilic, and aromatic domains of the peptide, respectively.

3.4 Concluding Remarks on the Thermal Selection of Peptides towards Assembly

In this complementary experimental and computational study of peptide conformational dynamics, adsorption kinetics and structural characterization of the assembled state, it is shown that the self-assembly of "soft" (conformationally flexible) biomolecules, can be directed by specific environmental conditions that affect the structural dispersity of the solvated molecules. Peptides with structurally uniform solution conformations, for example WT, readily self-organize into long-range ordered nanostructures, given the peptide conformation has a propensity to assemble. Increasing

the thermal energy elevates the dispersity of the peptide conformations in solution, which negatively impacts the adsorption and assembly process. Similar to the case of thermal destabilization, peptides that are already conformationally disperse at room-temperature, such as M2, do not readily assemble. Interestingly, increasing the supplied thermal energy allows peptides, such as M2, to sample the conformational space, and consolidate to a structure with increased propensity for self-assembly.

The profound effect of temperature on the adsorption kinetics and assembly behavior of these two solid-binding peptides suggests that SBPs are conformationally tunable, and thus, belong to the class of stimuli responsive materials that have use for a wide variety of practical applications, such as functional bioelectronic devices. From a general fundamental perspective these results expand the view of the effect of temperature on the molecular assembly process. For conformationally "soft" molecules, the temperature does not only affect the assembly kinetics, but also changes the aggregation structure due to the modification of solution conformational states.

Chapter 4:
Intermolecular Energetic Implications of Thermally Selected Conformations

4.1 Introduction

Structural dependencies are especially pivotal when assemblies rely on well-defined, directional interactions between the monomeric units as well as on specific interactions with the underlying solid substrate.[100,101] Given this structural dependence, further tuning of the equilibrium assembled states is achieved by external solution stimuli, such as temperature, pH, and salt concentration that modify or perturb the molecular conformation and intermolecular interactions dictating the assembly process.[88,102,103] Soft, flexible biomolecules, such as short peptides, are particularly sensitive to external solution conditions and can interchangeably assume different stable conformations.[87,104-106] This dynamic yet controllable nature of soft biomolecules have made them highly valuable for a variety of technological applications, such as sensors and molecular electronics.[105,107]

One such group of conformationally labile biomaterials with technological application are combinatorially selected solid-binding peptides (SBPs) that bind to their inorganic target and can form amorphous or long range ordered monolayers on two-dimensional surfaces.[20,31,108] As demonstrated in Chapter 3, in addition to the molecular sequence, the equilibrium self-assembled structure of a SBP was demonstrated to be tunable *via* environmental stimuli prior to adsorption, such as thermal pre-treatment, affecting the conformation of the aqueous peptide.[109] SBPs have thus become potential candidates for the directed assembly of two-dimensional devices with active interfaces

that possess tunable physical transport and chemical properties that are desired for bioelectronic devices.[25,110]

While the impact of external stimuli on the assembled structure of SBPs has been studied extensively, our understanding of the intermolecular interactions within the assembly and interfacial bonding interactions with the solid substrate has remained limited. Common methods to determine energetics of self-assembly, and intermolecular interactions within the assembly lack molecular resolution as they rely on visual, qualitative, classification of micrometer scale structural differences between ordered and amorphous regions.[31,108] The lack of quantitative molecule-level description of the energetics of the assemblies hampers the engineering of active interfaces with tailored transport properties, *i.e.,* heat, mass, or electronic, which are affected by the binding strength and mobility of the assembled molecules.[111-113] To illuminate the effects of the amino acid sequence and incubation temperature-controlled peptide conformation on the energetics of two-dimensionally assembled graphite binding peptides, we analyzed their thermally most active energetic states at the nanoscale by scanning probe methods and molecular dynamics simulations.

4.2 Experimental Methodology

4.2.1 Peptide Synthesis

The graphite binding peptides were synthesized on a preloaded support resin using HBTU activation chemistry and Fmoc deprotection as previously reported.[20-21] The peptides were purified by HPLC (Waters Deltaprep 600, Semiprep. Mode) using a linear gradient of 1% per minute at a flow rate of 10 mL/min. The synthesized peptide's

molecular weight was confirmed by MALDI-TOF mass spectrometry with reflectron (RETOF-MS) (Autoflex II, Bruker Daltonics, Billerica, MA).

4.2.2 Sample Preparation for Peptide Self Assembly and AFM Imaging

Highly oriented pyrolytic graphite (HOPG Grade 1, SPI, Inc.) sample surfaces with an approximate area of 0.25 cm^2 were mechanically cleaved using scotch tape. After cleavage, 40 µL of peptide in DI water of varying concentrations were incubated on the graphite surface for 3 hours to reach an assumed equilibrium. Samples of GrBP5-WT, GrBP5-M2, GrBP5-M4, and SS-GrBP5 as shown in Figure 4.1a were prepared using 1 µM peptide solutions. In addition, 2.5 µM peptide solutions of GrBP5-WT and GrBP5-M2 were used for investigating effects of temperature induced conformational changes as shown in Figure 4.3a. The peptide solution was pre-heated for 30 minutes at the incubation temperature as this was shown to thermally bias the conformational states of the peptide in solution.[24] After pre-heating, 40 µL of pre-heated peptide solution was incubated on a fresh graphite surface at the same temperature for 3 hours. Non-equilibrium peptide assemblies of GrBP5-WT and GrBP5-M2 were prepared by stopping the incubation before the peptide had enough time to form long-range ordered assembled structures. This was accomplished by incubating 1 µM peptide solutions for 30-minutes at 296 K for GrBP5-WT and 320 K for GrBP5-M2. Peptide solutions were wicked from the incubated HOPG surfaces and subsequently dried under a gentle nitrogen flow for 30 seconds. Dried peptide samples were visualized under ambient conditions using a DI Nanoscope IIIa SPM (Digital Instruments) in tapping mode using soft tapping mode AFM probes (HQ:NSC14/No Al, MikroMasch) before IFA analysis to confirm and ensure consistency in the self-assembled structure.

4.2.3 AFM Image Analysis

AFM images were analyzed using the Gwyddion SPM data analysis software.[32] The percent of ordering was deduced from the fraction of the total surface coverage that is part of a long range assembled structure. Total surface coverage was determined by first flattening the image and then masking based on height to separate the peptide from the graphite surface. The ordered regions were subsequently determined by thresholding the initial mask based on either the area or aspect ratio of individual peptide domains. Manual editing of the mask was needed for samples of densely packed peptide to distinguish between ordered and amorphous regions. At least three 1 μm^2 AFM images were analyzed for each sample and averages and standard deviations were determined from all individual image measurements.

4.2.4 Microscopic Energetic Analysis

Our microscopic energetic analysis employs a nanoscale mechanical scattering technique originally dubbed Intrinsic Fiction Analysis (IFA), as it is based on lateral force AFM, described in detail previously.[29, 33] Briefly, IFA relies on the coupling of the sliding AFM probe with fluctuating molecular modes in or at the interfaces of the sample material. Examples of fluctuation modes are sidechain or backbone rotations, bonding-debonding interactions, and probe-sample free surface dispersion interactions.[29, 34-36] In the work here, the prominent fluctuation mode that is coupling with the AFM probe is the adhesive bonding mode of the polypeptide with the HOPG substrate.

Force spectra (friction-velocity isotherms) are obtained by varying scanning velocities at constant temperature. Spectra obtained at different temperature are then treated based on the theory of time-temperature equivalence and superimposed by

shifting them either horizontally for fluctuation energy determination, or vertically for entropic cooperativity measurements.[35] In this study we focused on the fluctuation energetic analysis. Shift factors, a_T, obtained from horizontal shifting of the force spectra were plotted against the inverse recording temperature according to the well-established Arrhenius method. Activation energies were averaged over multiple repeated IFA experiments, and the standard deviation was taken as the error inherent in the Arrhenius curve propagated across all measurements.

IFA measurements of the dried peptide samples were obtained using a contact mode stand-alone Explorer SPM (Topometrix) in a low humidity nitrogen atmosphere. The sample temperature was controlled using a MMR heating stage.[33] Lateral forces were determined from the lateral deflection of the AFM tips using a blind calibration method in which the friction coefficient of a cleaned silicon wafer is obtained and scaled to the known friction coefficient to determine a geometric calibration factor.[37] The silicon wafer was cleaned by sonicating in acetone and then in methanol for 10 and 40 minutes respectively. The cleaned silicon wafer is rinsed with deionized water and dried in a vacuum oven at 110°C under a nitrogen atmosphere for 2 hours to create a natural oxide layer.

4.2.5 Molecular Dynamics of Peptide Adsorption

Pep-Fold 3 was employed to generate the solution structure used in molecular dynamics simulations.[38-39] Two-hundred iterations were performed and grouped by the sOPEP energy value. The lowest energy structure was used for adsorption studies in Maestro-Desmond (Schrödinger Release 2019-2: Desmond Molecular Dynamics System, D. E. Shaw Research, New York, NY, 2019. Maestro-Desmond Interoperability Tools, Schrödinger, New York, NY, 2019).[40] A graphene sheet was constructed to be

40 × 37 Å using the built-in Nanostructures generator. The peptide structure was oriented 9 Å above the graphene surface, the cut-off for long-range interactions. The graphene was infinitely bonded, and the simulation box had a buffer region of 1×1×15 Å. The TIP3P water model was used with the OPLS3e force field.[41-42] Before running the simulating, the peptide-graphene system was relaxed by performing 100 ps of Brownian dynamics followed by 2000 iterations of steepest descent minimization. Molecular dynamics simulations were 10 ns in length using the NVT (constant number-volume-temperature) thermodynamic ensemble at a temperature of 298 K, with a Langevin thermostat, and time step of 2 fs. Simulations were then subsequently analyzed with UCSF Chimera using the built-in ensemble clustering algorithm to determine the most frequent adsorbed peptide conformation.[43] Distances between the graphene surface and the apparent contacts were measured. Amino acid residues were considered in contact if the distance was less than or equal to 3.8 Å, the equilibrium van der Waals radius.

4.3 Results and Discussion

4.3.1 Amino acid sequence and peptide-graphite interaction

First, we investigated the effect of sequence and chemistry in polypeptides on the self-assembled structure and binding energy with HOPG, involving the wild-type graphite binding peptide, GrBP5-WT, and three rational mutants of it, *i.e.*, GrBP5-M2, GrBP5-M4, and SS-GrBP5. The sequence and relevant properties of these peptides are provided in Figure 4.1a. GrBP5-WT was chosen as the champion of all graphite binding-peptides from a combinatorial mutagenesis study involving millions of polypeptides.[31] GrBP5-WT forms a stable long-range structured assembly on graphite surfaces at room-temperature with an incubation time of 3 hours and concentration of 1 μM in deionized water, as

specified in the experimental section. GrBP5-M2 has increased aromatic content, GrBP5-M4 is a completely hydrophilic peptide, SS-GrBP5 retains this amphiphilicity of GrBP5-WT and GrBP5-M2 while increasing the overall hydrophilicity relative to GrBP5-WT. The self-assembled structures of the mentioned peptides are shown in Figure 4.1b. While GrBP5-WT and SS-GrBP5 both form long range ordered structures with six-fold symmetry, GrBP5-M2 and GrBP5-M4 form amorphous monolayers, as previously reported in the literature.[20, 25] All self-assembled peptide structures have thicknesses around 1.5-2 nm, suggesting monolayers with high surface coverage (> 80%).

(a)

Name	Sequence	MW	GRAVY	pI
GrBP5-WT	IMVTESSDYSSY	1381.5	-.242	3.55
GrBP5-M2	IMVTESSDWSSW	1427.5	-.175	3.55
GrBP5-M4	TQSTESSDYSSY	1354.3	-1.54	3.55
SS-GrBP5	SSIMVTESSDYSSY	1555.6	-.321	3.55

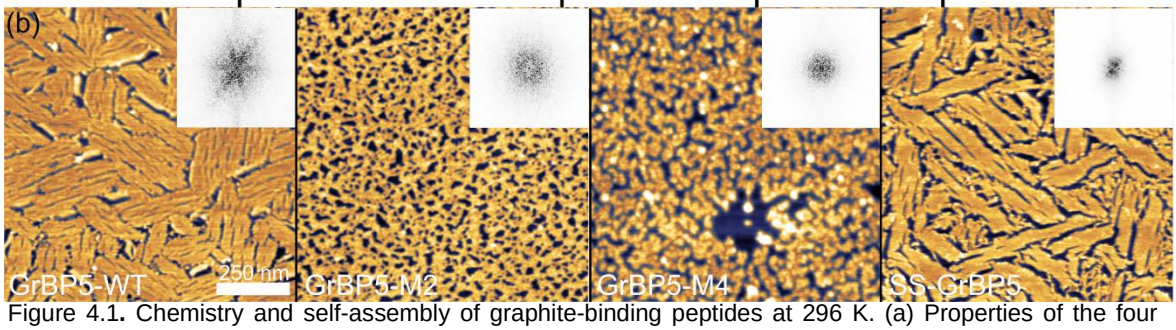

Figure 4.1. Chemistry and self-assembly of graphite-binding peptides at 296 K. (a) Properties of the four graphite binding peptides including the molecular weight (MW) in Daltons, the grand-average hydropathy (GRAVY), and isoelectric point (pI). (b) Atomic force microscope images of the equilibrium self-assembled structures resulting from 1 µM peptide incubated for 3 hours on a graphite surface. Insets are the fast-Fourier transform of the AFM images. Color coding of the peptide sequence is as follows: green – hydrophobic, red – negatively charged, orange – hydrophilic, blue – aromatic.

IFA energetic data obtained from the four peptide samples (Figure 4.1b) are shown in Figure 4.2a. GrBP5-M2 reveals the strongest mode energy of E_{M2} = 35.5 ± 1.0 kcal/mol, stronger than the wild-type GrBP5-WT mode energy of E_{WT} = 31.8 ± 1.3 kcal/mol. GrBP5-WT and SS-GrBP5 (E_{SS} = 31.2 ± 0.6 kcal/mol) have similar IFA mode energies. GrBP5-M4, the completely hydrophilic mutant, has an IFA mode energy of approximately half of GrBP5-WT, E_{M4} = 14.9 ± 0.8 kcal/mol. The following discussion will show that the IFA energies are congruent with the molecular binding fluctuation energy between the peptides and HOPG.

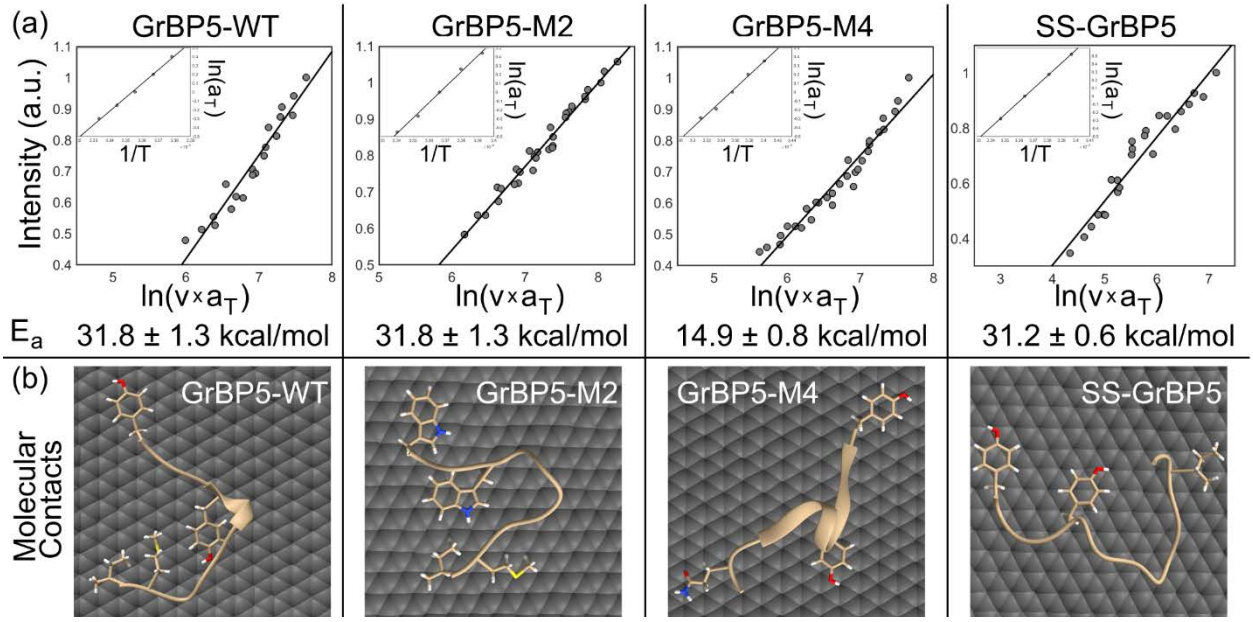

Figure 4.2. Energetic analysis of peptide-graphite binding energy at 296 K. (a) Shifted friction-velocity spectra from Intrinsic Friction Analysis (IFA) of graphite-binding peptides. The Arrhenius curve of the thermal shift factors is inset, and the resulting energy is displayed below. (b) The most frequently observed graphene adsorbed peptide from a molecular dynamics simulation. Only amino acids contacting the graphene surface are displayed for clarity. Oxygen is colored in red, sulfur in yellow, hydrogen in white, and nitrogen in blue.

Based on previous studies reporting the importance of aromatic residues in peptide adsorption to graphite, we anticipate that the tyrosine or tryptophan residues to be the primary anchoring groups with graphite.[31,94] In addition, we can expect that the binding energies will include all side-chain and main-chain contacts with the graphite surface. To further interrogate the peptide molecular contacts and match them to the observed

experimental IFA fluctuation energies, we performed molecular dynamics (MD) simulations of the peptide adsorption to a single sheet of graphene. The most frequently observed adsorbed peptide conformation during the 10 ns simulation is shown in Figure 4.2b. Only the sidechains contacting the graphene and main chain are shown for clarity.

As expected, the tyrosine (Tyr) or tryptophan (Trp) residues are in contact with graphene for all peptides. The interaction strength of Tyr and Trp with graphene were determined via DFT to be E_{Tyr} = 12-14 kcal/mol and E_{Trp} = 15-18 kcal/mol, respectively.[114,115] Moreover, as shown in Figure 4.2b, both GrBP5-WT and GrBP5-M2 have additional molecular contacts between isoleucine (Ile) and methionine (Met) with graphene. The interaction strengths of Ile-graphene and Met-graphene have both been estimated to be 5 to 8 kcal/mol depending on the computational force field.[116] Based on the computationally determined contacts and energetics we can assign the experimentally observed 4 kcal/mol difference between E_{WT} and E_{M2} to the amino acid mutation from Tyr to Trp, *i.e.*, $E_{M2} - E_{WT} \sim 2 \times (E_{Trp} - E_{Tyr})$. Additionally, both E_{WT} and E_{M2} are approximately 6-7 kcal/mol greater than what would be expected from aromatic interactions alone. We ascribe this additional energy to the hydrophobic contacts between the Ile and Met residues and the graphite surface, *i.e.,* $E_{WT/M2} = E_{Ile}/E_{Met} + 2 \times E_{Tyr/Trp}$. For GrBP5-WT and GrBP5-M2, neither of these hydrophobic residues made complete contact with the graphene surface suggesting why the experimentally observed binding energy is about half of the computationally suggested binding energy of both Ile and Met. For GrBP5-M4, the C-terminal Tyr was intermittently in contact with the graphene suggesting that it may not be in contact in the dried state explaining why $E_{M4} \sim E_{Tyr}$. In addition to the aromatic rings, the C^{γ} of the glutamine residue in GrBP5-M4 was also in contact. We do

not anticipate a single C-graphene interaction to be strong enough to be experimentally discernible. SS-GrBP5 contacts with graphene were analogous to those of GrBP5-WT, save the Met-graphene interaction, explaining the equivalence between E_{WT} and E_{SS}. Overall, the binding energy discussion let us conclude that the measured IFA fluctuation energies correspond to the molecular adhesive energies between the peptides and graphite, and that the amino acid sequence plays a prominent role in the interaction of the peptides with graphene.

4.3.2 Conformational partitioning of peptide-graphite interaction energy

While IFA and MD (Figure 4.2) energetic analyses established a strong correlation between the peptide amino-acid sequence and the substrate interaction energies, there is no apparent correlation between the strength of the binding energies (Figure 4.2a) and the assembled structures (Figure 4.1b) as previously postulated.[31] For instance, GrBP5-WT and GrBP5-M2 exhibit highly divergent self-assembled structures despite their similar binding energies. This is, on first sight, a surprising result. However, what is lacking in the prior discussion is information about the conformational states of the adsorbed peptides, which is an additional important parameter for molecular assembly. To this end, we further investigated the conformational dependence of peptide-graphite binding energies for GrBP5-WT and GrBP5-M2 as work presented in Chapter 3 showed they have thermally controllable self-assembled structures initiated by conformational changes of the peptides in solution. In the following, we analyzed the self-assembly structures and binding energies as a function of the incubation temperature for both GrBP5-WT and GrBP5-M2.

The AFM temperature series in Figure 4.3a illuminates the structural transition observed with increasing incubation temperature. GrBP5-WT exhibits an unstructured assembly at an elevated incubation temperature of 310 K that is contrasted to the highly ordered structure at a low temperature of 296 K. While GrBP5-M2 also shows a change in the order of the structure with temperature, Figure 4.3a, the behavior is opposite to that of GrBP5-WT. In parallel to the structural transition from long-range ordering to amorphous structuring, GrBP5-WT adsorption decreases with increasing temperature

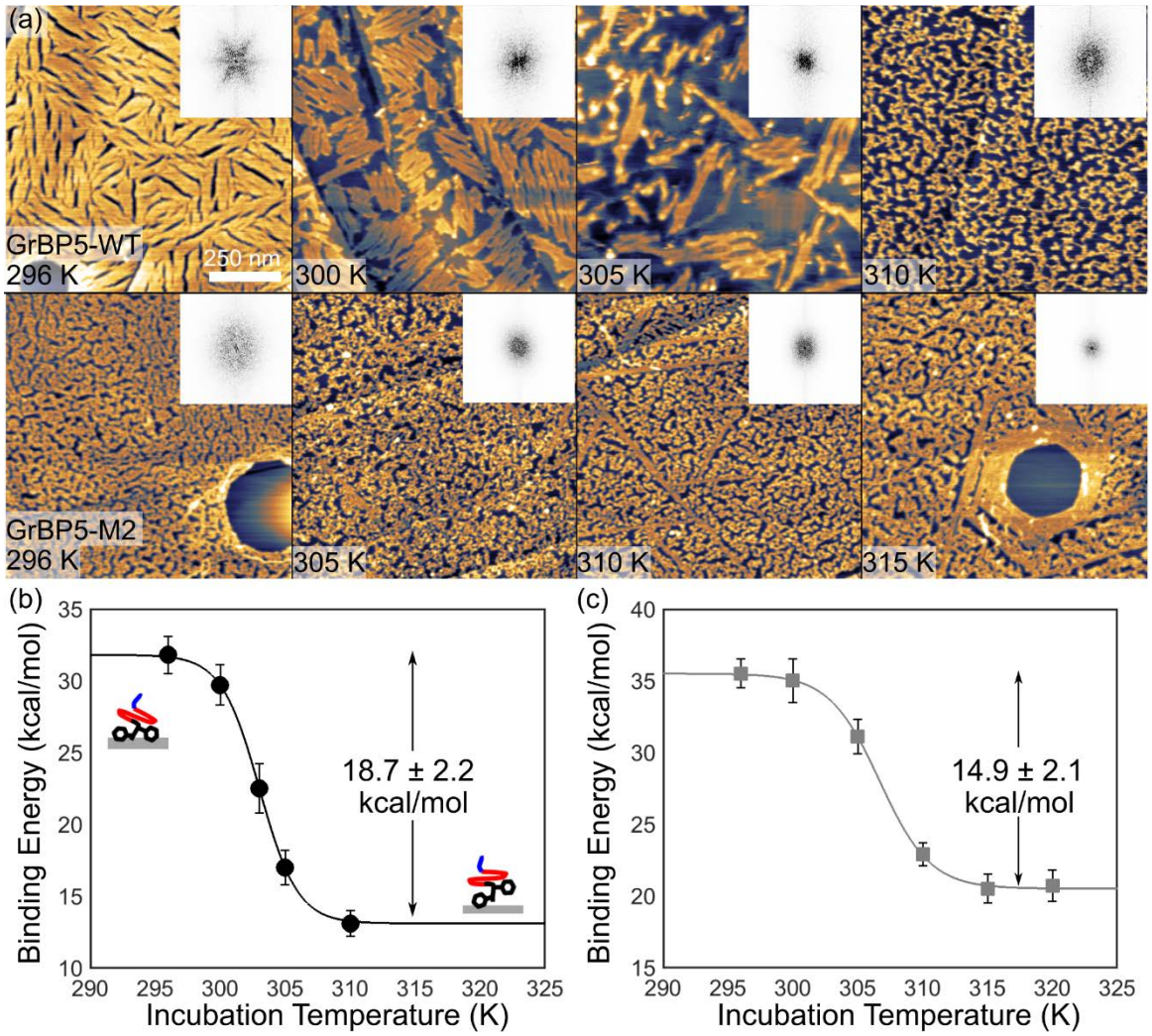

Figure 4.3. Thermal Partitioning of Peptide-Graphite Binding Energy. (a) Characteristic self-assembled structures resulting from 3-hour isothermal incubations of 2.5 μM GrBP5-WT (top row) at temperatures from 296 K to 310 K. The bottom row is the analogous images for GrBP5-M2 incubated at 296 K to 315 K. IFA determined binding energies of GrBP5-WT (b) and GrBP5-M2 (c) as a function of incubation temperature. The sigmoidal fit is described by Equation 1. The fit parameters are ΔT = 1.47 K and T_{50} = 303 K for GrBP5-WT and ΔT = 1.95 K and T_{50} = 307 K for GrBP5-M2.

going from an equilibrium surface coverage of nearly 100% at 296 K to 30% at 310 K. The percentage of the adsorbed GrBP5-WT found in ordered states, as determined by AFM image analysis (see experimental section), decreases from close to 100% and 296 K to ~0% at 310 K. On the other hand, GrBP5-M2 adsorption remains high from low to elevated temperatures and the percentage of ordered peptide structures increases from 0% at 296 K to ~40% at 320K.

IFA of the peptide assemblies, presented in Figure 4.3a, exhibited a sigmoidal relationship between peptide-graphite binding energy and incubation temperature for both GrBP5-WT and GrBP5-M2, Figure 4.3b and Figure 4.3c respectively. This result reveals that the thermally induced conformational change that leads to different assembled structures is associated with different peptide-graphite interactions. The energy difference between the two plateaus for GrBP5-WT and GrBP5-M2 are ΔE_{WT} = 18.7 ± 2.2 kcal/mol (31.8 ± 1.3 kcal/mol – 13.1 ± 0.9 kcal/mol) and ΔE_{M2} = 14.9 ± 2.1 kcal/mol (35.5 ± 1.0 kcal/mol – 20.7 ± 1.1 kcal/mol), respectively. We assign the thermally induced change in binding energy to the decoupling of an aromatic residue from the graphite surface. For GrBP5-WT, $E_{WT,\ 310\ K}$ is comparable to the theoretical binding of a single Tyr with graphite, and for GrBP5-M2, ΔE_{M2} is approximately the theoretical binding energy of a Trp to graphite. ΔE_{WT} is approximately 5-7 kcal/mol larger than the theoretical binding energy of Tyr suggesting that at 310 K the hydrophobic molecular contacts (present for GrBP5-WT at room temperature) are lost in addition to the aromatic Tyr contact. In effect, GrBP5-WT at 310 K binds with a similar strength to the graphite surface as GrBP5-M4. The closeness in binding energy of GrBP5-WT at 310 K and GrBP5-M4 at 296 K in conjunction with their associated amorphous equilibrium

assembled structure, Figure 4.3a and 4.3b, respectively, suggests that GrBP5-WT adopts a conformation similar to that of GrBP5-M4 in response to increasing temperature. This result highlights the molecular insight that can be obtained from the molecular energetic analysis of the peptide-graphite interface, yielding crucial information about the peptide conformational changes in solution.

Given the link between binding energies and the conformation of peptides in solution, we analyzed the conformational transitions for GrBP5-WT and GrBP5-M2 from binding energy – incubation temperature plots, Figure 4.3b and 4.3c, employing sigmoidal fits with two fit parameters, ΔT and T_{50},

$$E = E_{Low\,T} - \frac{E_{Low\,T} - E_{High\,T}}{1 + \exp\left(\frac{T_{50} - T[K]}{\Delta T}\right)} \quad Equation\ 4.1$$

The fitting parameter ΔT represents a critical temperature step related to the energy required for the transition. T_{50} represents the temperature at which the binding energy is halfway between the upper and lower bounds. In terms of the peptide conformation, equimolar amounts of peptide are in the two conformational states at $T = T_{50}$. For GrBP5-WT, the best fit yields ΔT = 1.47 K and T_{50} = 303 K. For GrBP5-M2, the best fit is for ΔT = 1.95 K and T_{50} = 307 K. The range of values obtained for ΔT and T_{50} based on the steepest and shallowest sigmoidal fits were 0.4 K and 0.1 K, respectively, for GrBP5-WT, and 0.3 K and 0.3 K, respectively, for GrBP5-M2. The larger ΔT for GrBP5-M2 suggests that the transition to the high temperature peptide conformation requires more thermal energy than the corresponding transition in GrBP5-WT. Equation 4.1 represents the temperature dependent partitioning of the binding energy with graphite as dictated by the conformational change in the peptide. Thus, with incubation temperature as a control

parameter, not only can the assembled structure of the peptide be dictated but also the molecular coupling strength with the substrate, in this case graphite. The molecular coupling strength is a critical parameter for bioelectronic devices that rely on bioactive interfaces.

Since Equation 4.1 represents the partitioning of peptide conformational states, further interrogation allows for determination of the energetic differences between the low and high temperature conformations. From the conformational transition described by Equation 4.1, the probability of the high temperature conformation can be defined as,

$$P_{High\,T} \equiv \left(\frac{E_{Low\,T} - E}{E_{Low\,T} - E_{High\,T}}\right) = \frac{1}{1 + \exp\left(\frac{T_{50} - T[K]}{\Delta T}\right)} \quad Equation\ 4.2$$

Using the relationship between probability and energetics, one can determine the relationship between the sigmoidal fit factors, T_{50} and ΔT, and the free energy difference, $\Delta G = G_{High\,T} - G_{Low\,T}$, between the low and high temperature states:

$$\frac{1}{1 + \exp\left(\frac{T_{50} - T[K]}{\Delta T}\right)} = \frac{1}{1 + \exp\left(\frac{\Delta G}{RT}\right)} \quad Equation\ 4.3$$

where, T is the absolute temperature in Kelvin, and R is the universal gas constant. Equation 4.3 yields that the sigmoidal dynamics is linear regarding the inverse-temperature with slope $\Delta G/R$. The linearity is confirmed, Figure 4.4, for both peptides. The free energy difference for GrBP5-WT is ΔG_{WT} = 125 ± 4 kcal/mol, while for GrBP5-M2 it is ΔG_{M2} = 98 ± 2 kcal/mol. It should be noted here that the larger energy difference for GrBP5-WT implies that GrBP5-WT is more conformationally stable than GrBP5-M2 at room-temperature.

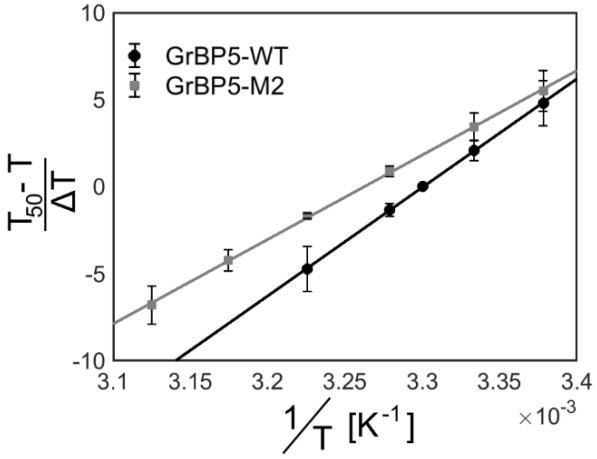

Figure 4.4 Linear relationship between the sigmoidal fit parameters of Equation 1 and the inverse temperature as described by Equation 4.3. Error bars were propagated from the ranges of T_{50} and ΔT.

While Equation 4.2 provides an insightful relationship between the incubation temperature and the extent of the peptide's conformational change, the relationship between the micrometer scale assembled structure and peptide conformation remains still open. To develop this relationship, the concentration of the assembly active peptide conformations (APC) of GrBP5-WT and GrBP5-M2 is required. From Equation 4.2, the effective concentration of the high temperature peptide conformation can be defined as,

$$C_{eff} \equiv C_o P_{High\,T} = \frac{C_o}{1 + \exp\left(\frac{T_{50} - T[K]}{\Delta T}\right)} \quad Equation\ 4.4$$

where C_o is the peptide solution concentration. Since GrBP5-WT assembles at low temperature and GrBP5-M2 assembles at high temperatures, it follows that Equation 4.5a describes the concentration of the assembly-active GrBP5-M2, while Equation 2-5b describes the concentration of assembly-active GrBP5-WT.

$$C_{APC,M2} = C_{eff,M2} = \frac{C_o}{1 + \exp\left(\frac{T_{50,M2} - T[K]}{\Delta T_{M2}}\right)} \quad Equation\ 4.5a$$

$$C_{APC,WT} = C_o - C_{eff,WT} = C_o - \frac{C_o}{1 + \exp\left(\frac{T_{50,WT} - T[K]}{\Delta T_{WT}}\right)} \quad Equation\ 4.5b$$

Plotting the effective concentration, as determined from Equations 4.5a and 4.5b for the experimental temperatures tested *versus* the associated degree of ordering, ζ, from AFM images (Figure 4.3a) yields a sigmoidal relationship for GrBP5-WT and a partial sigmoidal relationship for GrBP5-M2, as shown in Figure 4.5a and 4.5b, respectively.

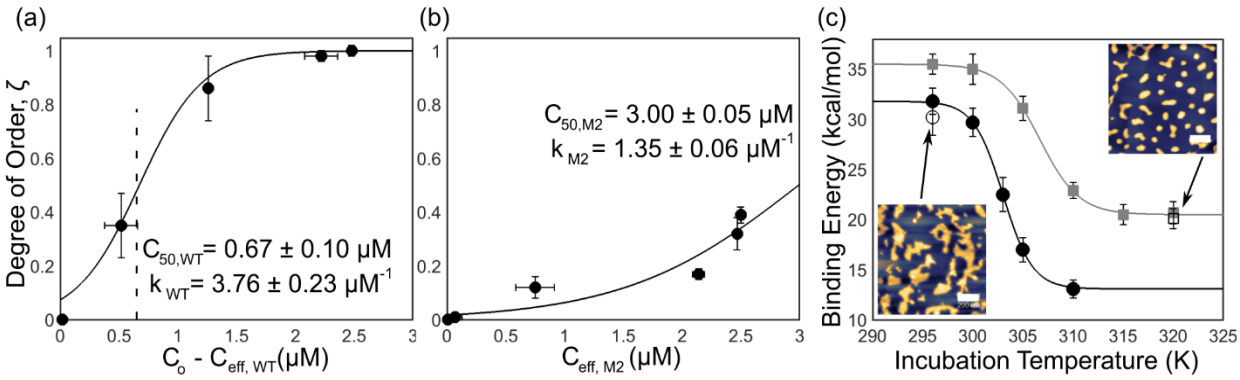

Figure 4.5 Sigmoidal relationship between micron scale assembly and assembly-active peptide conformation concentration for GrBP5-WT (a) and GrBP5-M2 (b). The solid black line is the sigmoidal fit with functionally described by Equation 6 using the fit parameters inset. (c) IFA binding energy of non-equilibrium amorphous assemblies of GrBP5-WT (open circle) and GrBP5-M2 (open square). Assemblies were obtained from 1 μM peptide incubated for 30 minutes on the graphite surface. AFM images of the assembled structure are inset. The scale bars for both images represent 200 nm.

Since only the APC forms the observed long-range ordered structures, a sigmoidal relationship of C_{APC} with ζ is expected. The appropriate fit function (Equation 4.6) with its two fit parameters, C_{50} and k, describes the change in the assembly's long-range order as a function of the APC concentration, Figure 4.5a and 4.5b, providing the desired conformation-assembly structure relationship. C_{50} is the concentration required for a 50% long-range ordered assembled structure, and k describes how significantly changes in

C_{APC} impacts ζ. Hence, k can be seen as an indirect measure of the rate of assembly in units of inverse concentration.

$$\zeta = \frac{1}{1 + \exp(k \times [C_{50} - C_{APC}])} \quad Equation\ 4.6$$

The data fits in Figure 4.5a and Figure 4.5b, yield the following fit parameters for GrBP5-WT and GrBP5-M2, respectively: $C_{50,\,WT}$ = 0.67 µM and $C_{50,\,M2}$ = 3.00 µM, and, k_{WT} = 3.76 μM^{-1} and k_{M2} = 1.35 μM^{-1}. While k qualitatively gauges the rate of assembly, C_{50} is dictated by the energetics of assembly, *i.e.*, a more favorable assembly process results in a smaller C_{50}. The large C_{50} value for GrBP5-M2 as compared to the one for GrBP5-WT is congruent to work reported in Chapter 3 in which only 5 µM assemblies at 320 K yielded $\zeta \sim 0.8 – 1$. If we assume an average temperature of 303 K for GrBP5-WT and 308 K for GrBP5-M2, we may estimate the free energy of assembly based on these C_{50} values. For GrBP5-WT the free energy of assembly is approximately -8.6 ± 1.3 kcal/mol, while the free energy of assembly for GrBP5-M2 is -7.8 ± 0.1 kcal/mol. The magnitude of this free energy is on the order of a few intermolecular hydrogen bonds. The reported $C_{50,\,M2}$ is imprecise in comparison to $C_{50,\,WT}$ since we are extrapolating as opposed to interpolating, thus, the estimated free energy of assembly is a very rough estimate for GrBP5-M2. Nonetheless, the estimates show that GrBP5-WT assembly is more energetically favorable than GrBP5-M2 assembly as expected.

The analysis discussed has been made under the assumption that the peptide conformation is set in the liquid phase in close vicinity to the substrate, and, unaltered during the assembly process. To validate this assumption, we let the thermally incubated peptides only assemble for 30 minutes instead of 3 hours. Within the shortened timescale,

the assembly process is interrupted and yields amorphous non-equilibrium structures, as demonstrated by the inset AFM images in Figure 4.5c. If our assumption above is correct, we would expect the binding energy of peptides with the graphite substrate to be independent of the incubation time and assembled structure. Thus, we picked the two most extreme incubation temperature conditions for GrBP5-WT and GrBP5-M2 of 296 K and 320 K, respectively, for which 3-hour assemblies showed long-range ordering, Figure 4.3a. As expected, the non-equilibrium assembled structures were in both cases amorphous, and showed energetic values of E_{WT}^{*} = 30.2 ± 1.8 kcal/mol and E_{M2}^{*} = 20.1 ± 1.0 kcal/mol for GrBP5-WT and GrBP5-M2, respectively, closely resembling the values for 3 hours, as illustrated in Figure 4.5c. This result suggests that during the assembly process, the peptide is part of a conformational ensemble that is stable, *i.e.*, locked in its conformational state, and maintains consistent contacts with the graphite surface, and thus, substantiating our assumption. Additionally, this result suggests that differences in peptide-substrate energetics are completely missed by microscale structural characterizations.

4.3.3 Rationally designed assembly and peptide-graphite coupling

Based on the energetic analysis above, it was shown that with the appropriate temperature stimuli and process time, the binding energy and the assembled structure can be tailored for peptide adsorption on free surfaces. The interpretation on the energy values above relied on simple energetic accounting of computationally derived amino acid-graphite interactions. To further validate the presented interpretation, but also to show the predictive capabilities, we chemically modified the GrBP5-M2 peptide to show long-range assembly at 296 K. As molecular analysis of ΔE_{M2} presented in Figure 4.3c

suggested that a decoupling of Trp from the graphite allowed GrBP5-M2 to form long-range ordered assemblies at 320 K, we predicted that a truncated version of GrBP5-M2, *i.e.*, IMVTESSDWS, could potentially form long-range ordered assemblies at 296 K with a binding energy of ~20 kcal/mol. As anticipated, and shown in Figure 4.6a, the truncated-M2 forms long-range ordered assemblies on graphite surfaces with six-fold symmetry after incubation of 1 μM peptide for 3 hours at 296 K. The average height and width of the truncated-M2 nanostructure was 1.1 ± 0.1 nm and 120 ± 60 nm, respectively. These structural results diverge slightly from GrBP5-M2 assemblies as they are slightly shorter and wider. Further investigation of the truncated-M2 assembly process is needed to explain these structural differences. IFA of the truncated-M2 assembly, Figure 4.6b, yields a binding energy of $E_{Trunc\text{-}M2}$ = 19.7 ± 1.2 kcal/mol. This energy is within error of the binding energy predicted based on the high-temperature assembled GrBP5-M2, Figure 4.3c. Molecular contacts between truncated-M2 and graphene were determined to be Met, Trp, Val, and Ile *via* adsorption simulations, Figure 4.6c. These contacts are congruent with the analysis of data presented in Figure 4.2, *i.e.,* that Met, Ile, and Trp dictate the binding energy of high temperature GrBP5-M2. These results validate our interpretation of the IFA data and showcase its ability to predict self-assembled structures and binding energies.

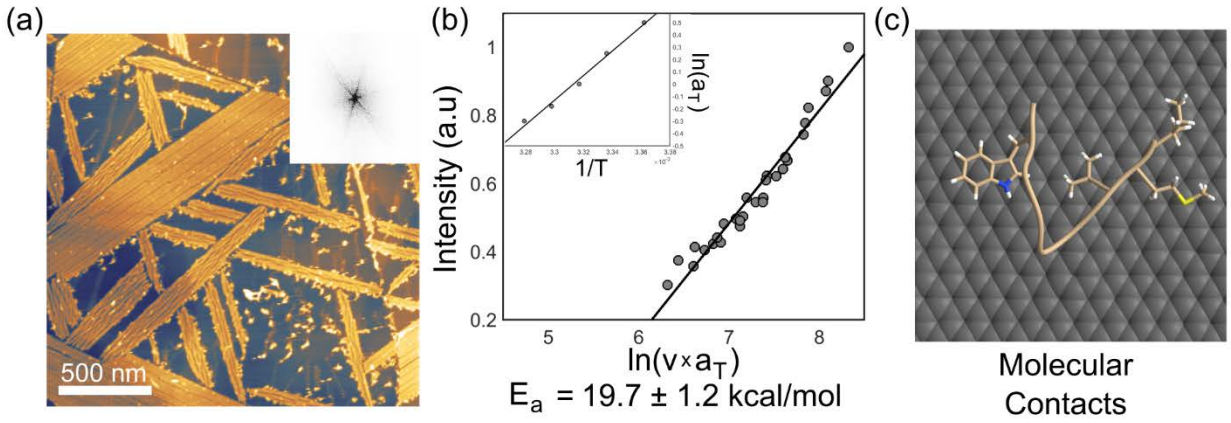

Figure 4.6 Self-assembly and binding energy of Truncated M2 at 296 K. (a) AFM images of self-assembled truncated M2 showing 6-fold symmetry. Inset: Fast-Fourier transform (FFT) of the AFM image. (b) IFA of truncated-M2 assembly shown in (a) revealing an activation energy within error to that of high-temperature M2 assemblies. Inset is Arrhenius curve of thermal shift factors versus inverse temperature. (c) The most frequently observed graphene adsorbed peptide from a molecular dynamics simulation. Only amino acids contacting the graphene surface are displayed for clarity. Sulfur is colored in yellow, hydrogen is in white, and nitrogen is in blue.

4.4 Concluding Remarks on Conformationally Dependent Interfacial Energetics and Assembly

In summary, the peptide binding energies with HOPG at room temperature, involving a wild-type graphite binding peptide, GrBP5-WT, and three rational mutants (e.g., GrBP5-M2 and SS-GrBP5) were mainly attributed to surface interactions with aromatic residues of the peptides. While there were no correlations found between the magnitude of the interaction strength and the structure of the assembly (amorphous vs long-range ordered), the amino acid sequence was found to play a prominent role in the interaction. In addition, the effect of temperature, in particular the temperature pretreatment of the peptide solution, was found to be an extraordinary parameter to control the assembled structure, not because of thermal effects on surface kinetics and diffusion, but because of the environmental selection of specific peptide conformational states in solution, confirming previously reported work.[109]

As per the nanoscale probing of the molecular structure and energetics of peptide assemblies on graphite, thermally selected conformational variations of aqueous peptide were found to translate into a partitioning of binding energies. This was illustrated by studying the binding energy as a function of the incubation temperature that sets the probability for each conformational state. Our results show that any primary peptide conformational state in the liquid phase can prevail during the adsorption process, if thermally selected prior to the adsorption. This was illustrated for a binary set of peptides (GrBP5-WT and GrBP5-M2), each possessing two primary conformational states. Tuning the incubation temperature resulted in sigmoidal transitions between high and low binding energy states that could be assigned to the dominant conformational states in solution. We found that the more favorable state*, i.e.,* the high binding energy state, resulted in a long-range ordered assembled structure for GrBP5-WT, and, an amorphous structure for GrBP5-M2. The second, less favorable liquid conformational state of each of the two peptides, yielded low binding energy and resulted in the opposite assembled structures, *i.e.*, amorphous structures for GrBP5-WT and long-range ordered structures for GrBP5-M2. Phase segregated amorphous and long-range ordered structures were found for intermediate incubation temperatures, where both primary conformational states are present during assembly. The observed binding energy differences between the two states was ascribed to a change in the number of aromatic groups anchoring with graphite for both GrBP5-WT and GrBP5-M2. The more favorable states provided for GrBP5-WT and GrBP5-M2 twice the anchoring groups of tyrosine and tryptophan, respectively, to bind with graphite, than the less favorable state.

This study highlights (i) the importance of the molecular conformational state of the peptides in solution, as they dictate the availability of anchoring groups to substrates for weak non-specific interactions, and (ii) the tunability of the conformational state of short peptides with a simple external parameter, such as the temperature. Furthermore, the energetic results also reveal that long-range order in assemblies is independent on the magnitude of the binding energy. The degree of order in molecular assemblies depends on the specific conformation of the peptide in solution and the time of assembly, as the initial peptide conformation persists during the assembly process. Based on an effective concentration analysis of the assembly active peptide conformation, it was shown that the magnitude of the free energy difference between the amorphous and ordered states of GrBP5-WT is larger than for GrBP5-M2, and thus, provides a greater driving force towards order. Furthermore, by considering the self-assembly implications of thermally selected GrBP5-M2 conformations, a modified peptide was designed to assemble with predictable binding strength and structural order. The outcome was as expected, and, validated our interpretation of external thermal tuning of peptide solutions towards controlled assembly and binding energetics.

The results of the study presented herein on the coupling of peptides with a solid has fundamental and practical implications for the design of soft interfaces. Firstly, the nanoscale energetic analysis of molecular binding provides a quantitative description of both the aqueous peptide phase and intermolecular forces at the surface that can facilitate the development of molecule models of soft bio-inorganic interfaces. Additionally, the presented results on conformational selection and directed assembly enables a more complete understanding of the sequence-structure-function correlations

of soft interfaces. This fundamental understanding is the starting point for the functional design of soft bio-inorganic interfaces with tailored properties to seamlessly couple biology with solid-state bioelectronic devices, for example, biomolecular fuel cells, diagnostics, and field-effect transistors.[25]

Chapter 5:
Impacts of Molecular Conformation & Self-Assembled Structure on Interfacial Electronic Transport

In the previous two chapters (Chapters 3 and 4), the impact of thermal pre-treatment on graphite-binding peptide adsorption and self-assembly was investigated showing the impact that peptide conformation has on the propensity to form long-range ordered structures. In this chapter the analysis is extended to interrogate how molecular parameters and self-assembly may affect the electronic properties of the peptide-inorganic interface through the implementation of scanning tunneling microscopy.

5.1 Introduction

Bioelectronic devices in which biological systems are in intimate contact with man-made electronic material have become a promising avenue for disease diagnostics, therapeutics, bioreactors, as well as fundamental interrogations of cellular and neuronal systems.[117-119] A wide variety of materials have been explored for their use in such bioelectronic applications, e.g., semiconducting polymers and inorganic nanomaterials. The material type is often chosen for certain desirable properties, e.g., high electronic or ionic conductivity, flexibility, biocompatibility, *etc*.[18,120] While the choice of substrate material is important, a critical parameter space controlling the device functionality is the material linkers with which the system bridges the interface between the biological environment and device substrate.

For inorganic materials, polymeric or other chemical functionalizations are often used to bridge this nano-bio divide and display functional biological epitopes for improved

interfacial bio-inertness, cell adhesion and proliferation.[10,14,121] One class of inorganic nanomaterials of increasing interest for bioelectronic applications is single layer atomic materials such as graphene and two-dimensional (2D) transition metal dichalcogenides.[9-11,117] The electronic transport within these 2D nanomaterials is extremely responsive to adsorbed molecules, thus enabling extremely sensitive bioelectronic devices.[18,27] However, preserving this sensitivity prevents the application of many covalent linkages as they would impart point defects into the material and impede device functionality. To avert such electronic defects, engineers implement non-covalent functionalizations that rely on soft intermolecular interactions between adsorbed molecules and the 2D nanomaterial surface.[19,122] However, control over such weak interactions is typically limited and restricts the optimization of the nanoscale interfacial structure and resulting device performance.

In recent years, control over the nanoscale structure of linker molecules at inorganic material interfaces has been advanced by rationally engineered self-assembling biomolecules.[31,83,123] As presented in this work and previous work, solid-binding peptides are ideal tools for the molecular engineering of bio-inorganic interfaces for biomedical applications.[20,21,31-33,95] Fine-tuned control over the equilibrium self-assembly structure and intermolecular energetics acting at the bio-nano interface has been achieved through proper selection of the polypeptide amino-acid sequence, environmental conditions (temperature, pH, ionicity, etc.) and assembly parameters (concentration, incubation time, binary mixtures, etc.) as demonstrated in Chapters 3 and 4.[124-127]

Perhaps more critical for the development of bio-nano interfaces with bioelectronic applications, is understanding how the adsorbed peptide molecules and their self-assembled structure effects device relevant properties. Prior work in by Hayamizu *et al.* found that peptide adsorption and long-range ordered structuring at graphene field effect transistor interfaces n-type doped the device while maintaining high charge mobility.[25] Additionally, Akdim *et al*. linked the coupling between peptide's aromatic residues with the graphene to explain experimentally observed p-type and n-type doping of their devices.[128] While these important early studies elucidated electron transport phenomena within the hybrid bio-nano devices, the electronic transport across the bio-nano interface is equally crucial for designing bioelectronic systems.

Electronic transport across the peptide-inorganic interface results from the collective impacts of peptide sequence, conformation, and peptide-substrate interactions.[105,129-131] For instance, aromatic tryptophan residues have been shown to "dope" simple peptide, e.g., polyalanine self-assembled monolayers, while distinct electron transport properties were demonstrated for peptides with canonical secondary structure, e.g., beta sheet, alpha helix, and 3/10 helix.[132] Solid binding peptides, due to their short length and breadth of sequence space, are typically conformationally labile and without canonical secondary structure. Additionally, since solid-binding peptides rely on non-covalent interactions, in contrast to the oft-studied thiol-based monolayers, the pathway for electron transport is ill-defined. While the extraordinary complexity of solid binding peptide promises to allow for fine tuning of bio-nano interfacial properties, this complexity simultaneously hinders the system's rational design and engineering. As a first step towards rational design, we investigated the impacts of sequence, peptide

conformation, and peptide-graphite coupling on the electron tunneling across peptide-graphite interfaces produced from a set of self-assembled solid-binding polypeptides *via* a combination of scanning probe microscopies and metadynamics simulations.

5.2 Experimental Methodology

5.2.1 Peptide Synthesis

Graphite binding peptides were synthesized in-house (C2336X, CSBio Inc., Menlo Park, CA) on a preloaded support resin using HBTU activation chemistry and Fmoc deprotection as previously reported. The peptides were purified by HPLC (Waters Deltaprep 600, Semi-preparation Mode) using a linear gradient of 1% per minute of water to acetonitrile and a flow rate of 10 mL/min. Purity of the synthesized peptide was confirmed by MALDI-TOF mass spectrometry (Autoflex II, Bruker Daltonics, Billerica, MA).

5.2.2 Peptide Self-Assembly

All peptide self-assemblies were prepared by incubating 40 µL of peptide solution on to freshly cleaved highly oriented pyrolytic graphite with an approximate area of 0.25 cm^2 for 3 hours in a humid environment to prevent droplet evaporation. After incubation, peptide solution is wicked from the graphite surface using a laboratory tissue and the surface is blown dry with a gentle stream of nitrogen for at least 30 seconds. For high temperature assemblies, peptide solutions and cleaved graphite surfaces were both pre-heated to the desired temperature, 37 °C and 47 °C for WT-GrBP5 and M2-GrBP5, respectively, for 30 minutes prior to incubating for 3 hours at the elevated temperature. Room-temperature samples were incubated at ambient conditions of 22 °C. WT-GrBP5 samples were prepared using 2.5 µM concentrations, while M2-GrBP5 assemblies were

prepared using 2.5 μM and 5 μM concentrations for the room-temperature and high temperature assemblies, respectively. The higher concentration was used for M2-GrBP5 high-temperature samples to ensure significant degrees of long-range ordering as previously demonstrated.

5.2.3 Scanning Force Microscopy and Image Analysis

Dried peptide samples were visualized under ambient conditions using a DI Nanoscope IIIa SPM (Digital Instruments) in tapping mode using soft tapping mode SPM probes (HQ:NSC14, MikroMasch). Several 1 μm x 1 μm scans were obtained for each sample for further analysis. The average and standard deviations were determined from all sample images. SFM images were analyzed using Gwyddion SPM data analysis software.[47] Images were plane flattened and scan lines were aligned using built in Gwyddion functionality. Total surface coverage was determined by masking images based on height to separate the graphite surface from the peptide structures. The percent ordering was deduced from the fraction of peptide coverage that is part of a long-range ordered structure. To determine this fraction, the mask was manually edited to distinguish between ordered and amorphous regions. The amorphous regions were then subsequently filtered out by thresholding the initial mask based on either the area or aspect ratio of the individual peptide domains.

5.2.4 Scanning Tunneling Microscopy and Spectroscopy

Scanning tunneling microscopy (STM) images and spectra were obtained using a DI Nanoscope IIIa SPM (Digital Instruments) in ambient conditions. Peptide assemblies on graphite were electrically connected using colloidal silver paste. The STM tip was prepared from Pt/Ir wire cut under ambient conditions. All images were acquired in a

constant-current mode. Typical imaging conditions are bias voltages of (0.2 to 2 V and a tunneling current of 1 pA to 1 nA. Images were manipulated with the Scanning Probe Image Processor (SPIP) software. The relative tunneling spectroscopy was determined from I-V measurements by sweeping the voltage from – 1 to + 1 V. The relevant surface area was imaged before and after scanning tunneling spectroscopy (STS) measurements to ensure no tip or sample alterations occurred during the experiment. Images of the same area showed no changes after STS, except for a small lateral drift of the sample between the two scans. Presented STS are averages of 10-20 spectra taken from at least two different locations. Spectra were smoothed before differentiating to obtain the local density of states (LDOS). Bandgaps were determined from the LDOS as the distance between the onsets (inflection points) of the highest occupied molecular orbital and lowest unoccupied molecular orbital.

5.2.5 Metadynamics Simulations

To computationally sample the conformational space of WT-GrBP5 and M2-GrBP5 in both aqueous and graphene bound states, metadynamics with well-tempered ensembles was implemented.[65,66] All simulations were performed using GROMACS 2020.2 with biasing being carried out using the Plumed 2.6.1 plugin.[133,134] The peptides were modeled using the CHARMM27 force field with TIP3P water, while the polarizable INTERFACE forcefield was used to model the graphene surface.[57,58,135] All simulations were conducted at 295 K using the NVT ensemble with velocity rescaling, and a 2 fs timestep. Van der Waals interactions were calculated below a cut-off of 1 nm, and electrostatic interactions were calculated with particle-mesh Ewald summations with a 1 nm cut-off. Two sodium ions were added to the simulation box to preserve charge

neutrality. The simulation box was approximately 5 nm x 6 nm x 8 nm in dimension. The graphene surface was kept at a constant z-position of 0.5 nm throughout the entire simulation. The center of mass of the peptide was initially placed at the center of the simulation box, with a z-position 3 nm way from the graphene surface. The initial peptide conformation was produced by simulating a collapsed peptide structure in aqueous conditions for 10 ns.

Before production simulations were conducted the peptide-graphene system was energy minimized using a steepest descent algorithm. The system was then solvated with water molecules and sodium ions. The solvated system was then energy minimized a second time using the steepest descent algorithm, after which the peptide was position restrained and the solvent was allowed to adjust to the peptide conformation. The minimized system was then simulated for 500 steps to temperature couple the simulation, after which the production simulation was initiated and continued until system convergence. Two collective variables, CVs, were chosen to bias the simulation: the peptide radius of gyration of the full peptide, and the z-distance between the all-atom center of mass of the peptide and a reference surface atom. These CVs were biased using sigma values of 0.2 nm, and initial hill height of 2 kJ/mol, a bias factor of 10, and a deposition rate of 1 hill/1 ps. The center-of-mass distance was restrained using a harmonic half-potential to keep the peptide within 4 nm of the surface. This was done to limit sampling to one side of the graphene surface and accelerate convergence. Convergence was determined by tracking the relative energy difference between the adsorbed state ($z < 1.5$ nm) and the aqueous state ($z > 1.5$ nm) as a function of simulation

time. When the adsorption energy remained within thermal energy of the average energy value for the last 20-30% of the simulation, the simulation was considered converged.

5.3 Results and Discussion

5.3.1 Peptide Assembly Structure

The graphite binding peptides (GrBPs) used in this study are presented in Table 5.1. WT-GrBP5 was previously selected in our lab as the tightest binder from a combinatorial phage display library. Rationally mutated peptides, M2-GrBP5 and Truncated-M2, were designed to study the impacts of sequence on the self-assembly and binding to graphite surfaces. Our previous work demonstrated that WT-GrBP5 forms long-range ordered structures upon incubation with graphite surfaces while M2-GrBP5 forms amorphous clusters. We expanded upon this initial observation by elucidating how WT-GrBP5 and M2-GrBP5 surface binding and assembly can be modulated by thermal pre-treatment of the aqueous peptide. Namely, WT-GrBP5 forms long-range ordered structures at room-temperature while pre-heating leads to amorphous surface structure. The inverse trend was observed for M2-GrBP5. The change in self-assembly was causally related to the peptides' conformation and interactions with the graphite substrate via binding energy analysis. The experimentally determined peptide-graphite binding energies are displayed in Table 5.1. As will be seen, the GrBPs investigated herein are a prime set of peptides to study electron transport across the bio-inorganic interface due to their breadth of binding energies, self-assembly structures, and differences in sequence.

Table 5.1. Peptide sequences and graphite binding energies

Peptide Name	Sequence	Binding Energy (kcal/mol)*	
		Low Temperature	High Temperature
WT-GrBP5	IMVTESSDYSSY	31.8 ± 1.3	13.1 ± 0.9
M2-GrBP5	IMVTESSDWSSW	35.5 ± 1.0	20.7 ± 1.1

Color coding represents the chemistry of the amino acid. Blue – hydrophobic, orange – hydrophilic, red – negatively charged, black – aromatic. *Data taken from Jorgenson *et al*.

As seen in Figure 5.1, the temperature dependent self-assembly structure of WT-GrBP5 and M2-GrBP5 after a 3hr incubation on graphite surfaces confirms prior results. Specifically, at room-temperature WT-GrBP5 forms full surface coverage confluent long-range ordered surface assemblies, as evidenced by the inset fast-Fourier transform in Figure 5.1a showing six-fold symmetry. Pre-heating and incubating WT-GrBP5 at elevated temperatures results in amorphous self-assembly structures with lower total surface coverage (~28%). M2-GrBP5 maintains high surface coverage (> 60%) at both experimental temperatures studied. Room-temperature self-assemblies of M2-GrBP5 are amorphous while pre-heating and incubating at elevated incubation temperatures leads to full surface long-range ordered structures. The thicknesses of the peptide self-assembly structures presented in Figure 5.1 were within measurement error of each other with average thicknesses between 1.1 and 1.4 nm. These thicknesses suggest the peptides from monolayer structures at all studied temperatures. On average the higher-temperature assemblies were shorter than the room-temperature assemblies by approximate 0.1 nm for both WT-GrBP5 and M2-GrBP5. This subtle decease in height

suggests that at elevated temperatures the peptide conformation is flatter on the graphite surface.

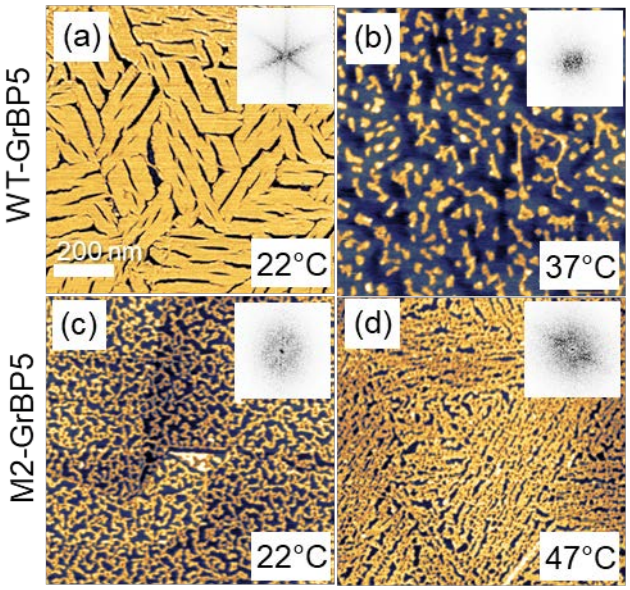

Figure 5.1. SFM images showing the self-assembly structure of (a) WT-GrBP5, and (c) M2-GrBP5 at room temperature. WT-GrBP5 (b) and M2-GrBP5 (d) self-assembly structure resulting from pre-heating and incubation at elevated temperatures. All insets are the fast Fourier transforms

5.3.2 Peptide Binding and Conformational State

As previously discussed in Chapter 3, the differences in assembly structure for WT-GrBP5 and M2-GrBP5 resulting from thermal pre-heating of the aqueous peptide solution, shown in Figure 5.1, are causally related to a peptide conformational change with differing peptide-graphite interaction strengths. The binding energies of WT-GrBP5 and M2-GrBP5 assemblies as previously determined are provided in Table 5.1. The experimentally determined decrease in binding energy for both WT-GrBP5 and M2-GrBP5 was suggested to result from the decoupling of aromatic residues from the graphite interface. For WT-GrBP5, an additional decoupling of hydrophobic interactions was hypothesized. To validate these suggested conformational details and elucidate the peptide conformations relating to the observed experimental binding energies and self-

assembly structures, metadynamics simulations were employed to map the conformational space of WT-GrBP5 and M2-GrBP5 as they absorb to a graphene surface. Figure 5.2 shows the free-energy of WT-GrBP5 and M2-GrBP5 as a function of distance from a graphene sheet at 295 K.

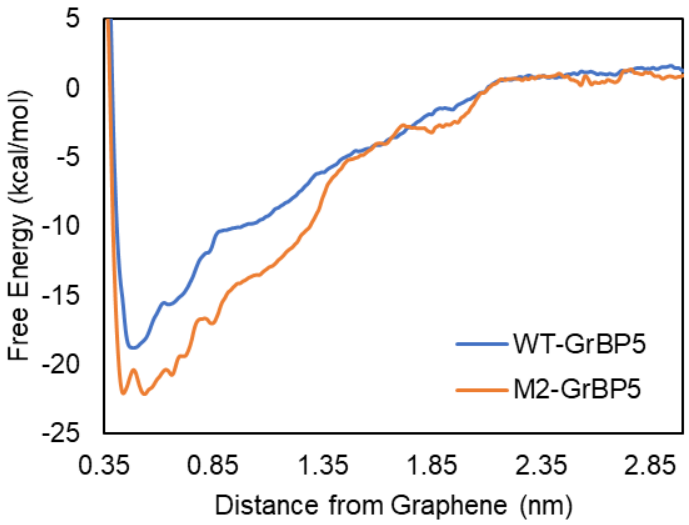

Figure 5.2. Free-energy profile for WT-GrBP5 and M2-GrBP5 adsorbing to graphene reweighted along the distance between the peptide's center of mass and the surface.

From the free-energy surfaces presented in Figure 5.2, the adsorption energy for WT-GrBP5 is found to be -16 kcal/mol at 295 K. For M2-GrBP5, the free-energy surfaces reveal an adsorption energy of -20.4 kcal/mol at 295 K. At first glance these adsorption energies do not appear to correspond the experimentally determined binding energies presented in Table 5.1. The computationally determined adsorption energies for both WT-GrBP5 and M2-GrBP 5 are approximately 15 kcal/mol lower than the experimental energies. One possible explanation for the deviation between the experimental and computational binding energies is that the computational system considers a single

graphene sheet while the experimental system considers bulk HOPG. Direct measurement of graphene's Hamaker constant by Lakshmi *et al.* revealed graphene's Hamaker constant to be approximately 55% lower than that of bulk HOPG.[136] If we assume that this decrease in interaction potential translates to a decrease in the binding energy of a peptide to graphene relative to HOPG, then the computationally observed binding energies are reasonable, i.e. 0.55 × 35.5 kcal/mol ≈ 19.5 kcal/mol for M2-GrBP5 and 0.55 × 31.8 kcal/mol ≈ 17.5 kcal/mol for WT-GrBP5.

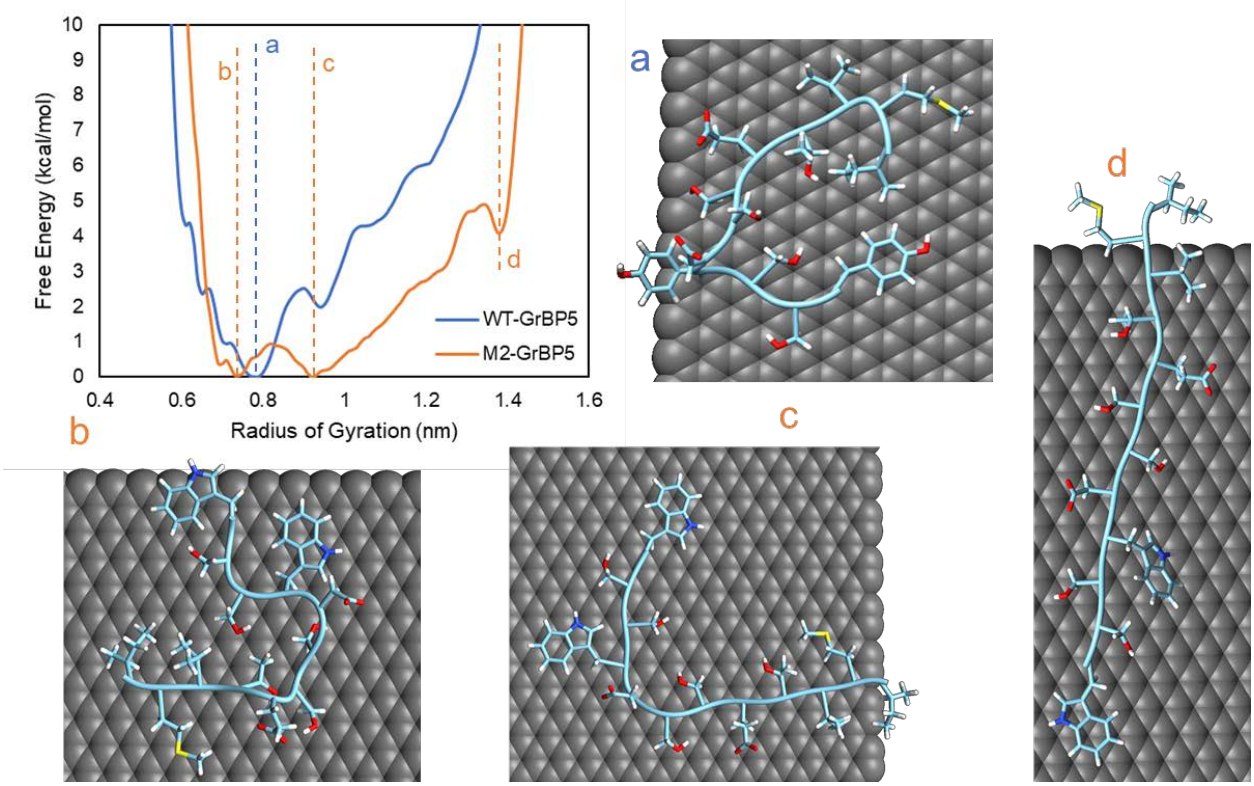

Figure 5.3. Reweighted free-energy profile for WT-GrBP5 and M2-GrBP5 on graphene reweighted along the radius of gyration. Dashed lines mark the free-energy minima marked with letters matching to the corresponding dominant conformation for WT-GrBP5 (a), and the three present conformations of M2-GrBP5 (b, c, d).

To understand what conformations of the two peptides are dominant, we analyzed the distribution of peptide conformations at the graphene surface (z < 1.5 nm). In Figure 5.3, the free-energy of WT-GrBP5 and M2-GrBP5 at the graphene surface as a function

of the peptide's radius of gyration is shown. WT-GrBP5 has one dominant well at a radius of gyration of approximately 0.78 nm with metastable but unfavorable conformational states present at higher and lower radius of gyrations. M2-GrBP5 has two equally probable conformational wells centered at radius of gyration values of 0.74 nm and 0.93 nm, respectively. A third metastable well is observed at a radius of gyration of 1.38 nm. The free energy difference between this metastable well and the main conformational wells for M2-GrBP5 is approximately 4 kcal/mol.

As shown in Figure 5.3, the dominant conformations of the peptide extracted from the different free-energy surface locations are visualized. We can assume that since WT-GrBP5 readily assembles at room-temperature that the lowest energy conformation with a radius of gyration of 0.78 nm is closest to the self-assembly conformation. The dominant WT-GrBP5 conformation is a collapsed structure with all the hydrophobic and aromatic residues contacting the graphene substrate. Heating of WT-GrBP5 would excite the peptide and allow it to take more conformations at the surface likely complicating its ability to self-assemble. One of the most dominant conformations for M2-GrBP5 at the surface is also a collapsed structure, however, comparison of backbone Cα positions between the WT-GrBP5 and M2-GrBP5 structures yields an RMSD of 4.1 Å revealing subtle conformational differences along the backbone. These observed differences in peptide conformation may be enough to prohibit M2-GrBP5 from self-assembling in the observed collapsed state. Additionally, the small energetic barrier between the two most dominant conformational states of M2-GrBP5 suggests that M2-GrBP5's conformation dispersity is higher at the surface relative to WT-GrBP5. High levels of conformational dispersity, as discussed in Chapter 3, would prevent self-assembly. The metastable conformation of

M2-GrBP5 at 1.34 nm radius of gyration is a consistent extended structure with a tryptophan decoupled from the graphene surface.

Since thermal energy would be required to access this metastable extended conformation and the observed decoupling of tryptophan from the surface matches our experimental predictions, we predict this metastable conformation is the self-assembling conformation. Moreover, the extended structure aligns perfectly with the graphene explaining the decrease in observed height for M2-GrBP5 assemblies at elevated temperature. Collectively, the metadynamics simulations presented here correspond well with previous experimental results presented in Chapter 3 and 4 elucidating the role peptide conformations and conformational dispersity play in the long-range ordering self-assembly process. In addition, the presented simulation results provide better atomistic detail about the possible self-assembling conformations of WT-GrBP5 and M2-GrBP5. However, as the peptide can take on many conformations with the same or similar radius of gyration, it is of interest to investigate the conformational space of the peptides at the surface using a different data representation so to better elucidate these conformational differences.

5.3.3 Scanning Tunneling Spectroscopy and Bandgap Analysis

Thermal processing of WT-GrBP5 yields an interface with higher conductivity relative to the room-temperature assembled interface as evidenced by I-V characteristic presented in Figure 5.4a. As shown in Figure 5.4b, I-V characteristics of room-temperature and thermally processed M2-GrBP5 are visually similar. The long-range ordered WT-GrBP5 assembled at room-temperature contains negative differential resistances at both positive (~0.1 V) and negative biases (~-0.3V - ~-0.6 V), see Figure

5.4c. The observed negative differential resistance does not appear in the electron transport characteristics of thermally processed amorphous WT-GrBP5 assemblies. However, as seen in Figure 4c, a shoulder peak is observed at ~0.4 V for thermally processed WT-GrBP5 that is not observed for the long-range ordered assembly. As seen in Figure 5.4d, shoulder peaks are observed for room-temperature assembled, amorphous M2-GrBP5 at ~-0.5 V and ~0.3 V. I-V characteristics and differential resistances for thermally processed WT-GrBP5 and M2-GrBP5 assemblies have fewer, or less pronounced, inter-band features. There does not appear to be any dependence on the electronic properties and the long range ordered structuring of the peptide. This result is expected since STS is predominantly sensitive to the local electronic properties and, as such, represent the tunneling through a single molecule.

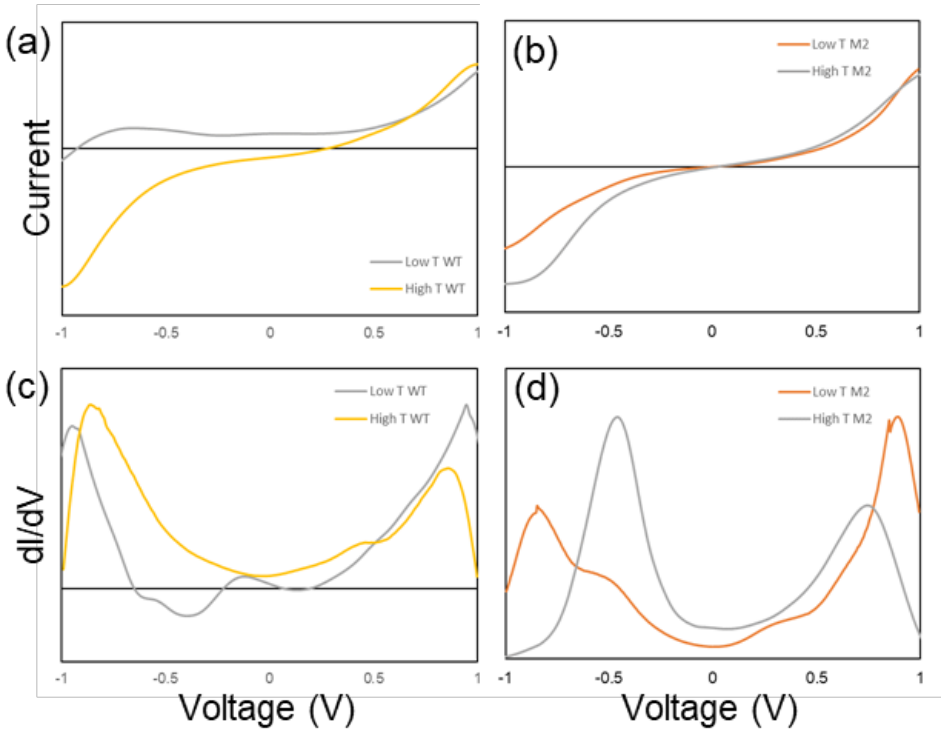

Figure 5.4. (a) I-V characteristics of long-range ordered low temperature WT-GrBP5 (grey line) and amorphous, 37 °C assembled WT-GrBP5 (yellow line). (b) I-V characteristics of amorphous room-temperature assembled M2-GrBP5 (orange line) and long-range ordered M2-GrBP5 assembled at 47 °C (grey line). (c) Differential resistance curves (dI/dV) of WT-GrBP5 I-V characteristics presented in (a). (d) Differential resistance curves of M2-GrBP5 I-V characteristics presented in (b).

Bandgaps, presented in Table 5.2, for the peptide-inorganic interfaces were extracted from the differential resistance properties of WT-GrBP5 and M2-GrBP5 presented in Figure 5.4c and Figure 5.4d, respectively. M2-GrBP5 has consistently lower bandgaps than those of WT-GrBP5 assemblies, which we postulate arises from chemical differences between the peptides, namely, the presence of tryptophan in M2-GrBP5 instead of tyrosine. Previous research has shown that tryptophan acts as a peptide dopant. Lower peptide-graphite binding energies correlate with smaller bandgaps for both WT-GrBP5 and M2-GrBP5. This is counter to our expectation that tighter binding, and thus better coupling between the peptide and graphite electron systems, would enable better transport across the interface. The tighter binding of the peptide does correspond with more inter-band features in the differential resistance properties of the peptide-inorganic interface suggesting that tight binding does create a more hybrid interface in which the peptide plays a larger role in the electron tunneling. An explanation for the smaller bandgap for thermally processed assemblies could be these high-temperature assemblies possessed, on average, smaller thicknesses. Given the exponential dependence of the tunnel current on the tip-graphite distance and the potential barrier thickness, the thinner peptide layers can have an appreciable impact on the electron tunneling across the interface. As shown in Table 5.2, the bandgap and binding energies (in eV) do not correspond in a 1-to-1 fashion suggesting that the STS experiment did not ablate the peptide from the surface and that bandgap is not simply a secondary representation of the binding energy of the peptide to the graphite substrate.

Table 5.2 Peptide-Inorganic Interface Bandgaps and Binding Energies

Peptide Name	Room-Temperature Assemblies		High Temperature Assemblies	
	Bandgap (V)	Binding Energy (eV)	Bandgap (V)	Binding Energy (eV)
WT-GrBP5	1.09 ± 0.04	1.38 ± 0.06	0.77 ± 0.02	0.57 ± 0.04
M2-GrBP5	0.98 ± 0.04	1.54 ± 0.04	0.83 ± 0.01	0.85 ± 0.05

5.4 Concluding Remarks on Molecular Control over Electronic Transport across Peptide-Inorganic Interfaces

Understanding the conformation of solid-binding peptides at their target surface is critical to design bioelectronic interfaces with tailored assembly structures, and as demonstrated in this chapter, with designer electronic transport properties. Even with the same peptide sequence, differing peptide conformations of the peptide as controlled by environmental conditions result in dramatically different electronic tunneling properties of the hybrid peptide-inorganic interface. Thinner peptide structures with lower coupling between the peptide and graphite surface enable better electronic tunneling across the inorganic interfaces. While peptides more strongly bound to the graphite surface demonstrated lower conductivity or even semiconducting properties due to the pronounces role of the peptide's molecular detail in determining the transport pathway. Depending on the bioelectronic application of interest, either of these peptide-inorganic interfaces can be of use. For instance, in electrochemical biosensor, less tightly bound, thinner peptide structures would be beneficial as better electron transport between the biological environment and the inorganic surface would enable more sensitive devices. On the other hand, for molecular electronics in which the peptide layer acts as an active material, the more tightly coupled peptide with complex electron transport pathways would be of interest, e.g., the negative differential resistance present in ordered WT-GrBP5 assemblies. Collectively the results presented herein show how knowledge of the

conformational space of a peptide can be leveraged to tailor interfaces through control over the molecular structure of the peptide-inorganic interface.

Chapter 6:
Impacts of Molecular Recognition on Peptide Miscibility and Binary Nucleation

As discussed in the previous chapters, the sequence in combination with the environmental conditions dictates a peptides conformation. The conformation is critical for determining peptide-peptide and peptide-substrate interactions. In this chapter, the effects of sequence and peptide-substrate interactions are investigated to elucidate fundamentals on the molecular scale miscibility of peptides in binary systems and the nucleation of binary assemblies.

6.1 Introduction

The co-organization of disparate materials into hierarchically assembled constructs is key to developing functional nano- and biotechnologies. For example, multienzyme complexes enable complex chemical pathways that overcoming diffusional limitations, while the nanoscale organization of quantum dots significantly tunes their photophysical properties.[137-143] Critical to the engineering of emerging nanobiotechnologies is the rational organization of inorganic and biological materials. To this end a variety of strategies have been developed, such as enzyme fusions, engineered bacteria, and surface immobilization.[12,144-149]

Functionalization of surfaces with biomolecules is of particular interest for the development of biosensing, bioelectronic and biofuel cell technologies.[118,121,145,150,151] Efficiencies and efficacies of these systems could be enhanced via biomolecular immobilization strategies that dictate the absorbed biomolecular density, orientation and conformational stability.[121,145] Detrimental effects, were found for simple physisorption

such as protein denaturation and loss of activity, which thus, decreased the overall device functionality.[150] To enhance the control over biomolecular immobilization onto surfaces, several strategies have been developed, which rely on biomolecular modifications involving chemical groups that facilitate surface adsorption and linkage.[122,152,153] Despite these successes, simultaneous control over the geometrical display, spatial distribution, and organized patterning of biomolecules towards full benefit of the surface functionalization remains limited. This level of control over the microscopic topology of the adsorbates is especially critical for the multiplexed patterning of several biomolecules at solid surfaces.[153]

Biomolecular self-assembly has shown to be a powerful approach to tailor interfaces and materials in both naturally occurring and man-made systems.[71,154-156] Engineered proteins and peptides have been designed to self-assemble at atomically flat two-dimensional solid surfaces with a variety of organized nanostructures.[123,157,158] Among these biomolecules, solid binding peptides which are genetically selected through directed evolution for substrate specificity have emerged as a prominent strategy for bio-functionalization of inorganic surfaces.[20,21,159] Solid binding peptides have been used as molecular building blocks to control surface immobilization and the displaying a variety of nano-entities at solid surfaces.[20,95,96] Certain solid binding peptide sequences provide the possibility of hierarchical structuring of materials as they form confluent, long-range ordered nanostructures that are commensurate with the underlying solid's crystal lattice.[31,108] Additionally, external factors such as pH, temperature, and concentration provide engineering controls over the equilibrium self-assembly structure.[124-126]

The wealth of peptide sequence space allows for the facile implementation of a great multitude of substrate and process tailored biomolecular self-assembly systems. While self-assembling peptides have been successfully implemented to display biomolecules at device interfaces, only recently has the fabrication of binary assembled peptide functionalizations been appreciated and attempted.[127,160] For example, two sequence differing peptides each known to form ordered surface assemblies would enable highly tuned mixed surface structures with designed functionality. Despite these early realizations, for the rational engineering of biomolecular surface functionalizations with independently tailorable phases, a better understanding of miscibility between disparate peptides and their binary assemblies is of critical importance. Specifically, whether the two peptide components co-assemble into a single crystalline order, or self-sort into separate crystalline phases. Additionally, there exists a need for models that accurately predict the binary assembly structure and identify the key parameters controlling the total surface coverage, density, and size of the self-assembled domains.

Towards this goal we investigated the assembly structure of two solution-blended combinatorially selected graphite binding peptides (GrBPs), a wild-type version, WT-GrBP5, and its double serine residue N-terminated analogue, SS-GrBP5. Prior work revealed biotinylated versions of WT-GrBP5 and SS-GrBP5 were miscible within their respective unmodified peptide assemblies, thus, making them excellent candidates for biofunctionalization of graphene biosensing surfaces.[27] In addition, the sequence similarity between WT-GrBP5 and SS-GrBP5 and their high propensity to form long range ordered structures at graphite interfaces, makes them prime candidates for investigating two-dimensional binary assembly and local molecular miscibility. While prior works

extensively studied the assembly properties of WT-GrBP5, focusing on an observed amorphous-to-ordered transition and the effects of environmental conditions, the studies lacked a rigorous analysis of the peptide domain nucleation itself.[31,125] Here, we directly analyze WT-GrBP5 and SS-GrBP5 nucleation kinetics in terms of the classical nucleation theory (CNT). Herein, dubbed as symbiotic assembly of binary peptide mixtures, we provide a rigorous understanding of the complex biomolecular patterning at atomically flat crystal interfaces. This symbiotic assembly platform represents a highly tunable method for the fabrication of high-density biomolecular nano-mosaics with wide ranging nanobiotechnological applications, e.g., multiplex biosensing for binary biomarkers, multicomponent bioelectronics, and spatially enhanced quantum dot devices.

6.2 Experimental Methodology

6.2.1 Peptide Synthesis and Assembly

The graphite binding peptides were synthesized on a preloaded support resin using HBTU activation chemistry and Fmoc deprotection as previously described.[125] Synthesized peptides were purified by HPLC (Waters Deltaprep 600, Semiprep Mode) using linear gradients of 1% per minute at a flow rate of 10 mL/min. MALDI-TOF mass spectrometry with reflectron (RETOF-MS, Autoflex II, Bruker Daltonics, Billerica, MA) was used to confirm the purified peptides' molecular weight.

All self-assembly samples were prepared on freshly cleaved highly oriented pyrolytic graphite (HOPG grate 1, SPI, Inc.) with an approximate area of 0.25 cm^2. Cleaved graphite surfaces were incubated with 40 µL of peptide in DI water for 2 hours with a variable peptide concentration. Peptide solutions were wicked from the incubated

graphite surfaces. Residual solution was blown from the graphite surface and dried using a stream of nitrogen.

6.2.2 Scanning Force Microscopy (SFM) Imaging

The self-assembly structure of the dried samples was visualized under ambient conditions using a DI Nanoscope IIIa SPM (Digital Instruments) in tapping mode using soft tapping mode SFM probes (HQ:NSC14, MikroMasch). Atomic resolution of the graphite lattice was obtained using a DI Nanoscope IIIa SPM in contact mode with appropriate SFM probes (VistaProbes).

6.2.3 Assembly Structure Analysis

SFM images were analyzed using the Gwyddion SPM data analysis software.[47] Features in the fast Fourier transforms (FFTs) of the SFM images were used to determine the relative angles of the (i) peptide nanostructures in co-assemblies as well as between (ii) peptide nanostructures and the graphite lattice. All analyzed images were 1×1 μm in size. As the broad structure of the peptide nanowires impedes the clear distinction between directions in the FFT, SFM images were first masked to distinguish the peptide nanostructure from the graphite substrate. The mask was then binarized and Fourier analysis was performed on the binarized image. Angles within the FFT were measured by hand. Angles were extracted from three images of each peptide assembly condition from which averages and standard deviations were determined. Samples of WT-GrBP5 and SS-GrBP5 co-assemblies were averaged together. Beyond angles present in the self-assembled peptide nanostructures, the size and density of unidirectional ordered domains, or grains, was analyzed. The density of grains was used to estimate the nucleation rate of the long-range ordered structures. Thereby, we assumed that the

number of ordered domains is equivalent to the number of nuclei and that minimal coarsening occurred. Masks separating the peptide from the graphite surface were manually edited to separate these grains. The grain density and average area were averaged over three different SFM images.

6.3 Results and Discussion

WT-GrBP5 was determined as the strongest graphite-binding peptide from a combinatorial selection process.[31] The addition of two serine residues at the N-terminus, yielding SS-GrBP5, increases the hydrophilicity of the peptide while maintaining other chemical and functional properties, i.e., high-binding affinity, binding strength, and long-range ordered assembly.[125] The chemistry and sequence information of WT-GrBP5 and SS-GrBP5 can be found in Table 6.1.

Table 6.1. Peptide Sequence and Chemical Information.

Peptide Name	**Sequence**	**Molecular Weight** (Da)	**GRAVY**
WT-GrBP5	IMVTESSDYSSY	1381.5	-.242
SS-GrBP5	SS-IMVTESSDYSSY	1555.6	-.321
The Grand Average of Hydropathicity Score (GRAVY) identifies the relative hydrophilicity. The more negative the number the more hydrophilic the peptide.			

Figures 6.1(a-f) present 2-hour assemblies of 0.5, 0.75 and 1 μM concentrations of WT-GrBP5 and SS-GrBP5 with indistinguishable confluent, high surface coverage films at 1 μM. Approximate film heights of 1.5 nm for WT-GrBP5 and SS-GrBP5 suggest monolayer assemblies. Both WT-GrBP5 and SS-GrBP5 form six-fold symmetric, long range ordering, as evidenced by fast Fourier transforms (FFTs) (insets of Figures 6.1(c,f)). As shown in Figures 6.1(a-c) and 6.1(d-f), respectively, WT-GrBP5 and SS-GrBP5 exhibit an increase in long-range ordered domains with increasing concentration. Growth differences are noticeable at low peptide concentrations, where SS-GrBP5

exhibits fewer aggregates, slimmer structures, and more ordered domains in comparison to WT-GrBP5. The addressed dissimilarity in the nucleation process of the two peptides, the observed amorphous-like clustering at low concentrations and inherent two-dimensionality (2D) of the system, invites a 2D CNT analysis of the two single phase assemblies.

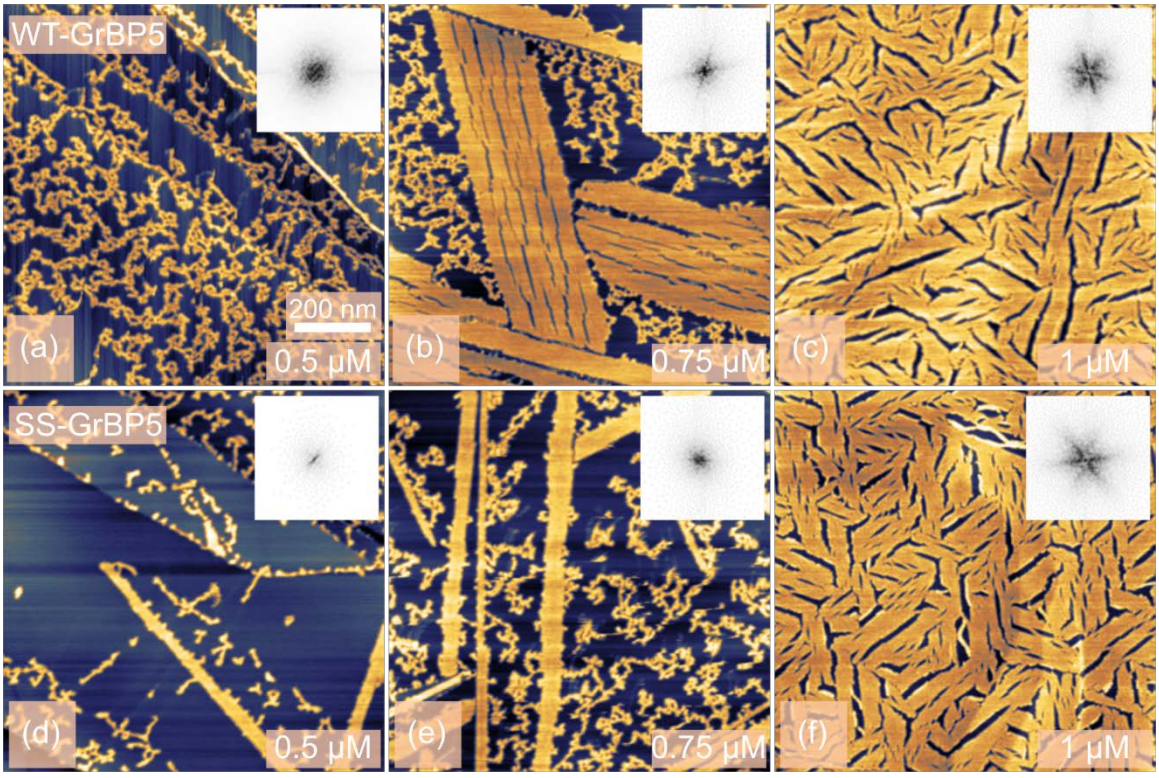

Figure 6.1. Self-Assembly structures resulting from 2-hour incubations of WT-GrBP5 at (a) 0.5 μM, (b) 0.75 μM, and (c) 1 μM at graphite surfaces. Single component self-assemblies of SS-GrBP5 at the same concentrations (d-f).

We consider the energetic nucleation free energy Δg_n for the formation of an assembly cluster to be the sum of the free energies of the bulk crystal phase, Δg_b, and the crystal interface, Δg_s.[44,45] Δg_b is given by the chemical potential difference of the single peptide (monomer) and the peptide crystal assembly, $\Delta\mu$, the area per monomer, A_m, and the radius of the cluster, r, as $\Delta g_b = (\pi r^2/A_m)\Delta\mu$. Δg_s is determined from the line tension at the crystal-substrate interface, λ, and the size of the cluster, as $\Delta g_s = 2\pi r\lambda$. Thus, at

equilibrium, where the cluster size is determined to be $r \equiv r_c = \lambda A_m/\Delta\mu$, the nucleation free energy is $\Delta g_n = \pi A_m \lambda^2/\Delta\mu$. If we consider further that $\Delta\mu$ is given by the activity α of the system, i.e., $\Delta\mu = kT\ln(\alpha)$, which can be related to the activity coefficient □, the peptide solution concentration C and the equilibrium concentration C_e, as $\alpha = \gamma(C/C_e)$, the free energy barrier, Δg_n, associated with a 2D circular critical nuclei is given by,

$$\Delta g_n = \frac{\pi A_m \lambda^2}{kT\left(\frac{C}{C_e} - 1\right)} \quad Equation\ 6.1$$

assuming ideality (□ ≈ 1) for low concentration (see Supplemental Information for more details). k is the Boltzmann constant, T is the absolute solution temperature, and, $\left(\frac{C}{C_e} - 1\right)$ represents the supersaturation or activity of the system. With the nuclei free energy Δg_n, we can express for $C > C_e$ the 2D nucleation rate as follows:

$$\frac{dn}{dt} = Ae^{-\frac{\Delta g_n}{kT}} = Ae^{\left(-\frac{\pi A_m \lambda^2}{(kT)^2\left(\frac{C}{C_e}-1\right)}\right)} = Ae^{\left(\frac{-B}{\left(\frac{C}{C_e}-1\right)}\right)} \quad Equation\ 6.2$$

where n is the number of nuclei, A is a complex pre-exponential factor, and B is a dimensionless factor combining the geometric and energetic parameters of the system. As implied by Equation 6.2, the relationship between the nucleation rate and the peptide concentration is non-linear, which as we present next, will fit our data well.

Figure 6.2(a, b) provide the experimentally determined nucleation rate as a function of the peptide concentration, determined from the data in Figure 6.1 for WT-GrBP5 and SS-GrBP5, respectively. Nucleation rates were estimated from the number of long-range ordered domains per area and incubation time, as described in the experimental section. The nucleation parameters in Table 6.2 were obtained from the fits in Figure 6.2. The fit quality let us conclude that WT-GrBP5 and SS-GrBP5 nucleation is

well described by the classical 2D nucleation theory. As anticipated from the results in Figure 6.1, WT-GrBP5 and SS-GrBP5 nucleation kinetics are similar with only subtle differences in fit factors. While the applicability of 2D nucleation theory shown herein is not surprising, we note that the inherent 2D confinement does not preclude the 1D nucleation of peptide nanostructures. As recently investigated by Chen *et al*., solid binding peptides assembling at MoS_2 interfaces displayed no observable nucleation barrier, and, the nucleation varied linearly with concentration.[108] We attribute the here observed non-linear peptide nucleation processes to the complex relationship between peptide sequence, conformation, intermolecular interactions, and self-assembly. WT-GrBP5 and its mutations self-assembly has previously highlighted this complexity by exhibiting

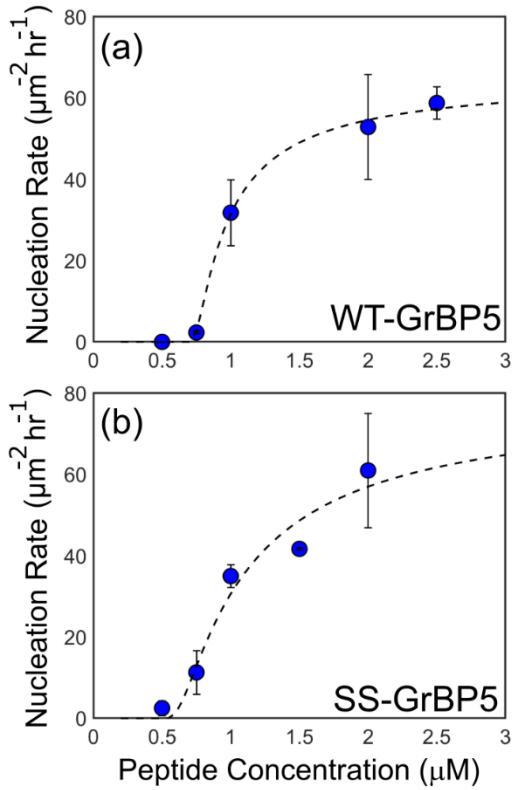

Figure 6.2. Nucleation rates for (a) WT-GrBP5 and (b) SS-GrBP5. Dotted lines are from Equation 6.2 using fit parameters in Table 6.2.

conformational dependent self-assembly that can be (de)activated by thermal pre-processing.[124,125]

Table 6.2. Two-Dimensional Nucleation Parameters for Peptide Assembly.

Peptide Name	***A*** $(1/\mu m^2 hr)$	***B***	C_e (μM)
WT-GrBP5	65.2	0.34	0.68
SS-GrBP5	78.8	1.03	0.48
Obtained from fits of Equation 6.2 to the nucleation rates in Figure 6.2.			

Having obtained an understanding about the individual WT-GrBP5 and SS-GrBP5 self-assembly processes, we focus next on how individual dynamics translates into the binary assembly process involving peptide mixtures. Figure 3 shows the self-assembly structures resulting from 50:50 mixtures of WT-GrBP5 and SS-GrBP5 at total concentrations between 1 and 2 µM. As demonstrated in Figure 6.3(b) and its inset FFT, the 50:50 mixtures yield high surface coverage monolayers with long-range order. Comparing the microstructures of the mixture (Figure 3) to the single-phase assemblies (Figure 6.1), it is apparent that the binary self-assembly structure diverges from that of the two pure peptide assemblies. Specifically, comparing the 1 µM total peptide concentration of the binary mixture, Figure 6.3(a), to the 1 µM single phase systems, Figure 6.1(c, f), revealed lower surface coverage and less long-range ordering in the binary system. Yet, contrasting the 1 µM 50:50 mixture, Figure 6.3(a), to the equivalent concentration of the single-phase peptides, (i.e., 0.5 µM WT-GrBP5 and SS-GrBP5) in Figure 6.1(a, d), reveals a higher degree of ordering in the binary system. Moreover, the size of the ordered domains in the binary 50:50 mixture is on average ~0.4 the size of the

ordered domains present in pure WT-GrBP5 or SS-GrBP5 assemblies of equal concentration. Collectively, these results suggest that WT-GrBP5 and SS-GrBP5 are immiscible, and, nucleate and grow their long-range ordered structures competitively.

Figure 6.4(a) demonstrates that nearly right-angle growth patterns form in the 50:50 binary assembly mixtures that break from the six-fold symmetry found for single phase systems, thus, suggesting the peptides competitively grow along well-defined substrate induced growth directions. The presence of the close to right-angles documents a ~20° to 30° offset between the WT-GrBP5 and SS-GrBP5 crystallographic assembly directions. Closer FFT analysis of angles in Figure 6.3 reveal a 24° ± 7° offset between FFT features. Comparing the single-phase self-assembly direction with the 0001 direction of the underlying graphite lattice reveals that WT-GrBP5 assembles at an orientation of 1° ± 7° relative to the zig-zag direction, Figure 6.4(c), while SS-GrBP5 grows along an angle of approximately 22° ± 6° from the zig-zag direction, Figure 6.4(d). The difference between the two growth orientations yields an offset of approximately 21° ± 9° between WT-GrBP5 and SS-GrBP5 assemblies, a result within the error of the FFT analysis. The assembly directions of WT-GrBP5 and SS-GrBP5 are schematized in Figure 6.4(b) depicting the expected offset of ~81°. The divergent growth directions for WT-GrBP5 and

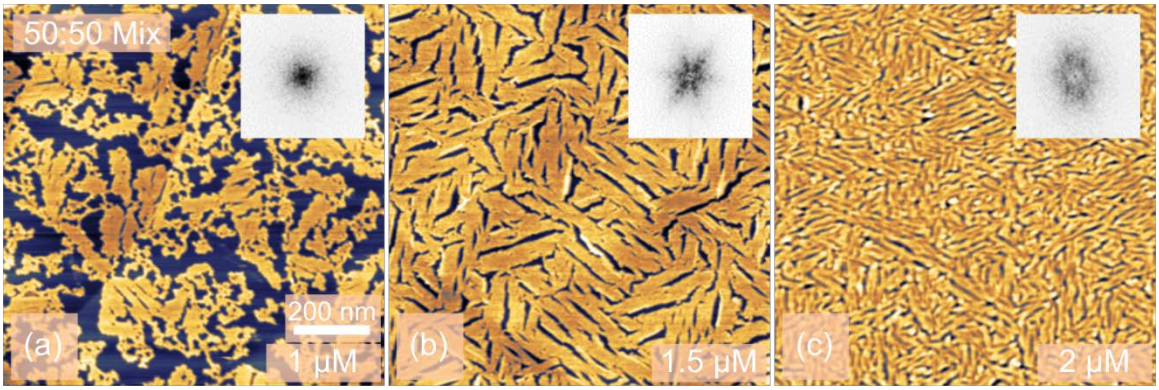

Figure 6.3. Self-assembly structure resulting from 2-hour incubations of 50:50 mixtures of WT-GrBP5 and SS-GrBP5 with total peptide concentrations of (a) 1 μM, (b) 1.5 μM, and (c) 2 μM.

SS-GrBP5 provide a molecular rational for the observed immiscibility and competitive assembly. While WT-GrBP5 and SS-GrBP5 compete for the same surface area, the orientational, non-congruent growth directions of the two peptides inhibit a strictly molecular co-assembly process. The result demonstrates a *symbiotic growth partitioning* of surface area, yielding a highly organized and dense assembly pattern that surpasses the single-phase assemblies.

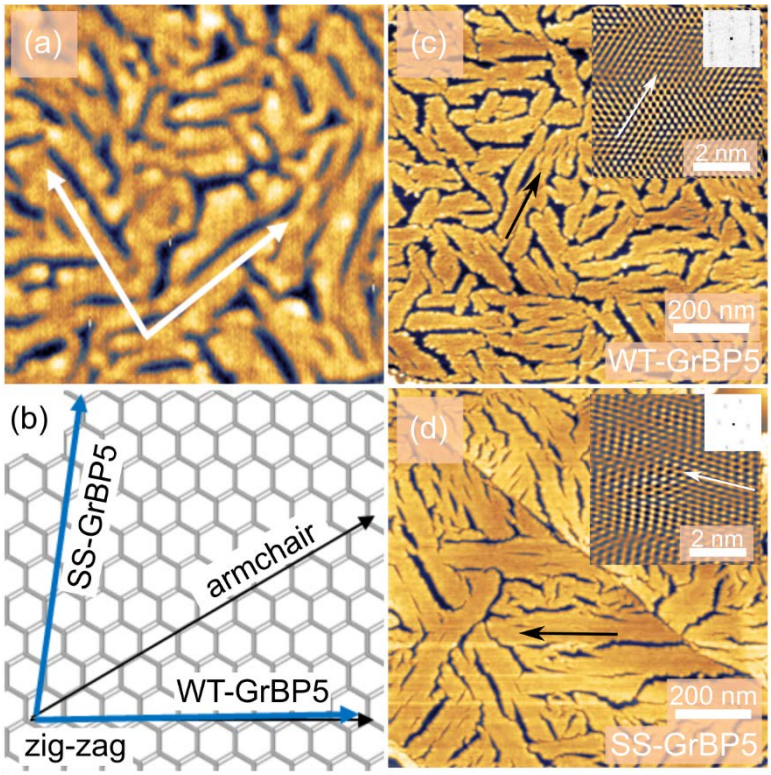

Figure 6.4. Topology images of (a) 50:50 mixture of WT-GrBP5 and SS-GrBP5 with inset white arrows highlighting the experimentally determined offset. (b) Schematic angle relationship between WT-GrBP5 and SS-GrBP5 with the underlying graphite lattice. The blue arrows indicate major peptide growth directions. (c-d) WT-GrBP5 and SS-GrBP5 assemblies with insets of the FFT filtered underlying graphite atomic lattice. White arrows point out the zig-zag direction of the lattice

To evaluate the nucleation rate in the peptide mixtures, we return to the 2D CNT analysis and extend it by taking the linear superposition of WT-GrBP5 and SS-GrBP5 nucleation kinetics and considering the molar fraction of each component in the binary assembly, Equation 6.3. We set ζ and 1- ζ to be the molar fraction of WT-GrBP5 and SS-GrBP5, respectively, which yield for the binary nucleation rate:

$$\frac{dn}{dt} = \frac{A_{WT}}{\zeta} e^{\left(\frac{-B_{WT}}{\zeta^2\left(\frac{C}{C_{e,WT}}-\zeta\right)}\right)} + \frac{A_{SS}}{(1-\zeta)} e^{\left(\frac{-B_{SS}}{(1-\zeta)^2\left(\frac{C}{C_{e,SS}}-(1-\zeta)\right)}\right)} \quad Equation\ 6.3$$

The introduced molar fraction ζ acts as a scaling parameter to adjust for the concentration dependent competitive growth conditions of the immiscible, binary system. While the molar fraction, ζ, is given by the experimental peptide mixture ratio, the fit parameters A_{WT}, A_{SS}, B_{WT}, B_{SS}, $C_{e,WT}$, and $C_{e,SS}$ were obtained earlier from the single phase assemblies, as provided in Table 2 as A, B, and C_e for WT-GrBP5 and SS-GrBP5, respectively. It is important to note that for Equation 6.3 no new fit parameters were introduced. As shown in Figure 6.5, an excellent fit is found between Equation 6.3 predicted nucleation rates and the nucleation rates obtained from assembly data shown in Figure 6.3.

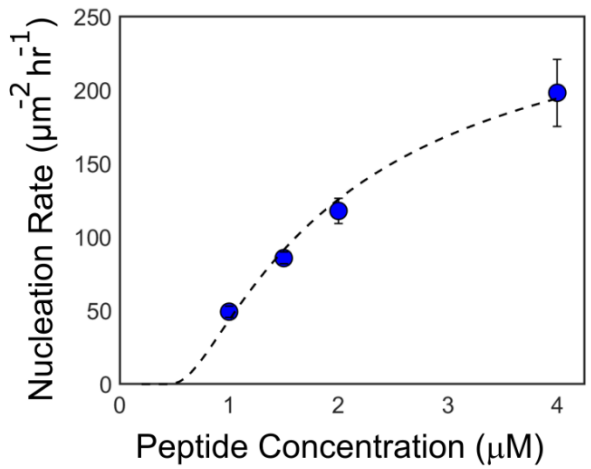

Figure 6.5. Nucleation rate of 50:50 binary mixture of WT-GrBP5 and SS-GrBP5. Equation 6.3 using fit parameters in Table 6.2 and ζ of 0.5 results in the dashed black line.

Based on the quality of fit in Figure 6.5 we find that the introduced scaling of the single-phase nucleation kinetics in Equation 6.3 accurately expresses the observed symbiotic assembly process. The presence of two peptide phases augments the growth

partitioning of both phases as evidenced by the increase in the kinetic pre-factors, A_{WT}/ζ and $A_{SS}/(1-\zeta)$. In addition, the two phases cause a divergence from ideality, ($\gamma \neq 1$), i.e., leading to a shift in the supersaturation or increase in the activity, thus, providing a greater driving force for the nucleation process. With the augmentation of the ratios B_{WT}/ζ^2 and $B_{SS}/(1-\zeta)^2$, considering their respective molar fractions, the nucleation rate of the constituent peptides vanishes as expected when its molar fraction approaches zero.

The apparent ad-hoc scaling presented in Equation 6.3 can be justified as follows. We consider that the preexponential factor of the classical nucleation theory for a single phase is given by

$$A = ZjN_s \quad Equation\ 6.4$$

where Z is the Zeldovich factor that accounts for the sticking probability of a molecule onto the critical nuclei, j is the molecular attachment rate, and N_s is the density of nucleation sites.[45] The dynamic quantity Zj can further be approximated using the diffusion coefficient of the nucleus, D, and the mean free path of the monomer, l, as, $Zj = 2D/l^2$. While D remains unchanged for binary systems, the average area probed by a monomer prior to any collision (assembly attempt), l^2, decreases with decreasing ζ, as the co-existing phase consumes more surface area. This leads to a binary growth partition of $Zj = 2D/\zeta l^2$ and the kinetic pre-factor A/ζ. Additionally, it has to be considered that a decreasing surface area increases the local density of monomers, and thus, reduces C_e with diminishing ζ resulting in a divergence from ideality of $\gamma=1/\zeta$ and activity $\alpha = (C/\zeta C_e)$. The chemical potential difference for the binary system is thus $\Delta\mu = kT[(C/C_e) - \zeta]$ for small concentrations. The empirically introduced ζ produces a non-physical limit that for $\zeta \rightarrow 0$, $A \rightarrow \infty$. To avoid a non-physical limit, Δg_n is augmented

to balance the diverging kinetic pre-factor by scaling the line-tension λ/ζ. Thus, for the binary system $B \propto (\lambda/\zeta)^2$. Combined, the outlined implementation of ζ produces the binary nucleation rate as introduced in Equation 6.3 above.

So far, we investigated 50:50 mixtures of WT-GrBP5 and SS-GrBP5. Next, we explore the nucleation rate as a function of the molar fractions for $0 < \zeta < 1$ at a total peptide concentration of 2 μM after an incubation time of two hours. Figure 6.6(a-c) shows high quality self-assembly structure for 25:75, 50:50, and 75:25 mixtures of WT-GrBP5 and SS-GrBP5. Thus, long-range ordered structures are found to be independent of the molar fraction for a 2 μM total peptide concentration. Figure 6.6(d) further highlights the validity of our nucleation model (Equation 6.3) by matching the measured nucleation rates. Within the molar fraction range of $0.25 < \zeta < 0.75$ the nucleation rate is augmented significantly over the predominantly single-phase systems with an experimental maximum at $\zeta = 0.5$, by a rate amplification factor of up to two. As documented in Figure 6.6(e) with the grain area plot *vs.* molar fraction, on average the long-range ordered domains are significantly smaller at $\zeta = 0.5$ compared to the other phase mixtures. At total concentrations above 1 μM, a simple linear relationship exists between the nucleation rate and the grain area allowing the determination of the grain area using Equation 6.3 (see dashed line in Figure 6.6(e)) Further details are provided in the Supplementary Information. This finding invites single parameter control over the ordered domain size, and thus, bears practical importance for instance for nanoscale patterning of bioreaction cascades to overcome diffusional limitations on reaction rates. Collectively, the results

presented in Figure 6.5 and Figure 6.6 demonstrate that the molar fraction and total peptide concentration are key parameters controlling the self-assembly structure.

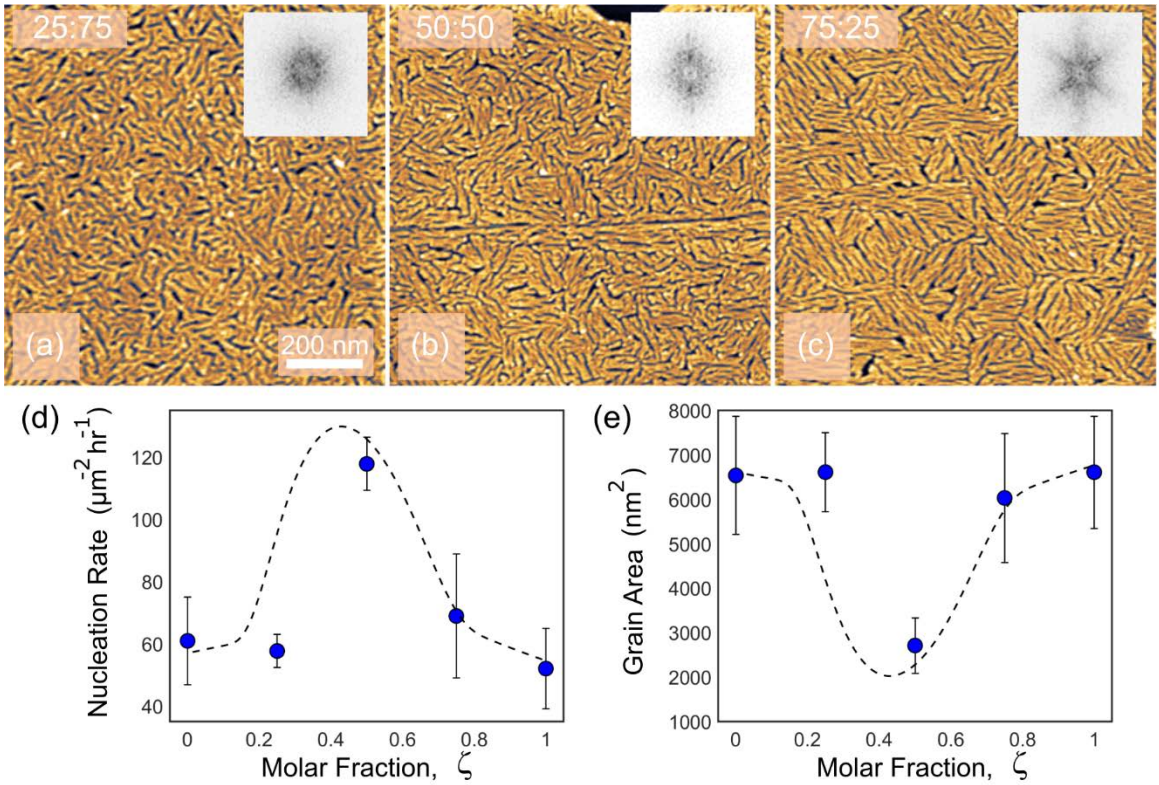

Figure 6.6 Assembly structure of (a) 25:75, (b) 50:50, and (c) 75:25 mixtures of WT-GrBP5 and SS-GrBP5. Insets are the fast-Fourier transform of the SFM image. (d) nucleation rates and (e) grain area as a function of WT-GrBP5 molar fraction, ζ. Predicted nucleation rate from Eqn. 3 is the black dashed line in (d). The black dashed line in (e) is the predicted grain area using a linear translation of nucleation rates predicted by Equation 6.3.

6.4 Concluding Remarks on the Symbiotic Nucleation of Binary Assemblies

Binary assembly of the two solution-blended combinatorially selected graphite binding peptides, WT-GrBP5 and SS-GrBP5, produced high quality self-assembled monolayers consisting of two immiscible ordered phases. Binary assemblies exhibited equal quality but exceeded in density the single-phase assemblies. The relative orientational difference in the growth-direction of the immiscible phases of approximately 25° could be attributed to the crystallographic growth direction of the single-phase

peptides, namely, approximately the zig-zag direction of the graphite lattice for WT-GrBP5 and close to the armchair direction of the graphite lattice for SS-GrBP5. The binary nucleation process was found to function cooperatively, and thus, augmenting the constituent peptide nucleation kinetics in a so-called *"symbiotic"* fashion. Parameters obtained from fitting the single-phase assemblies with a two-dimensional nucleation model, translated seamlessly to describe the symbiotic assembly process using the molar fraction as a scaling parameter. Peptide concentration and peptide molar fraction were found to be the sole critical growth parameters with which the nucleation rate and self-assembly structure can be controlled.

The summarized results of this symbiotic binary assembly study demonstrate the complexity of peptide miscibility and self-assembly. Since WT-GrBP5 and SS-GrBP5 form separate self-assembled phases, they are immiscible at the molecular scale. However, due to specific peptide-graphite molecular recognition resulting in compatible nucleation and assembly phenomena, WT-GrBP5 and SS-GrBP5 assemblies are apparently miscible at the macroscopic level allowing confluent monolayers. The ability to fabricate polycrystalline interfaces at the macroscopic scale while maintaining molecular level specificity greatly facilitates the development of biomolecular patterned hybrid systems. One could envision controlling the symbiotic assembly of three or more peptides, thus, forming a highly tunable interfacial biomolecular mosaic. To enable the rational design of such bio-inorganic interfaces, further research is needed to understand the role of peptide conformation on peptide-substrate molecular recognition and peptide-peptide intermolecular interactions. Collectively, the presented results demonstrate the ability to control and predict the supramolecular patterning of bio-inorganic interfaces *via* symbiotic

assembly of binary peptides, thus enabling the fabrication of multiplexed biomolecular electronics, biofuel cells, and quantum dot technologies.

Chapter 7:
Impacts of Lateral Confinement on Peptide Self-Assembly

In the previous chapters, the impact of peptide sequence and conformation in conjunction with environmental factors has been explored to understand the interactions and self-assembly phenomena of peptides on two-dimensional inorganic substrates. In this chapter, substrate effects are interrogated. Specifically, the results and studies presented here demonstrate the role of lateral confinement created by graphite substrates of differing size and shape on the adsorption and self-assembly of a graphite binding peptide.

7.1 Introduction

In nature, the spontaneous formation of materials and interfaces with complex nanoscale structure and patterning is of critical importance for biological functions such as environmental sensing, cell metabolism, and mineral formation.[156] For the development of bioelectronic nanotechnologies such as biosensors it is of interest to fabricate interfaces that mimic functionality of naturally occurring systems.[122,144,161] To this end several engineering systems have been developed to tailor the inorganic interfaces through the self-assembly of molecules, for instance, self-assembled organic monolayers.[73,121] A recent and very promising means of fabricating complex surface assemblies has been the use of self-assembling biomolecules.[123,157,162]

Of specific interest of this work are solid binding peptides which have been extensively introduced in the preceding chapters as highly tunable linkers and assemblers of complex bio-inorganic interfaces for bioelectronic technologies.[26,95,96,127] Given the

utility of SBPs, the focus of this Thesis is the development of a fundamental understanding of peptide self-assembly at inorganic interfaces. As detailed in Chapter 2, and explored in Chapters 3 through 6, the formation of these interfaces results from the adsorption of aqueous peptides, diffusion of the peptides on the inorganic surface, and favorable peptide-peptide interactions. The primary interest of most research efforts, and the focus of the preceding chapters, has been the elucidation of how sequence and environmental parameters impact long-range ordering to enable engineering handles over the formation of these hybrid bio-inorganic interfaces.[124-126,160]

While the role of the peptide and environment have been extensively studied (as presented in Chapters 3 and 4), the role of the substrate has not been adequately interrogated for these systems. In particular, the impact of different substrate preparation methods and the size of the substrate have not been explored. Previous experimental interrogations of the organization of synthetic organic molecules have shown the importance of nanoscale lateral confinement on the organic monolayers self-assembly and structure.[163,164] As a first step towards understanding substrate effects on the spontaneous formation of peptide-inorganic interfaces, this chapter interrogates the difference between peptide adsorption and self-assembly of a graphite binding peptide, denoted M6-GrBP5, on exfoliated graphite flakes of micron size and pristine highly oriented pyrolytic graphite (HOPG).

HOPG is the “gold standard” of graphite substrates for the study of peptide self-assembly. Exfoliated flakes are the preferred material for preparing pristine graphene substrates with lateral dimensions on the order of microns for device purposes, i.e., printed graphene field effect transistors. M6-GrBP5 has the amino acid sequence of

IMVTASSAYDDY and is a mutant of a previously selected graphite binding peptide.[25] M6-GrBP5 is a perfect candidate to interrogate the effects of substrate size and preparation as it was found to form long range ordered structures on exfoliated graphite flake surfaces, but as will be seen, has limited self-assembly capabilities on HOPG. As nanomaterials, like graphene, become more integral to advanced bioelectronic devices, understanding how to translate fundamental results from pristine bulk material studies will be critical for the development of nanoscale bio-inorganic interfaces.

7.2 Experimental Methodology

7.2.1 HOPG versus Graphite Self-Assembly

One set of self-assembly samples were prepared on freshly cleaved highly oriented pyrolytic graphite (HOPG grate 1, SPI, Inc.) with an approximate area of 0.25 cm^2, by incubating the cleaved graphite surfaces with 40 µL of M6-GrBP5 in DI water for 2 hours with peptide concentrations of either 0.5, 1, 2.5, or 5 µM. M6-GrBP5 solutions were wicked from the incubated HOPG surfaces with a laboratory tissue. Residual solution was blown from the graphite surface and dried using a stream of nitrogen.

To produce graphite samples with varying degrees of lateral confinement, graphite flakes were exfoliated between two pieces of scotch tape until a satisfactory density of graphite surfaces are present. The scotch tape decorated with the graphite flakes was then pressed onto a silicon wafer with a 300 nm silicon oxide layer to transfer graphite samples on to the silicon wafer surface. The silicon wafers used had an approximate are of 0.25 cm2. Exfoliated graphite samples were then immediately incubated with 40 µL of M6-GrBP5 solution with concentrations ranging from 0.1 to 1 µM for 2 hours. After

incubation, the peptide solution was wicked from the silicon wafer which was subsequently dried under a gentle stream of nitrogen for at least 30 seconds.

7.2.2 SFM Imaging and Analysis

Scanning force microscopy imaging and analysis were conducted as detailed in Section 2.2.1. Briefly, the self-assembly structure of the dried samples was visualized under ambient conditions using a DI Nanoscope IIIa SPM (Digital Instruments) in tapping mode using soft tapping mode SFM probes (HQ:NSC14, MikroMasch). SFM images were analyzed using the Gwyddion SPM data analysis software.[47] At least three images of 1×1 μm in size were taken per sample for analysis. SFM images were first masked to distinguish the peptide nanostructure from the graphite substrate and determine the sample surface coverage. For samples with long-range ordered structuring, the image masks separating the peptide from the graphite surface were edited to exclude amorphous structures. The percent of ordering was taken as the surface coverage of ordered peptide divided by the total peptide surface coverage.

7.2.3 Optical Microscopy and Grain Size Analysis

Graphite flakes were imaged using an optical microscope using 40 times magnification. Optical images were then processed using Gwyddion to extract the area of the graphite flake and the perimeter of the graphite flake. The scale of the optical images was calibrated using an in-house fabricated “ruler” made by photolithographic etching of a graphene surface on a silicon wafer. If graphite flakes contained multiple edge bounded surfaces, the area was determined for only the bounded graphite surface where the SFM images were taken. SFM images were then matched to the area and perimeter data taken from the optical images.

7.3 Results and Discussion

7.3.1 Substrate Specific Peptide Self-Assembly Properties

To investigate the self-assembly properties of M6-GrBP5 on HOPG, 40 µL of peptide solution with aqueous concentrations of 0.5 µM to 5 µM were incubated on cleaved HOPG surfaces for 2 hours. As shown in Figure 7.1, concentrations above 2.5 µM are required to form high-surface overage assembled films. Of the tested concentrations, only the 5 µM samples contained long-range ordered structuring, with approximately 50 % of the peptide being part of the long-range ordered structure. At all concentrations tested, the adsorption process of M6-GrBP5 onto HOPG surfaces is accurately described by a Langmuir adsorption isotherm, as evidenced by the dashed fit line in Figure 7.1b. The equilibrium adsorption constant, K_{eq}, associated M6-GrBP5 adsorption is 0.44 ± 0.18 μM^{-1}. The slight deviations from Langmuir-like behavior likely result from the presence of peptide-peptide interactions at the surface that lead to long-range ordered structuring. The results presented in Figure 7.1 stand in contrast to prior results of M6-GrBP5 self-assembly on exfoliated graphite flakes performed by Hayamizu *et al*., in which high surface coverage and long-range ordering was observed at much lower peptide concentrations.

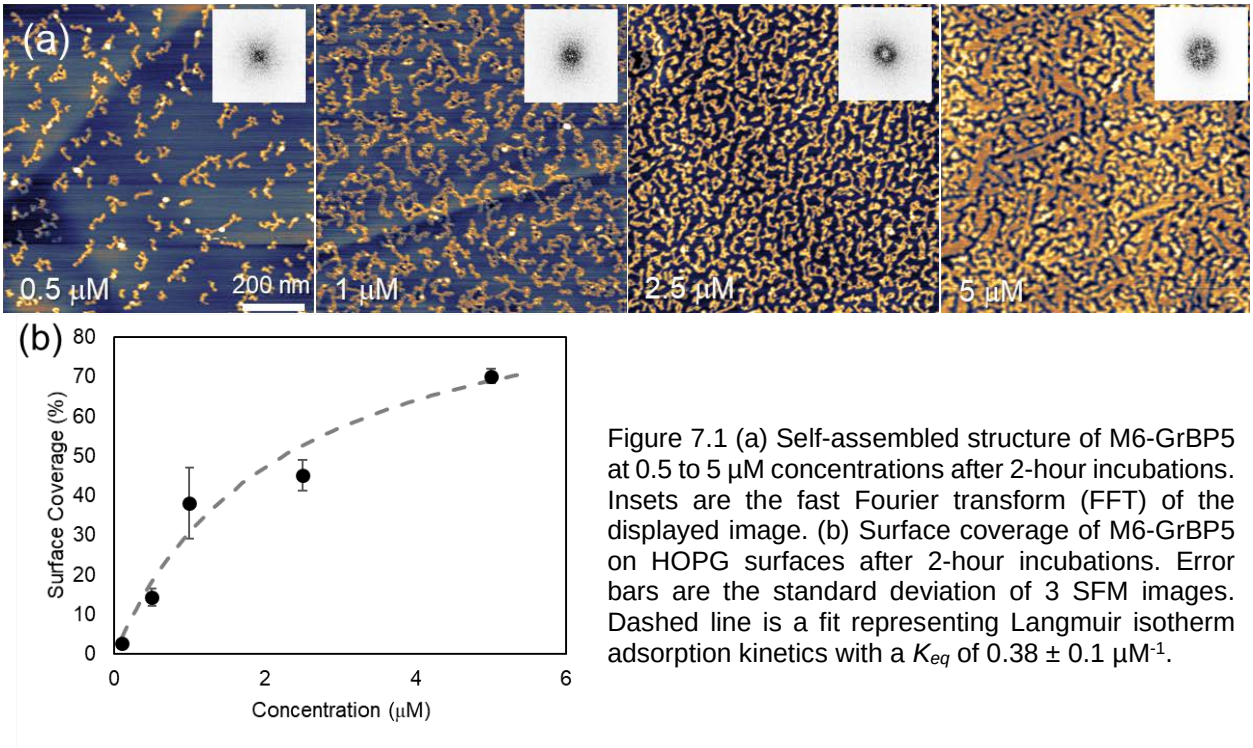

Figure 7.1 (a) Self-assembled structure of M6-GrBP5 at 0.5 to 5 µM concentrations after 2-hour incubations. Insets are the fast Fourier transform (FFT) of the displayed image. (b) Surface coverage of M6-GrBP5 on HOPG surfaces after 2-hour incubations. Error bars are the standard deviation of 3 SFM images. Dashed line is a fit representing Langmuir isotherm adsorption kinetics with a K_{eq} of 0.38 ± 0.1 μM^{-1}.

To investigate this discrepancy, exfoliated graphite flakes were incubated with 40 µL of peptide solution with 0.5 µM or 1 µM concentrations for 2 hours. As revealed by SFM images presented in Figure 7.2, the adsorption and self-assembly process of M6-GrBP5 at exfoliated graphite surfaces appears augmented over that of HOPG surfaces. For the same concentrations of aqueous peptide, the surface coverage of exfoliated graphite assemblies (Figure 7.2) is higher than that observed for HOPG samples (Figure 7.1). More critically, long-range ordering is observed for 1 µM incubations on exfoliated graphite in contrast to the limited long-range ordering of 5 µM incubations on HOPG (Figure 7.1). The augmented self-assembly of M6-GrBP5 on exfoliated samples substantiates previous results by Hayamizu *et al.*[25] and shows that the adsorption and self-assembly process is strongly dependent on the substrate preparation method.

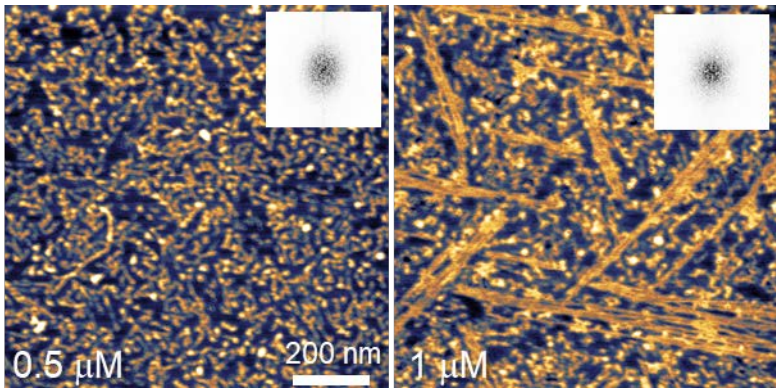

Figure 7.2 SFM images of M6-GrBP5 self-assembly structures on exfoliated graphite surfaces resulting from 0.5 µM and 1 µM peptide incubated for 2 hours.

There are a number of ways in which graphite flakes and HOPG can be different. For instance, graphite flakes may contain more defects, e.g., stack faults, than HOPG. However, an obvious, and more accessibly quantifiable, difference between the cleaved HOPG samples and exfoliated graphite samples is the dispersity of graphite grain sizes. All HOPG samples used herein are characterized by one large, consistent surface with an approximate area of 0.25 cm^2. On the other hand, the exfoliation process yields 10s to 100s of distinct graphite surfaces per sample with a range of sizes that are all several orders of magnitude smaller than the HOPG surfaces.

7.3.2 Effects of Graphite Grain Size on Coverage and Ordering

To study the impact of graphite flake size, the equilibrium structure of M6-GrBP5 assemblies resulting from 2-hour incubations of peptide concentrations ranging from 0.1 to 1 µM was compared to the area of the graphite flake. The graphite flake area was determined using optical microscopy as described in section 7.2.3. As shown in Figure 7.3a, SFM images of 1 µM samples show increased surface coverage and long-range ordering as the size of the graphite flake decreases. Broadly, the surface coverage has an asymptotic relationship with increasing graphite flake area, Figure 7.3b. This

asymptotic relationship between the peptide surface coverage and the graphite flake size suggests that as the area of the flake increases the surface coverage will reach that of the HOPG samples, i.e., ~ 38 % for 1 µM samples. The surface coverage of self-assembled peptide samples therefore lies on a continuum that goes from nearly 100% for exceedingly small graphite areas to a lower limit dictated by the equilibrium adsorption dynamics.

Interestingly, there appear to be two concentration dependent surface coverage-flake area relationships as evidenced by the two asymptotic curves shown in Figure 7.3b. Specifically, at concentrations above 0.25 µM, the relationship between surface coverage and flake size overlap generating one asymptotic curve. At concentrations below 0.25 µM, a second asymptotic relationship is found with overall surface coverage values being lower than that of the first curve. A bifurcation is observed in the surface coverage data for concentrations of 0.25 µM, Figure 7.3b, in which some graphite flakes had M6-GrBP5 coverages that fell on the lower curve while most aligned with the upper curve. As shown in Figure 7.3c, plotting the surface coverage as a function of the perimeter/area of the graphite flake appears to linearize the asymptotic relationship in Figure 7.3b suggesting that change in surface coverage is dependent on the extent of the lateral confinement.

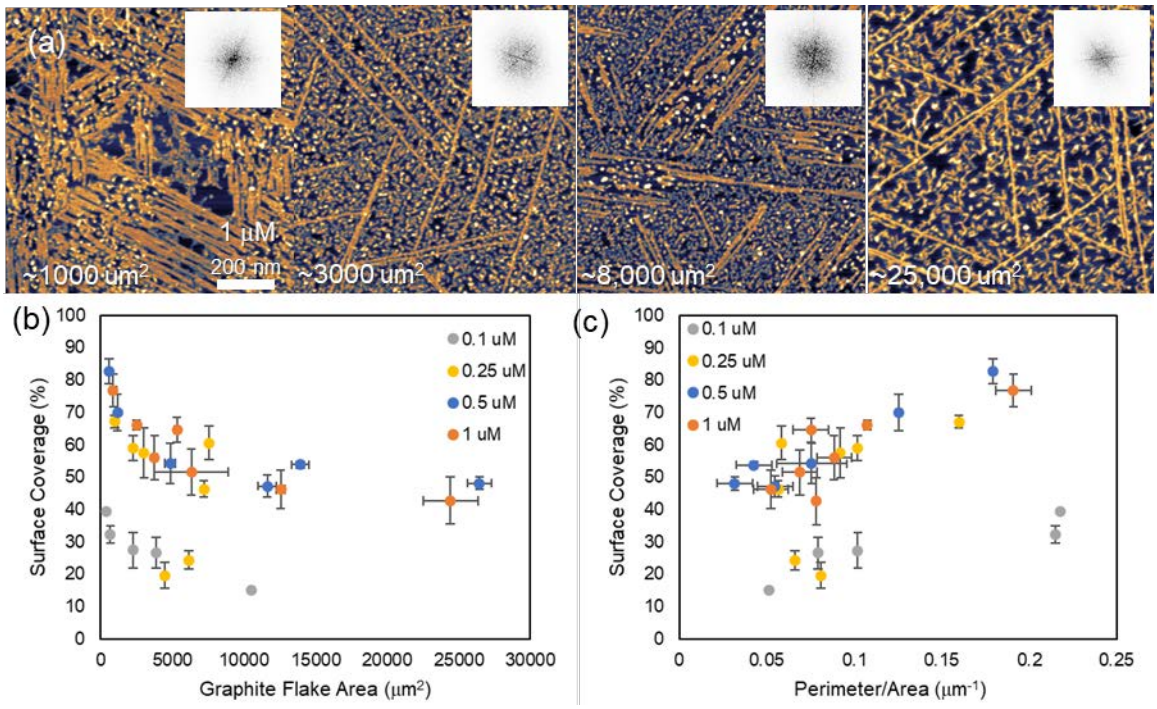

Figure 7.3 (a) Self-assembly structures of 1 µM M6-GrBP5 on exfoliated graphite surfaces substrate areas ranging from 1000 to 25000 µm^2. (b) Surface coverage of M6-GrBP5 assemblies on graphite flakes of differing areas at aqueous peptide concentrations. (c) Surface coverage of M6-GrBP5 assemblies resulting from different aqueous peptide concentrations as a function of graphite flake perimeter-to-area ratio.

The observed dependence of peptide surface coverage on the graphite flake area is surprising if we consider traditional adsorption theory as the surface coverage at equilibrium depends only on the concentration and the equilibrium adsorption constant. Moreover, the surface coverage should smoothly increase with concentration, instead of bifurcating into two surface coverage regimes. The bifurcation may result from a concentration dependent change in the packing of the peptide on the surface allowing more peptide to adsorb at the elevated concentrations. This state change may represent a change required for ordering to occur at the surface, however further experiments are needed to study these effects.

An alternative explanation for both the size and concentration dependence is that the experimental system is far from equilibrium and is kinetically trapped. If we assume

that the peptide's footprint on the graphite surface is 4 nm^2, then the ratio of total number of peptide molecules in solution relative to the total number of binding sites on the graphite surface is on the order of 10000. For HOPG samples, the ratio of total peptide molecules to available binding sites is on the order of 1 to 10. The excess peptide may kinetically drive the adsorption reaction. Favorable peptide-peptide interactions and aggregation may then impede desorption, thus, forming a non-equilibrium surface state.

In addition to a graphite flake size dependence of the surface coverage, SFM images presented in Figure 7.3a reveal an increase in the percent of ordering in the self-assembled structures, in particular for 1 μM samples. As shown in Figure 7.4a, the percent of ordering has an inverse relationship with the size of the graphite flake. While the relative prevalence of the graphite edge clearly had a relationship with the total surface coverage, the prevalence of the graphite edge does not clearly relate to the extent of the self-assembly process, as seen in Figure 7.4b. The lack of a relationship between the perimeter to area ratio suggests that the nucleation and self-assembly of M6-GrBP5 is homogenous and not edge nucleated. The linear relationship between the percent of ordering and the size of the graphite flake can be rationalized by the increase in surface coverage, i.e., increase in surface peptide concentration, which will drive the self-assembly process. Interestingly, samples prepared using 1 μM consistently contained long-range ordered structuring while samples prepared using lower concentrations did not. This result suggests that an additional parameter, beyond the amount of peptide at the surface, is required to explain the current self-assembly results. One possibility is to consider the transient system by investigating the flux of the peptide to the surface and how quickly the surface saturates.

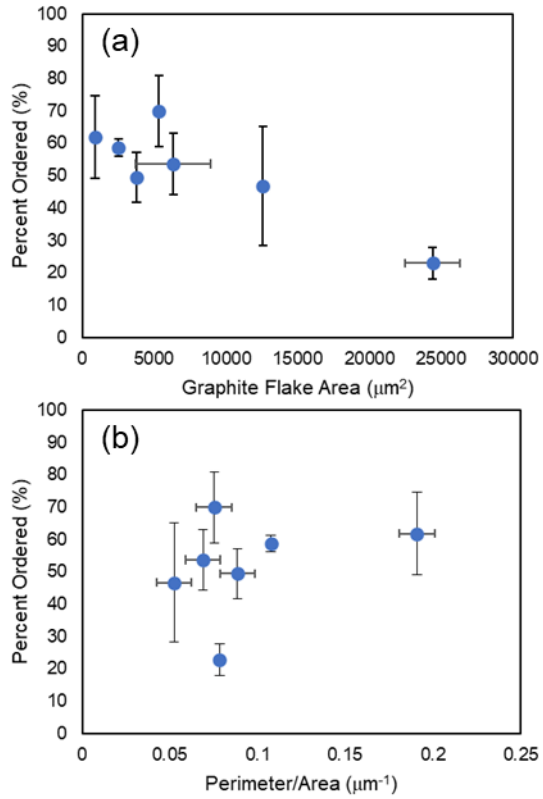

Figure 7.4 (a) Percent ordering of 1 μM M6-GrBP5 assemblies on graphite of differing flake areas. (b) Percent ordering of 1 μM M6-GrBP5 assemblies on graphite flakes with different perimeter-to-area ratios.

7.3.3 Local Graphite Grain Features Impact Peptide Self-Assembly

Given the dependence of peptide adsorption with the size and relative prevalence of the graphite edge, as well as the dependence of the extent of long-range ordering on the local peptide density, or surface coverage, it stands to reason that the self-assembly structure of peptides on graphite flakes will vary laterally. Specifically, near the edge of the graphite higher surface coverages would be expected due to the reflection (as suggested by Figure 7.3c), which in turn would yield higher percentages of ordering. To test this hypothesis, the self-assembly structure of M6-GrBP5 was investigated at various locations of a single graphite flake. As shown in Figure 7.5, the center of the graphite flake had lower surface coverage and percent order than that of either location closer to the graphite flake edge. More critically, locations on the graphite flake that were more confined (Edge 2 in Figure 7.5a), i.e., closer to the edge in several directions, showed

slightly elevated surface coverages in comparison to less confined locations (Edge 1 in Figure 7.5a). It is important to note that the locations imaged were still several microns away from the graphite edge. This result shows that the diffusion of peptides to the edge and the subsequent reflection from the edge imparts a type of memory in the local system that results in higher degrees of ordering.

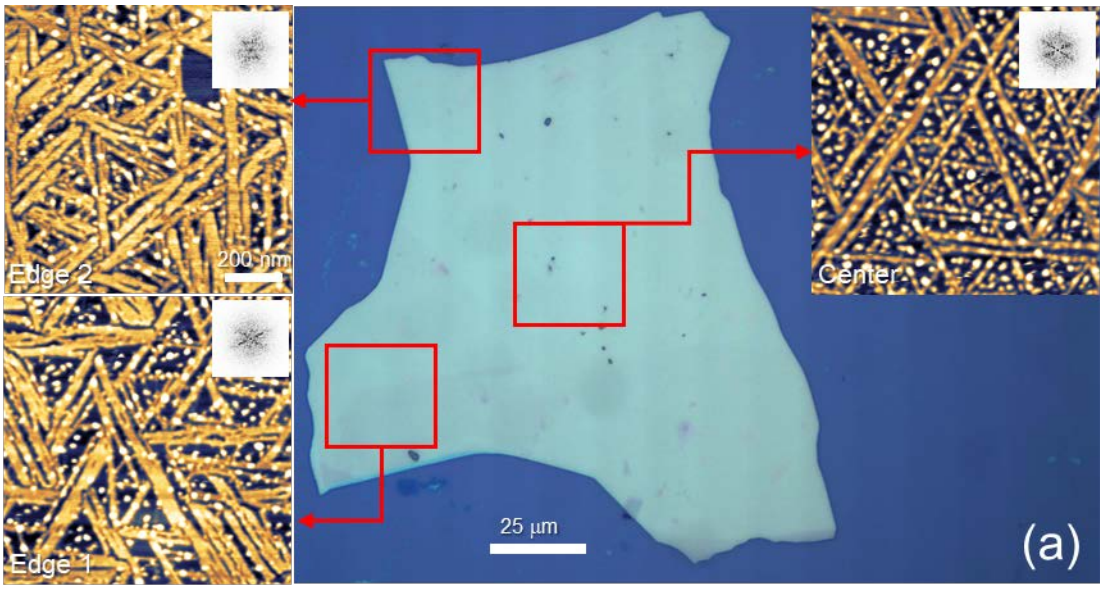

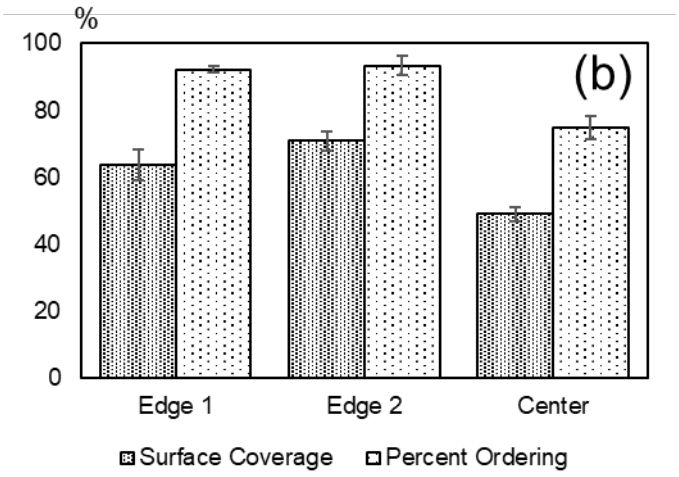

Figure 7.5 (a) Representative self-assembly structures of 0.5 µM M6-GrBP5 obtained from locations on a graphite flake with different local features. (b) Comparison of surface coverage and percent ordering obtained from differing locations on a graphite flake.

The results presented in Figure 7.5 detailing the local variations in self-assembly structures on a single graphite flake mirror the results presented for the impacts of graphite shape and size on the self-assembly. Namely, that higher surface coverages

likely result from reflection of peptides from the edge of the graphite flake and that this increase in surface coverage leads to an increase in peptide nucleation and long-range ordering of the peptide. The large error bars and variable trends presented in Figures 7.3 and 7.4 are likely a result of averaging the lateral variations in peptide self-assembly over an entire graphite flake.

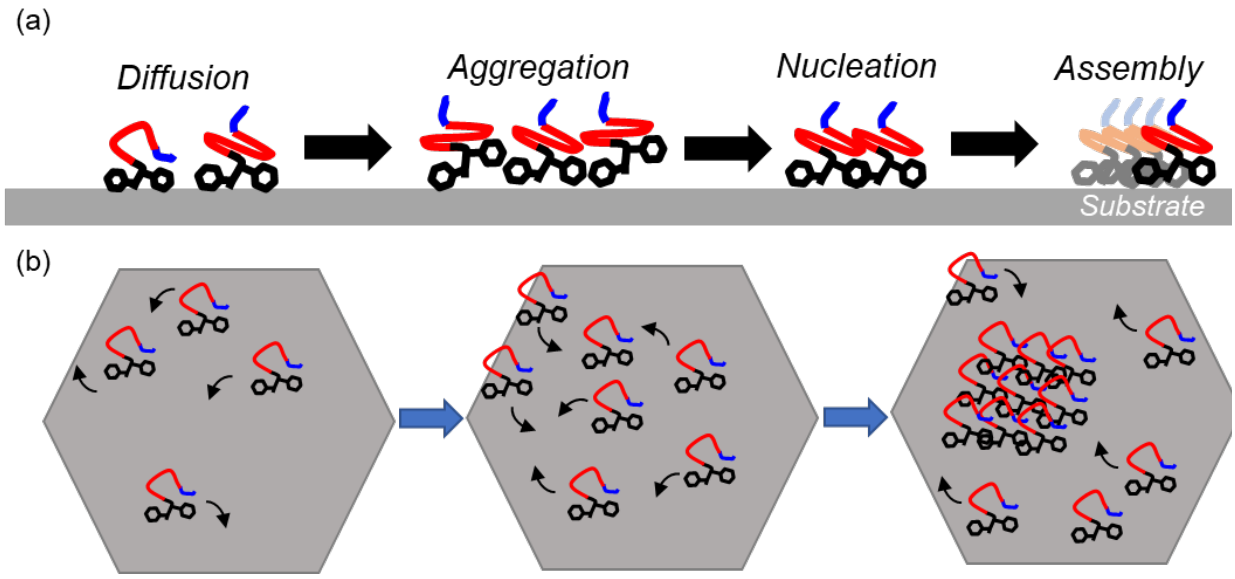

Figure 7.6 (a) Schematic of peptide assembly process on an "infinite" graphite surface. (b) Schematic of proposed impact of local edges on the self-assembly of peptides, in which reflection from the edge increases local concentrations and leads to nucleation. Arrows denote direction of diffusion.

Taken together all the results presented herein provide an overview of how the adsorption and self-assembly process change with lateral dimension of the graphite substrate. As schematized in Figure 7.6a, the self-assembly process for M6-GrBP5 on HOPG surfaces is in line with traditional homogenous nucleation in which the peptide monomers diffuse, interact, aggregate, nucleate and then grow to form long range ordered structures. When the lateral size of the graphite substrate is on the order of the diffusion length of the peptide, the edge plays an important role in the aggregation and

self-assembly process. As shown in Figure 7.6b, the peptide diffuses and can then reflect from the graphite edge thus creating an anisotropic environment that leads to artificially increased local concentrations of peptide. In turn, the increased local concentrations lead to higher surface coverage values and an increased percent of ordering.

7.4 Concluding Remarks on Lateral Confined Peptide Self-Assembly

The results presented in this chapter highlight the challenge in controlling the self-assembled structure of peptide-inorganic materials when using materials with variable size like graphite flakes. Reduction in the lateral size of the graphite surface resulted in self-assembly structures with higher surface coverage and percent of long-range ordering. The increase in adsorption was directly related to the relative presence of the graphite flake's edge suggesting the peptide reflects off the edge, thus, creating an augmented local surface coverage. This increase in surface coverage manifests itself as a size dependent increase in the apparent adsorption constant no matter the concentration of M6-GrBP5. As the size of the graphite flake increases, the surface coverage converges to a lower limit dictated by the equilibrium adsorption kinetics of M6-GrBP5 to HOPG surfaces.

The degree of long-range ordering directly increases with increasing surface coverage, i.e., increasing surface concentration. This interdependence of graphite flake size, surface coverage, and degree of ordering results in smaller graphite flakes exhibiting an increased degree of ordering. Although the reflection of peptide from the graphite edge increases the degree of ordering, the self-assembly process is still homogenous as the edge does not act as a nucleator. Moreover, due to the importance of the graphite edge

as a reflector, the surface coverage and assembly trends observed for graphite flakes of differing total sizes can also be as lateral variations within a single graphite flake.

The trends presented here are expected to continue for inorganic materials with lateral dimensions on the order of 10s to 100s of nanometers. More experimental work is needed to investigate the role of the graphite edge at these length scales as heterogenous edge nucleation may become more dominant. Additionally, the experimental study presented herein limited the interrogation to bulk graphite samples. It is known that the Hamaker constant for inorganic layered materials decreases as a function of layer, which would directly impact peptide adsorption energetics.[136] For production of practical graphene devices, it is of interest to explore how the adsorption and long-range ordering process changes with the number of graphene layers. Collectively, the presented results suggest ways in which peptide-inorganic interfaces with different lateral dimensions can be self-assembled with known structure thus enabling the further development of bioelectronic interfaces at a variety of length scales.

Chapter 8:
Summary and Outlook

Solid-binding peptides offer an extensive molecular toolbox from which novel bioelectronic devices and self-assembling hybrid systems can be developed. This toolbox is broadened further through the addition of environmental processing of the peptide conformation, or control over the substrate properties, allowing for the fine tuning of interfacial properties. The underlying molecular interactions and phenomenon that enable the self-organization of biomolecules at inorganic interfaces are extremely complex. As discussed in Chapter 2, the self-assembly process relies on the interdependent stages of aqueous peptide dynamics, peptide adsorption, peptide diffusion, peptide-peptide interactions and finally the nucleation and growth of long-range ordered structures. At each step of the self-assembly process, control over the self-assembly process can be achieved via the implementation of molecular engineering principles to control the intermolecular interactions and, thus, the structure and properties of the final self-assembled interface.

Of key importance in this work was the use of peptide sequence modifications and environmental conditions to impart control over the peptide conformation. In Chapter 3, thermal tuning of the aqueous peptide conformation was implemented to direct a peptide that normally prefers amorphous aggregation to form long-range ordered surface structures. In Chapter 4, the energetic implications of thermal tailoring of peptide conformations were revealed noting the ability to control the peptide-substrate contacts and therefore the energetics of the bio-inorganic interfaces. Such insights led to the ability to rationally design a new peptide sequence with predictive binding energetics and self-

assembly structure. Through the molecular scale tailoring of these peptide-inorganic interfaces, the electronic properties of the interface, and by extension the properties of devices built from these interfaces, can similarly be tuned. As revealed in Chapter 5, the electron tunneling across the peptide-inorganic interface can be tuned by selecting peptide conformations with differing thickness and substrate coupling.

Beyond environmental selection of the peptide conformation, sequence modifications are another molecular scale route by which the final peptide-inorganic interface can be controlled. Differing peptide sequences will have inherently different conformational propensities and thus divergent peptide-substrate and peptide-peptide interactions. The impact of such intermolecular deviations was elucidated in Chapter 6 in which peptides with high sequence similarity and self-assembly capabilities were shown to be immiscible at the molecular scale and self-assemble along different crystallographic directions of the substrate. The consequences of molecular immiscibility while maintaining long-range ordering enabled the predictable formation of extraordinarily complex binary assemblies with tunable density.

While most of the molecular scale controls on the self-assembly process rely on the peptides sequence and conformation, changes to the substrate can be similarly implemented. As studied in Chapter 7 the substrate size, or more specifically the substrate's lateral confinement of the peptide, was shown to cause higher levels of both peptide adsorption and long-range ordering. While the exact molecular rationale for the observation is yet to be determined, the role of the substrates edge as a reflector and the resultant anisotropic diffusion is clearly important for initiating the self-assembly process. Collectively, the results presented in this work outline a multitude of molecular

engineering interventions and methods by which the self-assembled structure and properties of peptide-inorganic interfaces can be controlled. Building from the molecular fundamentals and insights developed herein can enable to rational design of functional interfaces and advanced bioelectronic interfaces.

Bioconjugation or chemical functionalization of these solid-binding peptides e.g., with biotin, would enable the controlled patterning of inorganic interfaces with proteins, nanoparticles or quantum materials. Moreover, through the design of peptides with distinct substrate interactions and immiscible assemblies, the multiplexed display of enzymes for bioreactors or nanoparticles for advanced photonics/plasmonics is possible. Figure 8.1 schematizes the modularity of these solid-binding peptides and their potential use in displaying functional molecules.

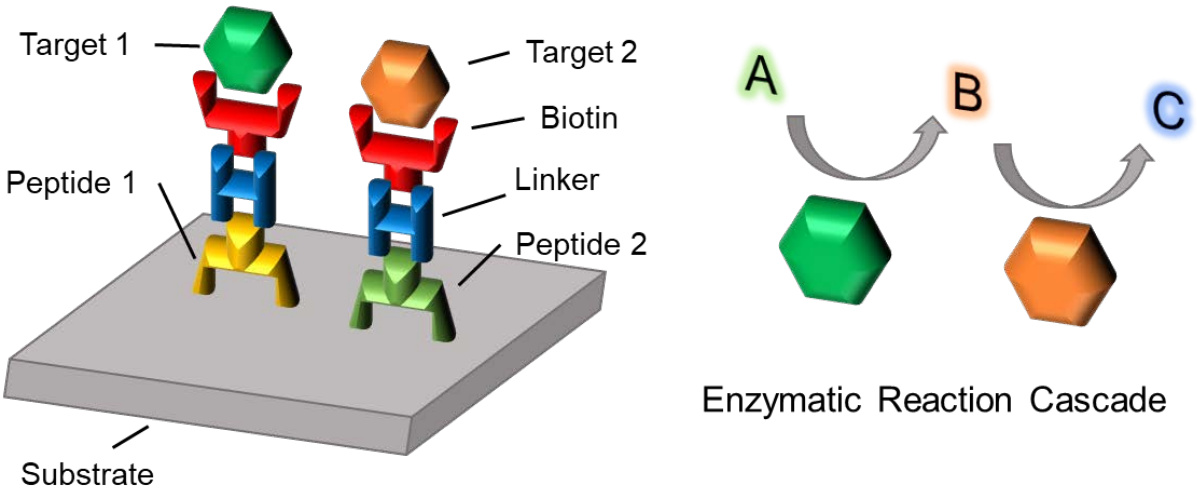

Figure 8.1 The binary assembly of two functionalized peptides can enable to capture and display of target molecules (enzymes, nanoparticles, etc.) at an inorganic substrate. For instance, the display of two enzymes that work cooperatively can be leveraged to design bioreactors with enzymatic reaction cascades that overcome diffusional limits.

Even if a functionalized peptide does not immediately self-assemble, the results presented herein demonstrate that with the proper selection of environmental conditions assembly is achievable. This possibility emphasizes the need to investigate the impact of other environmental conditions, and combination of environmental conditions, beyond temperature. For instance, the combined effect of temperature, ionicity, bias, electric fields, etc. could be leveraged to fine tune peptide conformation and self-assembly. The development of large datasets describing the combined impacts of peptide sequence and these various environmental parameters would further enable the rational design of self-assembling systems. Future work should focus on the high-throughput interrogation of peptide binding and self-assembly and leverage the abilities of machine learning and data science approaches to accurately sample and investigate the vast experimental parameter space.

With further molecular level interrogation of peptide-substrate interactions, a wealth of engineering solutions will be discovered for the design of advanced bioelectronic devices and bio-enable technologies. The work presented herein represents a step towards, and a launching point for, the goal of rationally designed biotechnologies that can address a wide variety of society's needs where the bridging of biology and solid state devices are the prime focus, such as in bio-nanosensors, bioelectronic devices, bioenergy harvesting, and future bio-enabled logic devices.

References

[1] L. P. Kozlowski, *IPC–isoelectric point calculator*, Biology direct **11**, 55 (2016).

[2] D. Shi, *Nanoscience in biomedicine* (Springer Science & Business Media, 2010).

[3] B. A. Kairdolf, X. Qian, and S. Nie, *Bioconjugated nanoparticles for biosensing, in vivo imaging, and medical diagnostics*, Analytical chemistry **89**, 1015-31 (2017).

[4] M. Liong, J. Lu, M. Kovochich, T. Xia, S. G. Ruehm, A. E. Nel, F. Tamanoi, and J. I. Zink, *Multifunctional inorganic nanoparticles for imaging, targeting, and drug delivery*, ACS nano **2**, 889-96 (2008).

[5] M. Elsabahy and K. L. Wooley, *Design of polymeric nanoparticles for biomedical delivery applications*, Chemical Society Reviews **41**, 2545-61 (2012).

[6] A. C. Ferrari, J. Meyer, V. Scardaci, C. Casiraghi, M. Lazzeri, F. Mauri, S. Piscanec, D. Jiang, K. Novoselov, and S. Roth, *Raman spectrum of graphene and graphene layers*, Physical review letters **97**, 187401 (2006).

[7] K. S. Novoselov, D. Jiang, F. Schedin, T. Booth, V. Khotkevich, S. Morozov, and A. K. Geim, *Two-dimensional atomic crystals*, Proceedings of the National Academy of Sciences **102**, 10451-3 (2005).

[8] K. J. Koski and Y. Cui, *The new skinny in two-dimensional nanomaterials*, ACS nano **7**, 3739-43 (2013).

[9] P. K. Kannan, D. J. Late, H. Morgan, and C. S. Rout, *Recent developments in 2D layered inorganic nanomaterials for sensing*, Nanoscale **7**, 13293-312 (2015).

[10] C. I. Justino, A. R. Gomes, A. C. Freitas, A. C. Duarte, and T. A. Rocha-Santos, *Graphene based sensors and biosensors*, TrAC Trends in Analytical Chemistry **91**, 53-66 (2017).

[11] Y. Shao, J. Wang, H. Wu, J. Liu, I. A. Aksay, and Y. Lin, *Graphene Based Electrochemical Sensors and Biosensors: A Review*, Electroanalysis **22**, 1027-36 (2010).

[12] P. T. Yin, S. Shah, M. Chhowalla, and K.-B. Lee, *Design, synthesis, and characterization of graphene–nanoparticle hybrid materials for bioapplications*, Chemical reviews **115**, 2483-531 (2015).

[13] Y. Wang, Z. Li, J. Wang, J. Li, and Y. Lin, *Graphene and graphene oxide: biofunctionalization and applications in biotechnology*, Trends in Biotechnology **29**, 205-12 (2011).

[14] J. Zhao, H. Park, J. Han, and J. P. Lu, *Electronic properties of carbon nanotubes with covalent sidewall functionalization*, The Journal of Physical Chemistry B **108**, 4227-30 (2004).

[15] R. J. Chen, H. C. Choi, S. Bangsaruntip, E. Yenilmez, X. Tang, Q. Wang, Y.-L. Chang, and H. Dai, *An investigation of the mechanisms of electronic sensing of protein adsorption on carbon nanotube devices*, Journal of the American Chemical Society **126**, 1563-8 (2004).

[16] A. Star, J.-C. P. Gabriel, K. Bradley, and G. Grüner, *Electronic detection of specific protein binding using nanotube FET devices*, Nano letters **3**, 459-63 (2003).

[17] A. K. Nowinski, F. Sun, A. D. White, A. J. Keefe, and S. Jiang, *Sequence, Structure, and Function of Peptide Self-Assembled Monolayers*, Journal of the American Chemical Society **134**, 6000-5 (2012).

[18] K. Z. Milowska and J. A. Majewski, *Graphene-based sensors: theoretical study*, The Journal of Physical Chemistry C **118**, 17395-401 (2014).

[19] J. A. Mann and W. R. Dichtel, *Noncovalent functionalization of graphene by molecular and polymeric adsorbates*, The Journal of Physical Chemistry Letters **4**, 2649-57 (2013).

[20] A. Care, P. L. Bergquist, and A. Sunna, *Solid-binding peptides: smart tools for nanobiotechnology*, Trends in biotechnology **33**, 259-68 (2015).

[21] M. Sarikaya, C. Tamerler, A. K. Y. Jen, K. Schulten, and F. Baneyx, *Molecular biomimetics: nanotechnology through biology*, Nat Mater **2**, 577-85 (2003).

[22] K. A. Günay and H.-A. Klok, *Identification of soft matter binding peptide ligands using phage display*, Bioconjugate chemistry **26**, 2002-15 (2015).

[23] T. Serizawa, P. Techawanitchai, and H. Matsuno, *Isolation of peptides that can recognize syndiotactic polystyrene*, ChemBioChem **8**, 989-93 (2007).

[24] S. N. Kim, Z. Kuang, J. M. Slocik, S. E. Jones, Y. Cui, B. L. Farmer, M. C. McAlpine, and R. R. Naik, *Preferential binding of peptides to graphene edges and planes*, Journal of the American Chemical Society **133**, 14480-3 (2011).

[25] Y. Hayamizu, C. R. So, S. Dag, T. S. Page, D. Starkebaum, and M. Sarikaya, *Bioelectronic interfaces by spontaneously organized peptides on 2D atomic single layer materials*, Scientific reports **6**, 33778 (2016).

[26] D. Khatayevich, M. Gungormus, H. Yazici, C. So, S. Cetinel, H. Ma, A. Jen, C. Tamerler, and M. Sarikaya, *Biofunctionalization of materials for implants using engineered peptides*, Acta Biomaterialia **6**, 4634-41 (2010).

[27] D. Khatayevich, T. Page, C. Gresswell, Y. Hayamizu, W. Grady, and M. Sarikaya, *Selective Detection of Target Proteins by Peptide-Enabled Graphene Biosensor*, Small **10**, 1505-13 (2014).

[28] L. Wang, Y. Sun, X. Xue, Y. Sun, and Z. Li, *Graphite-specific peptide mediated synthesis of Pt nanoparticles on reduced graphene oxide for electrochemical detection of H2O2*, Functional Materials Letters **9**, 1650051 (2016).

[29] M. S. Mannoor, H. Tao, J. D. Clayton, A. Sengupta, D. L. Kaplan, R. R. Naik, N. Verma, F. G. Omenetto, and M. C. McAlpine, *Graphene-based wireless bacteria detection on tooth enamel*, Nature communications **3**, 763 (2012).

[30] Y. Cui, S. N. Kim, S. E. Jones, L. L. Wissler, R. R. Naik, and M. C. McAlpine, *Chemical functionalization of graphene enabled by phage displayed peptides*, Nano letters **10**, 4559-65 (2010).

[31] C. R. So, Y. Hayamizu, H. Yazici, C. Gresswell, D. Khatayevich, C. Tamerler, and M. Sarikaya, *Controlling Self-Assembly of Engineered Peptides on Graphite by Rational Mutation*, ACS Nano **6**, 1648-56 (2012).

[32] C. R. So, J. L. Kulp III, E. E. Oren, H. Zareie, C. Tamerler, J. S. Evans, and M. Sarikaya, *Molecular recognition and supramolecular self-assembly of a genetically engineered gold binding peptide on Au {111}*, Acs Nano **3**, 1525-31 (2009).

[33] J. L. Kulp, K. Shiba, and J. S. Evans, *Probing the conformational features of a phage display polypeptide sequence directed against single-walled carbon nanohorn surfaces*, Langmuir **21**, 11907-14 (2005).

[34] Z. Su, T. Leung, and J. F. Honek, *Conformational selectivity of peptides for single-walled carbon nanotubes*, The Journal of Physical Chemistry B **110**, 23623-7 (2006).

[35] A. M. Sultan, Z. C. Westcott, Z. E. Hughes, J. P. Palafox-Hernandez, T. Giesa, V. Puddu, M. J. Buehler, C. C. Perry, and T. R. Walsh, *Aqueous peptide–TiO2*

interfaces: isoenergetic binding via either entropically or enthalpically driven mechanisms, ACS applied materials & interfaces **8**, 18620-30 (2016).

[36] R. Overney, D. Leta, C. Pictroski, M. Rafailovich, Y. Liu, J. Quinn, J. Sokolov, A. Eisenberg, and G. Overney, *Compliance measurements of confined polystyrene solutions by atomic force microscopy*, Physical review letters **76**, 1272 (1996).

[37] M. He, A. S. Blum, G. Overney, and R. M. Overney, *Effect of interfacial liquid structuring on the coherence length in nanolubrication*, Physical review letters **88**, 154302 (2002).

[38] V. G. Levich, *Physicochemical hydrodynamics* (Prentice hall, 1962).

[39] I. Langmuir, *The adsorption of gases on plane surfaces of glass, mica and platinum*, Journal of the American Chemical society **40**, 1361-403 (1918).

[40] J. Toth, *Adsorption* (CRC Press, 2002).

[41] A. Frumkin, *Über die Beeinflussung der Adsorption von Neutralmolekülen durch ein elektrisches Feld*, Zeitschrift für Physik **35**, 792-802 (1926).

[42] H. Freundlich, *Colloid & capillary chemistry* (Methuen & co. ltd, 1926).

[43] J. N. Israelachvili, *Intermolecular and surface forces* (Academic press, 2011).

[44] J. J. De Yoreo and P. G. Vekilov, *Principles of crystal nucleation and growth*, Reviews in mineralogy and geochemistry **54**, 57-93 (2003).

[45] R. P. Sear, *Nucleation: theory and applications to protein solutions and colloidal suspensions*, Journal of Physics: Condensed Matter **19**, 033101 (2007).

[46] K. S. Novoselov, A. K. Geim, S. V. Morozov, D. Jiang, Y. Zhang, S. V. Dubonos, I. V. Grigorieva, and A. A. Firsov, *Electric field effect in atomically thin carbon films*, science **306**, 666-9 (2004).

[47] D. Nečas and P. Klapetek, *Gwyddion: an open-source software for SPM data analysis*, Open Physics **10**, 181-8 (2012).

[48] S. Sills and R. M. Overney, *Creeping friction dynamics and molecular dissipation mechanisms in glassy polymers*, Phys. Rev. Lett. **91**, 095501(1-4) (2003).

[49] T. Gray, J. Killgore, J. D. Luo, A. K. Y. Jen, and R. M. Overney, *Molecular mobility and transitions in complex organic systems studied by shear force microscopy*, Nanotechnology **18** (2007).

[50] D. B. Knorr, T. O. Gray, and R. M. Overney, *Intrinsic friction analysis-Novel nanoscopic access to molecular mobility in constrained organic systems*, Ultramicroscopy **109**, 991-1000 (2009).

[51] R. M. Overney, L. Guo, H. Totsuka, M. Rafailovich, J. Sokolov, and S. A. Schwarz, *Interfacially confined polymeric systems studied by atomic force microscopy*, Mat. Res. Soc. Symp. Proc. **464**, 133-44 (1997).

[52] I. M. Ward, *Mechanical Properties of Solid Polymers* (Wiley-Interscience, London, 1971).

[53] J. D. Ferry, *Viscoelastic Properties of Polymers* (John Wiley & Sons, New York, 1980).

[54] D. B. Knorr, T. O. Gray, and R. M. Overney, *Intrinsic friction analysis—Novel nanoscopic access to molecular mobility in constrained organic systems*, Ultramicroscopy **109**, 991-1000 (2009).

[55] C. Buenviaje, S.-R. Ge, M. Rafailovich, and R. Overney, *Atomic force microscopy calibration methods for lateral force, elasticity, and viscosity*, MRS Online Proceedings Library Archive **522** (1998).

[56] K. J. Bowers, D. E. Chow, H. Xu, R. O. Dror, M. P. Eastwood, B. A. Gregersen, J. L. Klepeis, I. Kolossvary, M. A. Moraes, and F. D. Sacerdoti, in *SC'06: Proceedings of the 2006 ACM/IEEE Conference on Supercomputing* (IEEE, 2006), p. 43-.

[57] C. Pramanik, T. Jamil, J. R. Gissinger, D. Guittet, P. J. Arias-Monje, S. Kumar, and H. Heinz, *Polyacrylonitrile Interactions with Carbon Nanotubes in Solution: Conformations and Binding as a Function of Solvent, Temperature, and Concentration*, Advanced Functional Materials, 1905247 (2019).

[58] B. R. Brooks, C. L. Brooks III, A. D. Mackerell Jr, L. Nilsson, R. J. Petrella, B. Roux, Y. Won, G. Archontis, C. Bartels, and S. Boresch, *CHARMM: the biomolecular simulation program*, Journal of computational chemistry **30**, 1545-614 (2009).

[59] M. Levitt, M. Hirshberg, R. Sharon, and V. Daggett, *Potential energy function and parameters for simulations of the molecular dynamics of proteins and nucleic acids in solution*, Computer physics communications **91**, 215-31 (1995).

[60] D. Beck, D. Alonso, and V. Daggett, *In lucem molecular mechanics (ilmm)*, Computer Program, University of Washington, Seattle (2000).

[61] M. Levitt, M. Hirshberg, R. Sharon, K. E. Laidig, and V. Daggett, *Calibration and testing of a water model for simulation of the molecular dynamics of proteins and nucleic acids in solution*, The Journal of Physical Chemistry B **101**, 5051-61 (1997).

[62] R. C. Bernardi, M. C. Melo, and K. Schulten, *Enhanced sampling techniques in molecular dynamics simulations of biological systems*, Biochimica et Biophysica Acta (BBA)-General Subjects **1850**, 872-7 (2015).

[63] P. Liu, B. Kim, R. A. Friesner, and B. Berne, *Replica exchange with solute tempering: A method for sampling biological systems in explicit water*, Proceedings of the National Academy of Sciences **102**, 13749-54 (2005).

[64] C. M. Mao, J. Sampath, K. G. Sprenger, G. Drobny, and J. Pfaendtner, *Molecular Driving Forces in Peptide Adsorption to Metal Oxide Surfaces*, Langmuir **35**, 5911-20 (2019).

[65] A. Barducci, M. Bonomi, and M. Parrinello, *Metadynamics*, Wiley Interdisciplinary Reviews: Computational Molecular Science **1**, 826-43 (2011).

[66] A. Barducci, G. Bussi, and M. Parrinello, *Well-tempered metadynamics: a smoothly converging and tunable free-energy method*, Physical review letters **100**, 020603 (2008).

[67] G. M. Whitesides and B. Grzybowski, *Self-assembly at all scales*, Science **295**, 2418-21 (2002).

[68] D. Philp and J. F. Stoddart, *Self-assembly in natural and unnatural systems*, Angewandte Chemie International Edition in English **35**, 1154-96 (1996).

[69] M. Zerial and H. McBride, *Rab proteins as membrane organizers*, Nature reviews Molecular cell biology **2**, 107 (2001).

[70] A. Mallavarapu and T. Mitchison, *Regulated actin cytoskeleton assembly at filopodium tips controls their extension and retraction*, The Journal of cell biology **146**, 1097-106 (1999).

[71] S. Zhang, *Fabrication of novel biomaterials through molecular self-assembly*, Nature biotechnology **21**, 1171 (2003).

[72] Y. Lin, A. Böker, J. He, K. Sill, H. Xiang, C. Abetz, X. Li, J. Wang, T. Emrick, and S. Long, *Self-directed self-assembly of nanoparticle/copolymer mixtures*, Nature **434**, 55 (2005).

[73] J. C. Love, L. A. Estroff, J. K. Kriebel, R. G. Nuzzo, and G. M. Whitesides, *Self-Assembled Monolayers of Thiolates on Metals as a Form of Nanotechnology*, Chemical Reviews **105**, 1103-70 (2005).

[74] T. Kato, *Self-assembly of phase-segregated liquid crystal structures*, Science **295**, 2414-8 (2002).

[75] L. Zang, Y. Che, and J. S. Moore, *One-dimensional self-assembly of planar π-conjugated molecules: adaptable building blocks for organic nanodevices*, Accounts of chemical research **41**, 1596-608 (2008).

[76] D. E. Koshland Jr, *The key–lock theory and the induced fit theory*, Angewandte Chemie International Edition in English **33**, 2375-8 (1995).

[77] R. Mannhold, H. Kubinyi, and G. Folkers, *Protein-ligand interactions: from molecular recognition to drug design* (John Wiley & Sons, 2006).

[78] P. W. Rothemund, *Folding DNA to create nanoscale shapes and patterns*, Nature **440**, 297 (2006).

[79] S. Gonen, F. DiMaio, T. Gonen, and D. Baker, *Design of ordered two-dimensional arrays mediated by noncovalent protein-protein interfaces*, Science **348**, 1365-8 (2015).

[80] A. Aggeli, I. A. Nyrkova, M. Bell, R. Harding, L. Carrick, T. C. McLeish, A. N. Semenov, and N. Boden, *Hierarchical self-assembly of chiral rod-like molecules*

as a model for peptide β-sheet tapes, ribbons, fibrils, and fibers, Proceedings of the National Academy of Sciences **98**, 11857-62 (2001).

[81] J. D. Hartgerink, E. Beniash, and S. I. Stupp, *Self-assembly and mineralization of peptide-amphiphile nanofibers*, Science **294**, 1684-8 (2001).

[82] S. Woo and P. W. Rothemund, *Self-assembly of two-dimensional DNA origami lattices using cation-controlled surface diffusion*, Nature communications **5**, 4889 (2014).

[83] C. Whitehouse, J. Fang, A. Aggeli, M. Bell, R. Brydson, C. W. Fishwick, J. R. Henderson, C. M. Knobler, R. W. Owens, and N. H. Thomson, *Adsorption and self-assembly of peptides on mica substrates*, Angewandte Chemie International Edition **44**, 1965-8 (2005).

[84] E. Györvary, O. Stein, D. Pum, and U. Sleytr, *Self-assembly and recrystallization of bacterial S-layer proteins at silicon supports imaged in real time by atomic force microscopy*, Journal of microscopy **212**, 300-6 (2003).

[85] J. Israelachvili, *Self-assembly in two dimensions: surface micelles and domain formation in monolayers*, Langmuir **10**, 3774-81 (1994).

[86] R. Schulman and E. Winfree, *Synthesis of crystals with a programmable kinetic barrier to nucleation*, Proceedings of the National Academy of Sciences **104**, 15236-41 (2007).

[87] M. Altman, P. Lee, A. Rich, and S. Zhang, *Conformational behavior of ionic self-complementary peptides*, Protein Science **9**, 1095-105 (2000).

[88] J. H. Collier, B. H. Hu, J. W. Ruberti, J. Zhang, P. Shum, D. H. Thompson, and P. B. Messersmith, *Thermally and photochemically triggered self-assembly of peptide hydrogels*, Journal of the American Chemical Society **123**, 9463-4 (2001).

[89] A. K. Dunker, J. D. Lawson, C. J. Brown, R. M. Williams, P. Romero, J. S. Oh, C. J. Oldfield, A. M. Campen, C. M. Ratliff, and K. W. Hipps, *Intrinsically disordered protein*, Journal of molecular graphics and modelling **19**, 26-59 (2001).

[90] Z. A. Levine, L. Larini, N. E. LaPointe, S. C. Feinstein, and J.-E. Shea, *Regulation and aggregation of intrinsically disordered peptides*, Proceedings of the National Academy of Sciences **112**, 2758-63 (2015).

[91] H. J. Dyson and P. E. Wright, *Intrinsically unstructured proteins and their functions*, Nature reviews Molecular cell biology **6**, 197 (2005).

[92] Q. Qiao, G. R. Bowman, and X. Huang, *Dynamics of an intrinsically disordered protein reveal metastable conformations that potentially seed aggregation*, Journal of the American Chemical Society **135**, 16092-101 (2013).

[93] M. J. Penna, M. Mijajlovic, C. Tamerler, and M. J. Biggs, *Molecular-level understanding of the adsorption mechanism of a graphite-binding peptide at the water/graphite interface*, Soft Matter **11**, 5192-203 (2015).

[94] Z. E. Hughes and T. R. Walsh, *What makes a good graphene-binding peptide? Adsorption of amino acids and peptides at aqueous graphene interfaces*, Journal of Materials Chemistry B **3**, 3211-21 (2015).

[95] T. Kacar, M. T. Zin, C. So, B. Wilson, H. Ma, N. Gul-Karaguler, A. K. Y. Jen, M. Sarikaya, and C. Tamerler, *Directed self-immobilization of alkaline phosphatase*

on micro-patterned substrates via genetically fused metal-binding peptide, Biotechnology and Bioengineering **103**, 696-705 (2009).

96 M. Hnilova, D. Khatayevich, A. Carlson, E. E. Oren, C. Gresswell, S. Zheng, F. Ohuchi, M. Sarikaya, and C. Tamerler, *Single-step fabrication of patterned gold film array by an engineered multi-functional peptide*, Journal of colloid and interface science **365**, 97-102 (2012).

97 M. Hnilova, E. E. Oren, U. O. Seker, B. R. Wilson, S. Collino, J. S. Evans, C. Tamerler, and M. Sarikaya, *Effect of molecular conformations on the adsorption behavior of gold-binding peptides*, Langmuir **24**, 12440-5 (2008).

98 J. N. Mabry, M. Kastantin, and D. K. Schwartz, *Capturing Conformation-Dependent Molecule–Surface Interactions When Surface Chemistry Is Heterogeneous*, ACS nano **9**, 7237-47 (2015).

99 E. F. Pettersen, T. D. Goddard, C. C. Huang, G. S. Couch, D. M. Greenblatt, E. C. Meng, and T. E. Ferrin, *UCSF Chimera—a visualization system for exploratory research and analysis*, Journal of computational chemistry **25**, 1605-12 (2004).

100 T. A. Martinek, A. Hetényi, L. Fülöp, I. M. Mándity, G. K. Tóth, I. Dékány, and F. Fülöp, *Secondary Structure Dependent Self-Assembly of β-Peptides into Nanosized Fibrils and Membranes*, Angewandte Chemie International Edition **45**, 2396-400 (2006).

101 S. De Feyter, A. Miura, S. Yao, Z. Chen, F. Würthner, P. Jonkheijm, A. P. Schenning, E. Meijer, and F. C. De Schryver, *Two-dimensional self-assembly into multicomponent hydrogen-bonded nanostructures*, Nano letters **5**, 77-81 (2005).

[102] M. R. Dreher, A. J. Simnick, K. Fischer, R. J. Smith, A. Patel, M. Schmidt, and A. Chilkoti, *Temperature triggered self-assembly of polypeptides into multivalent spherical micelles*, Journal of the American Chemical Society **130**, 687-94 (2008).

[103] A. K. Boal, F. Ilhan, J. E. DeRouchey, T. Thurn-Albrecht, T. P. Russell, and V. M. Rotello, *Self-assembly of nanoparticles into structured spherical and network aggregates*, Nature **404**, 746 (2000).

[104] A. Aggeli, M. Bell, L. M. Carrick, C. W. Fishwick, R. Harding, P. J. Mawer, S. E. Radford, A. E. Strong, and N. Boden, *pH as a trigger of peptide β-sheet self-assembly and reversible switching between nematic and isotropic phases*, Journal of the American Chemical Society **125**, 9619-28 (2003).

[105] L. Scullion, T. Doneux, L. Bouffier, D. G. Fernig, S. J. Higgins, D. Bethell, and R. J. Nichols, *Large conductance changes in peptide single molecule junctions controlled by pH*, The Journal of Physical Chemistry C **115**, 8361-8 (2011).

[106] K. Kitagawa, T. Morita, and S. Kimura, *A helical molecule that exhibits two lengths in response to an applied potential*, Angewandte Chemie International Edition **44**, 6330-3 (2005).

[107] Y. Chen, E. R. Cruz-Chu, J. C. Woodard, M. R. Gartia, K. Schulten, and L. Liu, *Electrically induced conformational change of peptides on metallic nanosurfaces*, ACS nano **6**, 8847-56 (2012).

[108] J. Chen, E. Zhu, J. Liu, S. Zhang, Z. Lin, X. Duan, H. Heinz, Y. Huang, and J. J. De Yoreo, *Building two-dimensional materials one row at a time: Avoiding the nucleation barrier*, Science **362**, 1135-9 (2018).

[109] T. D. Jorgenson, M. Milligan, M. Sarikaya, and R. Overney, *Conformationally Directed Assembly of Peptides on 2D Solid Surfaces Mediated by Thermal Stimuli*, Soft Matter (2019).

[110] D. Khatayevich, C. R. So, Y. Hayamizu, C. Gresswell, and M. Sarikaya, *Controlling the Surface Chemistry of Graphite by Engineered Self-Assembled Peptides*, Langmuir **28**, 8589-93 (2012).

[111] E. A. Della Pia, M. Elliott, D. D. Jones, and J. E. Macdonald, *Orientation-dependent electron transport in a single redox protein*, ACS nano **6**, 355-61 (2011).

[112] L. S. Kocherlakota, D. B. Knorr Jr, L. Foster, and R. M. Overney, *Enhanced gas transport properties and molecular mobilities in nano-constrained poly [1-(trimethylsilyl)-1-propyne] membranes*, Polymer **53**, 2394-401 (2012).

[113] H. Han, Y. Zhang, N. Wang, M. K. Samani, Y. Ni, Z. Y. Mijbil, M. Edwards, S. Xiong, K. Sääskilahti, and M. Murugesan, *Functionalization mediates heat transport in graphene nanoflakes*, Nature Communications **7**, 11281 (2016).

[114] D. Xiao, W. Sun, H. Dai, Y. Zhang, X. Qin, L. Li, Z. Wei, and X. Chen, *Influence of charge states on the π–π interactions of aromatic side chains with surface of graphene sheet and single-walled carbon nanotubes in bioelectrodes*, The Journal of Physical Chemistry C **118**, 20694-701 (2014).

[115] C. Rajesh, C. Majumder, H. Mizuseki, and Y. Kawazoe, *A theoretical study on the interaction of aromatic amino acids with graphene and single walled carbon nanotube*, The Journal of chemical physics **130**, 124911 (2009).

[116] S. Dasetty, J. K. Barrows, and S. Sarupria, *Adsorption of amino acids on graphene: assessment of current force fields*, Soft Matter **15**, 2359-72 (2019).

[117] T. Kuila, S. Bose, P. Khanra, A. K. Mishra, N. H. Kim, and J. H. Lee, *Recent advances in graphene-based biosensors*, Biosensors and Bioelectronics **26**, 4637-48 (2011).

[118] A. Zhang and C. M. Lieber, *Nano-bioelectronics*, Chemical reviews **116**, 215-57 (2016).

[119] E. Katz and I. Willner, *Biomolecule-functionalized carbon nanotubes: applications in nanobioelectronics*, ChemPhysChem **5**, 1084-104 (2004).

[120] L. Groenendaal, F. Jonas, D. Freitag, H. Pielartzik, and J. R. Reynolds, *Poly (3, 4-ethylenedioxythiophene) and its derivatives: past, present, and future*, Advanced materials **12**, 481-94 (2000).

[121] D. Samanta and A. Sarkar, *Immobilization of bio-macromolecules on self-assembled monolayers: methods and sensor applications*, Chemical Society Reviews **40**, 2567-92 (2011).

[122] V. Georgakilas, J. N. Tiwari, K. C. Kemp, J. A. Perman, A. B. Bourlinos, K. S. Kim, and R. Zboril, *Noncovalent functionalization of graphene and graphene oxide for energy materials, biosensing, catalytic, and biomedical applications*, Chemical reviews **116**, 5464-519 (2016).

[123] H. Pyles, S. Zhang, J. J. De Yoreo, and D. Baker, *Controlling protein assembly on inorganic crystals through designed protein interfaces*, Nature **571**, 251-6 (2019).

[124] T. D. Jorgenson, M. Milligan, M. Sarikaya, and R. M. Overney, *Conformationally directed assembly of peptides on 2D surfaces mediated by thermal stimuli*, Soft matter **15**, 7360-8 (2019).

[125] T. D. Jorgenson, D. T. Yucesoy, M. Sarikaya, and R. M. Overney, *Thermal Selection of Aqueous Molecular Conformations for Tailored Energetics of Peptide Assemblies at Solid Interfaces*, Langmuir (2019).

[126] T. Seki, C. R. So, T. R. Page, D. Starkebaum, Y. Hayamizu, and M. Sarikaya, *Electrochemical control of peptide self-organization on atomically flat solid surfaces: a case study with graphite*, Langmuir **34**, 1819-26 (2017).

[127] P. Li, K. Sakuma, S. Tsuchiya, L. Sun, and Y. Hayamizu, *Fibroin-like peptides self-assembling on two-dimensional materials as a molecular scaffold for potential biosensing*, ACS applied materials & interfaces **11**, 20670-7 (2019).

[128] B. Akdim, R. Pachter, S. S. Kim, R. R. Naik, T. R. Walsh, S. Trohalaki, G. Hong, Z. Kuang, and B. L. Farmer, *Electronic properties of a graphene device with peptide adsorption: insight from simulation*, ACS applied materials & interfaces **5**, 7470-7 (2013).

[129] S. Sek, K. Swiatek, and A. Misicka, *Electrical behavior of molecular junctions incorporating α-helical peptide*, The Journal of Physical Chemistry B **109**, 23121-4 (2005).

[130] H. Uji, T. Morita, and S. Kimura, *Molecular direction dependence of single-molecule conductance of a helical peptide in molecular junction*, Physical Chemistry Chemical Physics **15**, 757-60 (2013).

[131] D. R. Samarajeewa, G. R. Dieckmann, S. O. Nielsen, and I. H. Musselman, *Modifying the electronic properties of single-walled carbon nanotubes using designed surfactant peptides*, Nanoscale **4**, 4544-54 (2012).

[132] C. Guo, X. Yu, S. Refaely-Abramson, L. Sepunaru, T. Bendikov, I. Pecht, L. Kronik, A. Vilan, M. Sheves, and D. Cahen, *Tuning electronic transport via hepta-alanine peptides junction by tryptophan doping*, Proceedings of the National Academy of Sciences **113**, 10785-90 (2016).

[133] M. Bonomi, D. Branduardi, G. Bussi, C. Camilloni, D. Provasi, P. Raiteri, D. Donadio, F. Marinelli, F. Pietrucci, and R. A. Broglia, *PLUMED: A portable plugin for free-energy calculations with molecular dynamics*, Computer Physics Communications **180**, 1961-72 (2009).

[134] M. J. Abraham, T. Murtola, R. Schulz, S. Páll, J. C. Smith, B. Hess, and E. Lindahl, *GROMACS: High performance molecular simulations through multi-level parallelism from laptops to supercomputers*, SoftwareX **1**, 19-25 (2015).

[135] C. Pramanik, J. R. Gissinger, S. Kumar, and H. Heinz, *Carbon nanotube dispersion in solvents and polymer solutions: mechanisms, assembly, and preferences*, ACS nano **11**, 12805-16 (2017).

[136] L. S. Kocherlakota, B. A. Krajina, and R. M. Overney, *Communication: Local energetic analysis of the interfacial and surface energies of graphene from the single layer to graphite*, The Journal of Chemical Physics **143**, 241105 (2015).

[137] B. S. Winkel, *Metabolic channeling in plants*, Annu. Rev. Plant Biol. **55**, 85-107 (2004).

[138] K.-H. Suss, C. Arkona, R. Manteuffel, and K. Adler, *Calvin cycle multienzyme complexes are bound to chloroplast thylakoid membranes of higher plants in situ*, Proceedings of the National Academy of Sciences **90**, 5514-8 (1993).

[139] M. Castellana, M. Z. Wilson, Y. Xu, P. Joshi, I. M. Cristea, J. D. Rabinowitz, Z. Gitai, and N. S. Wingreen, *Enzyme clustering accelerates processing of intermediates through metabolic channeling*, Nature biotechnology **32**, 1011-8 (2014).

[140] I. Wheeldon, S. D. Minteer, S. Banta, S. C. Barton, P. Atanassov, and M. Sigman, *Substrate channelling as an approach to cascade reactions*, Nature chemistry **8**, 299 (2016).

[141] J. H. Bang and P. V. Kamat, *Quantum dot sensitized solar cells. A tale of two semiconductor nanocrystals: CdSe and CdTe*, ACS nano **3**, 1467-76 (2009).

[142] J.-H. Song, T. Atay, S. Shi, H. Urabe, and A. V. Nurmikko, *Large enhancement of fluorescence efficiency from CdSe/ZnS quantum dots induced by resonant coupling to spatially controlled surface plasmons*, Nano letters **5**, 1557-61 (2005).

[143] M. Wang, S. Kumar, A. Lee, N. Felorzabihi, L. Shen, F. Zhao, P. Froimowicz, G. D. Scholes, and M. A. Winnik, *Nanoscale co-organization of quantum dots and conjugated polymers using polymeric micelles as templates*, Journal of the American Chemical Society **130**, 9481-91 (2008).

[144] R. J. Conrado, J. D. Varner, and M. P. DeLisa, *Engineering the spatial organization of metabolic enzymes: mimicking nature's synergy*, Current opinion in biotechnology **19**, 492-9 (2008).

[145] F. Jia, B. Narasimhan, and S. Mallapragada, *Materials-based strategies for multi-enzyme immobilization and co-localization: a review*, Biotechnology and bioengineering **111**, 209-22 (2014).

[146] J. E. Dueber, G. C. Wu, G. R. Malmirchegini, T. S. Moon, C. J. Petzold, A. V. Ullal, K. L. Prather, and J. D. Keasling, *Synthetic protein scaffolds provide modular control over metabolic flux*, Nature biotechnology **27**, 753 (2009).

[147] P. Q. Nguyen, N. M. D. Courchesne, A. Duraj-Thatte, P. Praveschotinunt, and N. S. Joshi, *Engineered living materials: prospects and challenges for using biological systems to direct the assembly of smart materials*, Advanced Materials **30**, 1704847 (2018).

[148] A. Y. Chen, C. Zhong, and T. K. Lu, (ACS Publications, 2015).

[149] T. A. Pham, B. C. Choi, and Y. T. Jeong, *Facile covalent immobilization of cadmium sulfide quantum dots on graphene oxide nanosheets: preparation, characterization, and optical properties*, Nanotechnology **21**, 465603 (2010).

[150] U. T. Bornscheuer, *Immobilizing enzymes: how to create more suitable biocatalysts*, Angewandte Chemie International Edition **42**, 3336-7 (2003).

[151] N. Hildebrandt, *Biofunctional quantum dots: controlled conjugation for multiplexed biosensors*, Acs Nano **5**, 5286-90 (2011).

[152] J. N. Talbert and J. M. Goddard, *Enzymes on material surfaces*, Colloids and Surfaces B: Biointerfaces **93**, 8-19 (2012).

[153] R. Ganesan, K. Kratz, and A. Lendlein, *Multicomponent protein patterning of material surfaces*, Journal of Materials Chemistry **20**, 7322-31 (2010).

[154] N. Stephanopoulos, J. H. Ortony, and S. I. Stupp, *Self-assembly for the synthesis of functional biomaterials*, Acta materialia **61**, 912-30 (2013).

[155] N. C. Seeman and H. F. Sleiman, *DNA nanotechnology*, Nature Reviews Materials **3**, 1-23 (2017).

[156] J. Fu, Y. R. Yang, A. Johnson-Buck, M. Liu, Y. Liu, N. G. Walter, N. W. Woodbury, and H. Yan, *Multi-enzyme complexes on DNA scaffolds capable of substrate channelling with an artificial swinging arm*, Nature nanotechnology **9**, 531 (2014).

[157] X. Ma, S. Zhang, F. Jiao, C. J. Newcomb, Y. Zhang, A. Prakash, Z. Liao, M. D. Baer, C. J. Mundy, and J. Pfaendtner, *Tuning crystallization pathways through sequence engineering of biomimetic polymers*, Nature materials **16**, 767-74 (2017).

[158] H. Rapaport, K. Kjaer, T. R. Jensen, L. Leiserowitz, and D. A. Tirrell, *Two-dimensional order in β-sheet peptide monolayers*, Journal of the American Chemical Society **122**, 12523-9 (2000).

[159] T. R. Walsh and M. R. Knecht, *Biomolecular Material Recognition in Two Dimensions: Peptide Binding to Graphene, h-BN, and MoS2 Nanosheets as Unique Bioconjugates*, Bioconjugate chemistry **30**, 2727-50 (2019).

[160] L. Sun, T. Narimatsu, S. Tsuchiya, T. Tanaka, P. Li, and Y. Hayamizu, *Water stability of self-assembled peptide nanostructures for sequential formation of two-dimensional interstitial patterns on layered materials*, RSC advances **6**, 96889-97 (2016).

[161] Z. Li, Y. Zhang, Y. Su, P. Ouyang, J. Ge, and Z. Liu, *Spatial co-localization of multi-enzymes by inorganic nanocrystal–protein complexes*, Chemical Communications **50**, 12465-8 (2014).

[162] F. Zhang, H. N. Du, Z. X. Zhang, L. N. Ji, H. T. Li, L. Tang, H. B. Wang, C. H. Fan, H. J. Xu, and Y. Zhang, *Epitaxial growth of peptide nanofilaments on inorganic*

surfaces: Effects of interfacial hydrophobicity/hydrophilicity, Angewandte Chemie International Edition **45**, 3611-3 (2006).

[163] J.-j. Yu, Y. H. Tan, X. Li, P.-K. Kuo, and G.-y. Liu, *A nanoengineering approach to regulate the lateral heterogeneity of self-assembled monolayers*, Journal of the American Chemical Society **128**, 11574-81 (2006).

[164] L. Verstraete, J. Greenwood, B. E. Hirsch, and S. De Feyter, *Self-assembly under confinement: nanocorrals for understanding fundamentals of 2D crystallization*, ACS nano **10**, 10706-15 (2016).